THE UNIVERSITY OF CALGARY

Wavelength dependent photochemistry in d^6 transition metal complexes having low-lying MLCT states

by

Lawton Earl Shaw

A DISSERTATION

SUBMITTED TO THE FACULTY OF GRADUATE STUDIES

IN PARTIAL FULFILMENT OF THE REQUIREMENTS FOR THE

DEGREE OF DOCTOR OF PHILOSOPHY

DEPARTMENT OF CHEMISTRY

CALGARY, ALBERTA

JANUARY, 1999

National Library of Canada
Acquisitions and Bibliographic Services
395 Wellington Street
Ottawa ON K1A 0N4
Canada

Bibliothèque nationale du Canada
Acquisitions et services bibliographiques
395, rue Wellington
Ottawa ON K1A 0N4
Canada

Your file Votre référence

Our file Notre référence

0-612-38504-3

Canada

ABSTRACT:

Three d^6 transition metal complexes having low-lying metal-to-ligand charge transfer (MLCT) excited states are prepared and their wavelength dependent photochemistry investigated using a combination of quantum yield measurements and time resolved spectroscopy (picosecond and nanosecond time resolution). Chromium hexakis(phenylisocyanide), or $Cr(CNPh)_6$, a compound known to undergo both photosubstitution and electron transfer, is found to have two different modes of photoreactivity. The first mode applies to high excitation energies (> 27000 cm^{-1}) and involves neutral dissociation of a phenylisocyanide ligand. The second mode applies to lower excitation energies and is responsible for parallel substitution and electron transfer reactivity at those irradiation wavelengths. It is proposed that the second mode involves dissociation of a phenylisocyanide radical anion from the MLCT excited state. Overall, the photosubstitution quantum yields of $Cr(CNPh)_6$ increase with increasing excitation energy while the electron transfer quantum yields are small at high excitation energy but reach a maximum at low excitation energy (20490 cm^{-1}). Molybdenum hexakis(phenylisocyanide), or $Mo(CNPh)_6$, has been proposed to undergo photosubstitution via an associative mechanism and is known to undergo photoinduced electron transfer. It is shown that the photosubstitution is in fact dissociative in nature and is wavelength independent. The photoinduced electron transfer reaction of $Mo(CNPh)_6$ in chloroform is found to be wavelength dependent and there is evidence for 'hot' electron transfer in this reaction. The ion $Ru(bpy)_2py_2^{2+}$ has been used to model

photosubstitution in $Ru(bpy)_3^{2+}$. Previous evidence suggests that photosubstitution in $Ru(bpy)_2py_2^{2+}$ occurs on a time scale faster than 100 ps. However, it is observed that the photosubstitution is wavelength independent, the classical cage effect apparently absent. Excited state models for each of these systems are presented and discussed. A competitive photosolvation study on $W(CO)_5py$ is presented in an appendix. This study measured the wavelength dependence of the distribution of photoproducts in the photosubstitution of $W(CO)_5py$ in an equimolar mixture of piperidine and triethylamine. Results indicate the preferential formation of the piperidine substitution product at low excitation energy and a statistical product distribution at high excitation energy.

ACKNOWLEDGMENTS:

Thanks to everyone who had an influence on this work, especially those 'Langfordites' from whom I learned, well, just about everything: Joe Lepore, Lalchan Persaud, and Duane Friesen. Thanks to all the other 'Langfordites' whose friendship and camaraderie I value.

Thanks to Prof. Ian Butler and his students at McGill for their overwhelming hospitality. Dev Sharma and Reza Danesh are acknowledged for their expert assistance with the picosecond experiments at Concordia University. The hospitality of Prof. Sandy Kirk and students Garth Irwin and Ian Mackay during a visit to the University of Victoria is warmly acknowledged. To everyone I know at the U of C for being such a pleasure to work with: Thanks.

Finally, Professor Cooper Langford deserves kudos for his energy, enthusiasm, wisdom, and for never once being the rate determining step on anything.

To Mom and Dad.

TABLE OF CONTENTS:

LIST OF TABLES:

LIST OF FIGURES:

CHAPTER ONE: INTRODUCTION

1.1 General Features of Ultrafast Photochemistry

With the development of picosecond and femtosecond pulsed laser systems, a number of photochemical dissociation, fragmentation, and isomerization reactions[1-11] have been shown to occur on subpicosecond time scales. Such time scales correspond to several periods of a typical bond vibration. For example, bond vibration with an infrared absorption at 500 cm^{-1} has a period of vibration of 67 fs.

For these so called ultrafast reactions to occur on the time scale of up to a few bond vibrations, selected molecular vibrations must be coupled to the electronic excitation and lead to the primary photoprocess. These reactions contrast strongly with systems that closely follow the photochemical model of thermally equilibrated excited states, or 'thexi' states.[12] In these systems, the excited states are simply energetic isomers of the ground state and are thermally equilibrated with the surrounding medium. Table 1.1 compares these two extremes of photochemical reactivity.

Femtosecond spectroscopy has shown that reactions such as the photodissociation of NaI[2], I_2[1], and HgI_2[3], the photoisomerizations of stilbene[4] and rhodopsin[5,6], and other reactions occur on the subpicosecond time scale. The time resolution in these studies has

made the observation of wavepacket dynamics possible. A wavepacket is simply the modulus squared of the wave function, ψ.[2]

Table 1.1 Features of Ultrafast (prompt) and Thexi State Photochemistry	
Ultrafast	Thermally Equilibrated Excited States
Relevant time scale is < 1 ps	Relevant time scale is 1 ps - 0.1 s
Photochemical events occur prior to thermal equilibration	Conventional temperature dependences apply
Absence of bound states and weak emission (if any)	Emission typically observed
Highly distorted excited state	Excited state is an electronic isomer of the ground state
Bond motions are coupled to the electronic excitation	Most bimolecular photochemistry is included here
Often very efficient	Less efficient
Examples: photoisomerization of rhodopsin[5,6]; photodissociation of $Cr(CO)_6$[9,10,11]	Examples: $Ru(bpy)_3^{2+}$ electron transfer[13]; photoreduction of benzophenone by benzhydrol[14]

The observation of coherent vibrational wavepacket dynamics is evidence for extreme molecular motions in the excited state. For example, in the 200 fs cis-trans isomerization of rhodopsin, an oscillatory feature in the product absorption has a period of 550 fs and the phase of the oscillation depends on the probe wavelength, with the 180° phase change

occurring at the photoproduct absorption maximum.[6] Such nonstationary vibrational motion in the ground state of the photoproduct suggests that the primary photoprocess (cis-trans isomerization) is itself vibrationally coherent.

The remainder of this introduction presents two theoretical bases for dealing with ultrafast photochemistry in inorganic systems and reviews solvent effects. Spectroscopic techniques capable of providing direct information on ultrafast dynamics are also presented. Last, there is an overview of this dissertation.

1.2 Theoretical Approaches

1.2.1 Heller-Zink Theory

The time dependent theory of semi-classical dynamics was developed initially by Heller[15-17] and then exploited by Zink[18-20] in a number of systems. Time dependent theory applies to electronic absorption, Raman, and electronic emission spectroscopy. It provides a way of determining excited state distortions from electronic absorption (or emission) spectra and pre-resonance Raman spectroscopy.

In electronic absorption spectroscopy, the initial vibrational wavepacket ϕ makes a vertical transition to the potential surface of the excited state. Relative the the ground state, the excited state is typically displaced along the vibrational coordinate. The wavepacket then propagates along the potential surface of the excited state, evolving according to the time dependent Schrodinger equation. Of interest is the overlap of the initial wavepacket ϕ with the time dependent wavepacket $\phi(t)$[20]:

$$1) \qquad \langle \phi_k | \phi(t) \rangle = \exp\left\{ \frac{-\Delta_k^2}{2}(1 - \exp(-i\omega_k t)) - \frac{i\omega_k t}{2} \right\}$$

where k is the normal mode, ω_k is the vibrational frequency, and Δ_k is the displacement of the kth normal mode.

The electronic absorption spectrum (in the frequency domain) is the Fourier transform of the overlap of vibrational wavepackets in the time domain:

$$2) \qquad I(\omega) = c\omega \int_{-\infty}^{\infty} e^{i\omega t} \langle \phi | \phi(t) \rangle$$

where C is a constant, ω is the frequency, and $I(\omega)$ is the photon intensity per unit volume per unit time.

Since the absorption spectrum is the Fourier transform of the time dependent overlap of wavepackets, the features of the absorption spectrum are determined by wavepacket dynamics. Larger vibrational distortions are related to faster movement of the wavepacket and therefore a faster decrease in the initial wavepacket overlap, leading to a broader spectrum. Similarly, small vibrational distortions lead to a narrower spectrum. Vibronic spacing in high resolution absorption spectra is caused by the recurring overlap of wavepackets every vibrational period.

In complex systems where many vibrational modes are displaced in the excited state (most metal complexes), the total wavepacket overlap is:

$$3) \qquad \langle \phi | \phi(t) \rangle = \prod_k \langle \phi_k | \phi(t) \rangle \exp(iE_o t - \Gamma^2 t^2)$$

where E_o is the difference in energy between the minima of the two surfaces and Γ is a damping factor. Combining (1) and (3), the complete overlap is:

$$4) \qquad \langle \phi | \phi(t) \rangle = \exp\left\{ \sum_k \left[\frac{\Delta_k^2}{2}(1 - \exp(-i\omega_k t)) - \frac{i\omega_k t}{2} \right] - iE_o t - \Gamma^2 t^2 \right\}$$

When sufficient vibrational structure is observed in the absorption spectrum, the displacements Δ_k can be calculated from the equations above. Otherwise, a combination of Raman scattering data and electronic spectra must be used. A pre-resonance Raman spectrum corresponds to extremely short time dynamics with a large damping factor. Intensities in the Raman spectrum are related to normal mode displacements by:

$$5) \qquad \frac{I_k}{I_{k'}} = \frac{\Delta_k^2 \omega_k^2}{\Delta_{k'}^2 \omega_{k'}^2}$$

The absorption spectrum in the short time limit is:

$$6) \qquad I(\omega) = c\omega \exp\left[\frac{-(\omega - E)}{2\sigma^2} \right]$$

where $2\sigma^2$ is the width of the absorption spectrum at 1/e of its intensity. $2\sigma^2$ is related to displacements by

7) $$2\sigma^2 = \sum_k \Delta_k^2 \omega_k^2$$

$2\sigma^2$ is determined from the absorption spectrum and ratios of displacements are obtained from the Raman spectrum. Individual displacements Δ_k's (absolute displacements because the sign cannot be determined) are calculated by pairwise comparison of the Raman intensities. Similar procedures can be used when emission spectra are used.

The molecular distortions in the excited states of $W(CO)_5py$[19] and $Mo_2(O_2CCF_3)_4$[18] have been calculated using this combination of pre-resonance Raman and electronic absorption and emission spectra. For $W(CO)_5py$, the calculated bond length changes in its first excited state are given in Table1.2. If large bond length changes are indicative of potential bond scission, then these predict the photochemical dissociation of pyridine - which is observed experimentally.

The Heller-Zink approach to molecular distortions in excited states is based on early time wavepacket dynamics. Vibrational distortions are set in motion promptly after electronic excitation and the effects of this can be observed in electronic spectroscopy. The time dependent theory described here provides a relatively simple means of calculating excited state distortions from spectroscopic data in cases where spectra are favourable.

Table 1.2. Predicted Bond Displacements in $W(CO)_5py$[19]	
Bond	Displacement (Å)
W-N(py)	0.18
W-CO (trans)	0.12
W-CO (cis)	0.04

1.2.2 Hollebone's Octupole Rule

The Heller-Zink approach does not offer a means of *predicting* molecular distortions in the excited state. Hollebone has developed selection rules for vibronic transitions that allow for the prediction of vibrational modes that are coupled to the electronic excitation.[21,22] The basis of these rules is that overall angular momentum must be conserved in a vibronic transition. During the absorption of a photon leading to electronic excitation, the translational and rotational momentum of the photon is converted into internal motions within the molecule (i.e. vibrations). However, molecular translation and rotation are not affected. Thus, the centre of gravity and axes of symmetry remain unchanged. This only occurs if the changes in electronic angular momentum are compensated by opposing internal motions. The result is activation of certain vibrational modes.

By considering the modes of vibration of a sphere of uniform mass density and subduction from spherical symmetry to a lower symmetry such as octahedral, it is possible to define angular momentum quantum numbers for vibrations - analogous to electronic orbital and spin angular momentum quantum numbers. The simplest result from this analysis is the octupole rule:

8) $\Delta L + \Delta S + \Delta V = 3$

ΔL is the change in electronic orbital angular momentum quantum number, ΔS is the change in spin angular momentum quantum number, and ΔV is the change in vibrational angular momentum quantum number. ΔV is defined as: $\Delta V = V_{ex} - V_{gr}$, the difference between vibrational quantum numbers of the excited and ground states. For vibrations above 400 cm^{-1}, $\Delta V = V_{ex}$ because $V_{gr} = 0$.

For d^6 octahedral systems, the first two LF excited states are $^1T(I)$ and $^3T(H)$, where H and I are the atomic terms correlated to the molecular terms. Table 1.3 gives the ΔL, ΔS, and ΔV parameters for these two states. Figure 1.1 shows the vibrations corresponding to $\Delta V = 1, 2$, and 3.

Table 1.3 Ligand field transitions in a d^6 octahedral system and the octupole rule[22]				
Transition	ΔL	ΔS	ΔV	O_h vibration
$^1T_1(I) \leftarrow {}^1A_1(I)$	0	0	3	t_{iu} buckle
$^3T_1(H) \leftarrow {}^1A_1(I)$	1	1	1	t_{1u} stretch

$W(CO)_5py$ has been shown to produce the $W(CO)_5$ fragment from the LF singlet transition[23], which has $\Delta L = \Delta S = 0$ and therefore $\Delta V = 3$. According to the octupole rule, this is associated with the t_{1u} buckle vibrational mode. In the buckle mode, the metal atom is exposed to solvent on one side, making non-specific coordination with the solvent possible. $W(CO)_6$ produces $W(CO)_5$ via the LF triplet transition[24], having $\Delta L = \Delta S = 1$ and $\Delta V = 1$. This is coupled to the asymmetric t_{1u} stretch mode which allows one ligand to dissociate specifically and makes a specific reaction pathway feasible. This explanation has been used to explain why the product from $W(CO)_6$ preferentially binds C=C and -OH functional groups in contrast to randomized vs. functional group coordination seen in the photoproducts of $W(CO)_5py$ in alkene and alcohol solutions.[25]

For spin allowed MLCT transitions, which are dipolar, $\Delta L = 1$ and $\Delta S = 0$. This leaves $\Delta V = 2$. In octahedral symmetry, the vibration corresponding to this is the e_g symmetric

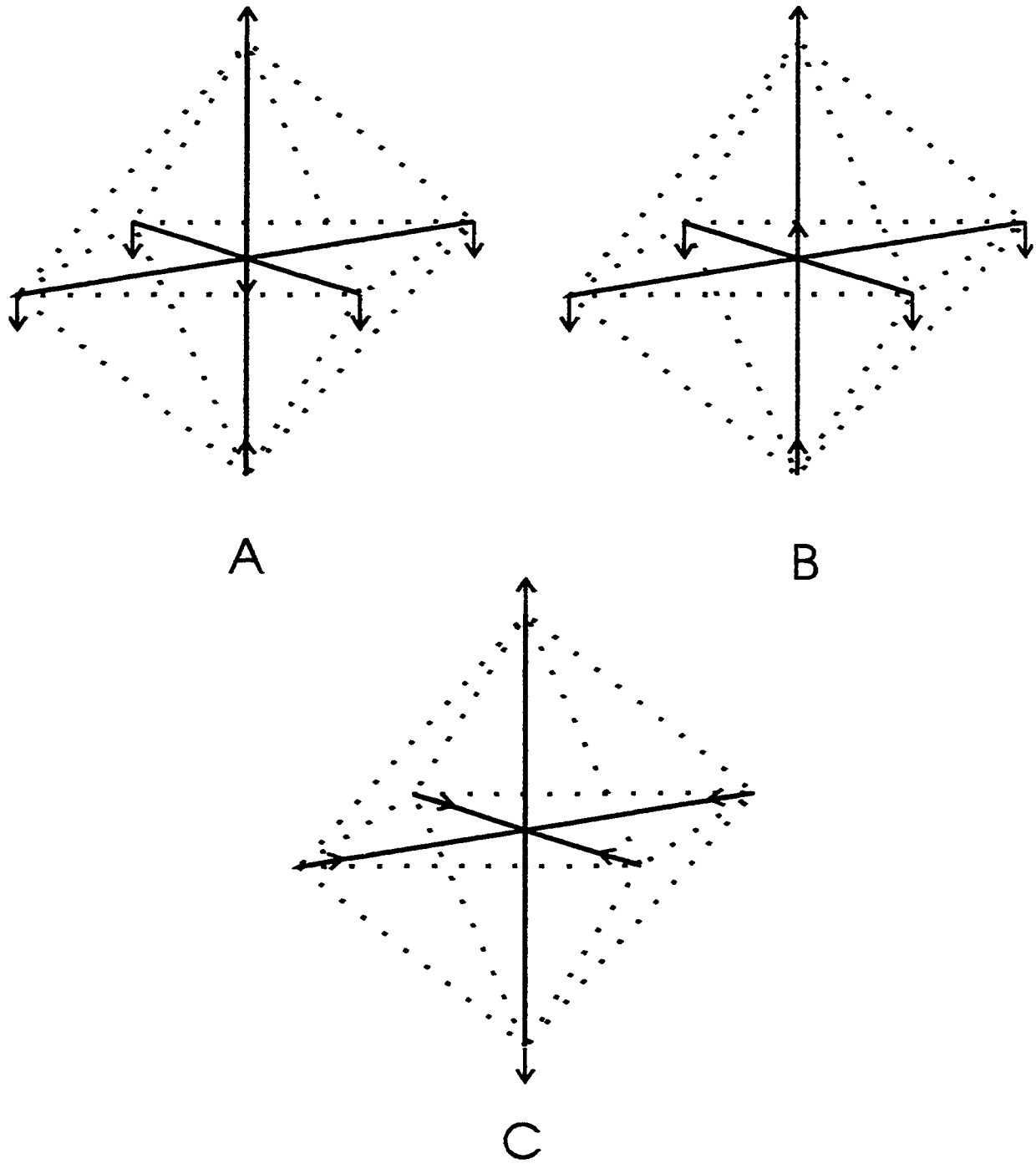

Figure 1.1 Octahedral vibrational modes: A) t_{1u} asymmetric stretch; B) t_{1u} buckle; C) e_g symmetric stretch.

stretch. This vibrational mode is not expected to lead to prompt ligand dissociation. In any octahedral normal mode maintaining gerade symmetry, at least two M-L bonds must be activated. The distribution of excess vibrational energy over more bonds decreases the probability of a prompt ligand dissociation. This may explain the low substitutional reactivity of many MLCT states in octahedral d^6 systems.

1.3 Solvent Effects

1.3.1 Cage Effects:

The mechanical, or classical, cage effect was first identified and modelled by Franck and Rabinowitch for the case of I_2 photodissociation.[26-28] The mechanical cage effect was later expanded in papers by Noyes on the photodissociation of I_2.[29-32] In the mechanical cage effect, the products of a photodissociation are encased in a mechanical 'cage' of solvent molecules. Due to collisions with this solvent cage, the photoproducts may undergo 'geminate' or primary recombination prior to cage escape. This is different from the case of recombination via diffusion, which may occur after initial cage escape. This cage effect acts to reduce the overall quantum yield for dissociation by forcing recombination.

The magnitude of the cage effect was found to be dependent on the wavelength of excitation - the quantum yield increasing at shorter wavelengths.[29,32] The energy of the absorbed light is in excess of the I_2 bond dissociation energy. This excess energy is converted into kinetic energy in the two I atoms produced. The more excess kinetic energy, the greater the probability of cage escape. The viscosity of the solvent also plays a role in the mechanical cage effect. In solvents with low viscosity, the I atoms will achieve greater initial separation and therefore a higher overall quantum yield. The opposite holds for more viscous solvents.

Thus, the results of the mechanical cage effect can be seen in many photodissociation reactions[33-36]: a monotonic decrease in quantum yield with increasing wavelength and an inverse dependence of quantum yield with solvent viscosity, η. The parameter solvent fluidity, $1/\eta$, is typically used diagnostically in studies of the mechanical cage effect.[31,37]

A second type of cage effect has been identified more recently.[38,39] The vibrational cooling times of azulene in various solvents were measured by monitoring the time dependent shifts in the $S_0 \rightarrow S_1$ absorption. When compared to the cooling rate in the gas phase, the liquid phase cooling rates were found to be slower when corrected for increased collision frequencies in the liquid phase. Cooling times are slower in the liquid phase because the solvent acts as a "thermal cage". Initially, energy is transfered from

the vibrationally hot solute to the first solvent shell, which increases local temperature. Heat is then transferred from the immediate surroundings outwards to the rest of the cool medium. As the immediate solvent surroundings become 'hot' due to energy transfer from the hot solute, the rate of energy transfer from the solute to solvent slows down - essentially an example of Newton's Law of Cooling on a microscopic scale. The thermal cage effect is correlated to solvent bulk thermal conductivity, which measures the ability of a solvent to conduct heat away from the immediate solvation shell. Higher solvent thermal conductivity leads to a faster rate of loss of vibrational excitation.

The thermal cage effect is expected to play a role in systems where the photoproducts contain significant vibrational energy, unlike the case of I_2 where excess excitation energy is transformed mainly into kinetic energy in the atomic products. Vibrational relaxation occurs on time scales of 0.1 - 100 ps. Thus, thermal cages are capable of influencing photophysical processes that occur on this time scale.

Langford and Shaw[37] have shown that both mechanical and thermal cage effects are present in the photosubstitution of $W(CO)_5py$, and that the balance of solvent effects was itself wavelength dependent.

For large excitation energy (313 nm), solvent fluidity was found to be an adequate parameter to account for solvents effects on the substitution quantum yield. The excitation energy in excess of the W-py bond dissociation energy was estimated to be > 16600 cm^{-1} (199 kJ mol^{-1}).[37] It is possible that cage escape occurs before energy transfer to solvent thermal cages is extensive.

At 365 and 436 nm, intermediate excitation energies, thermal conductivity and fluidity were both required in order to account for solvent effects. For these wavelengths, increasing thermal conductivity was favourable to product formation. With photoproducts remaining trapped within the solvent cage for a fixed time, prompt cooling to the surroundings may become important. It is possible that rapid cooling is required to prevent recrossing in the neighbourhood of the transition state, which would favour return to the initial complex and ultimate relaxation to the original ground state.

At 458 nm, smaller variations in quantum yield with solvent could not be accounted for by either or both parameters. The lack of significant correlation with solvent dynamic parameters suggests the approach to behaviour associated with a nearly thermally equilibrated excited state - perhaps the triplet. Indeed, it is known that the triplet state can have microsecond lifetimes under certain conditions (i.e. low temperature glasses).[40]

1.3.2 Solvent Friction

In transition state theory (TST), reaction rates are described by treating the reactants as being in equilibrium with the "activated complex" - the transition state reached by reactants at the highest point on the potential energy surface with the most favourable reaction pathway. The activated complex then decomposes to products at a specific rate and no possibility of barrier recrossing is considered.[41] Solvent effects are usually treated as 'static'[42] - where the solvent can perturb energy levels (e.g. the level of the barrier) in the same way that the solvent can perturb ground and excited state energies in solvatochromism.

The solvent can have a dynamic influence on reaction rates and Kramers[43] was the first to recognize that the solvent can cause a breakdown of TST. Considering a one dimensional parabolic reaction barrier associated with a frequency ω_b (similar to the frequency of vibration of a harmonic oscillator; proportional to the degree of curvature of the barrier) and the solvent influence described with a simple Brownian motion model, the dynamic solvent influence is expressed in the transmission coefficient κ, the ratio of observed and predicted rate constants:

$$9) \qquad \kappa = \frac{k}{k_{TST}} = \left[1+\left(\frac{\zeta}{2\omega_b}\right)^2\right]^{1/2} - \left(\frac{\zeta}{2\omega_b}\right)$$

ζ is a friction constant per reduced mass that is experienced by an activated complex interacting with the solvent. When barriers are sharp (large ω_b) and the solvent is fast relaxing (weak friction), reaction rates are well described by TST.[42] In the case of broad barrier reactions (small ω_b) in slow relaxing solvents (high friction), it is the solvent reorientation that becomes rate limiting and[42]

$$\text{rate of crossing} \propto \frac{1}{\text{solvent reorientation time}}$$

In charge transfer processes, the solvent reorientation time used is the longitudinal relaxation time[44,45]:

$$10) \qquad \tau_L = \left(\frac{\varepsilon_\infty}{\varepsilon_s}\right)\tau_D$$

where ε_∞ is the dielectric constant at high frequency (the square of the refractive index, n^2), ε_s is the static dielectric constant, and τ_D is the Debye dielectric relaxation time. The

longitudinal dielectric time is preferred over the Debye time because it has been suggested that polarization relaxation times are shorter for solvent molecules immediately surrounding an ion pair (constant charge conditions) than under the condition of constant potential used to measure τ_D.[46] Table 1.4 gives some examples of dielectric relaxation times of common solvents. These times range fron 0.15 ps to 10.4 ps - time scales appropriate for influencing fast photochemical processes.

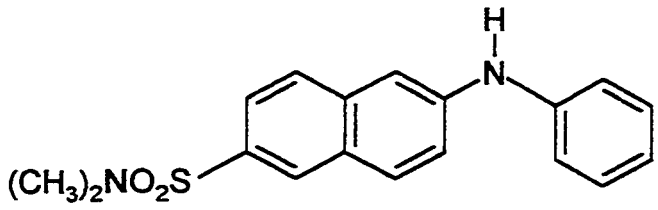

TNSDMA

In the photochemical intramolecular charge transfer of 6-(4-methylphenylamino)-2-naphthalenesulfon-N,N-dimethylamide (TNSDMA), it has been shown that the lifetime of the fluorescence resulting from the back electron transfer is linearly correlated to the longitudinal dielectric relaxation time of the solvent.[44] While this example is not specifically for an ultrafast process, it shows that solvent friction can influence processes that occur from excited states.

Table 1.4 Dielectric Relaxation Times for Selected Common Solvents at 20°C				
Solvent	τ_D (ps)	ε_s[a]	ε_∞[a]	τ_L (ps)
Water	6.8[b]	80.16	1.78	0.15
MeOH	47[c]	32.66	1.76	2.5
EtOH	138[c]	24.55	1.85	10.4
Chloroform	5.4[d]	4.806	2.09	2.3
Pyridine	7.3[e]	13.55	2.30	1.2
Toluene	5.1[d]	2.379	2.24	4.8
Chlorobenzene	11.8[e]	5.69	2.56	5.31
MeCN	3.8[d]	35.94	1.81	0.19

a) taken from reference 47; b) taken from reference 48; c) taken from reference 49; d) taken from reference 50; e) taken from reference 51.

A femtosecond time resolved study of the fluorescence spectral shifts of coumarin 343 in water showed that water undergoes an initial response faster than 50 fs and accounts for >50% of the total solvent response to the charge redistribution between ground and excited states.[52] This initial response was assigned to rotational and librational motions of water and the following slower component (up to 1 ps) was assigned to diffusive motions. Note that these time scales are on the order of the longitudinal dielectric relaxation time for water.

In reactions with little or no charge redistribution, insights into solvent dynamics have come largely from molecular dynamics simulations.[42] An example is the thermal boat-chair isomerization of cyclohexane[53], for which the transition state crossing occurs in the femtosecond domain. The rate of boat-chair interconversion is accelerated by increasing pressure. This observation can be explained by TST if the volume of activation is negative. However, theoretical calculations using intermolecular potential functions show that this is not the case. The explanation for the pressure effect must come from solvent dynamics.

The interconversion between boat and chair forms can be described by two coordinates: a hindered rotation coordinate θ which takes a molecule from a chair to a boat configuration or vice versa; and a secondary cyclic generalized coordinate φ that takes a molecule to another degenerate configuration (eg. chair $\leftrightarrow$ chair). These coordinates depend on the positions of all six carbon atoms.

To study the solvent dynamic effects on this reaction[53], the differential work done by the solvent on the solute as it passes through the transition state was analyzed. This was done according to:

11) $$W(\theta,\theta',t_1,t_2) = -(t_2 - t_1)^{-1} \int_{t_1}^{t_2} \theta' \langle \delta V | \delta\theta \rangle dt$$

where W is the rate of work done between times t_1 and t_2 for a given θ and its time derivative θ'. V is the total potential energy of the solute-solvent interaction. A set of trajectory simulations used to calculate the thermal rate constants of chair-boat interconversion in carbon disulfide solvent was used for this calculation.

Trajectories were divided into those that *recross* the transition state and those that do not. The non-recrossing trajectories caused the solvent to do negative work on the reaction coordinate, thus cooling the molecule. The recrossing trajectories did not show any net energy transfer to the solvent. These recrossing trajectories account for the deviation from TST. The mechanism for the pressure acceleration is due to favourable formation of solvent cages that cool activated trajectories, thereby decreasing the number of recrossing trajectories that would lower the overall rate of interconversion.

In order for a reaction to proceed to completion, the system must dissipate energy after crossing through the transition state. When there is too much excess energy remaining for too long a time, the system can recross the barrier and ultimately fail to convert to products.[42] The discussion of solvent cages, especially thermal cages, above is quite

relevant to this issue. However, the only discussion of the dynamic effects of thermal cages has been for $W(CO)_5py$.[37]

1.4 Spectroscopic Tools

Time resolved spectroscopic techniques are now capable of time resolution under 50 fs.[6] As discussed above, this allows for the direct observation of wavepacket dynamics. Time resolved spectroscopies are a most powerful tool in understanding the mechanisms of ultrafast photochemical reactions. While femtosecond spectroscopy provides the greatest time resolution, picosecond and nanosecond spectroscopies remain very useful - especially when more than one excitation wavelength can be used. Both picosecond and nanosecond absorbance spectroscopies are used extensively in this work and are described in chapter two.

A type of spectroscopy that can provide useful information about molecular distortions in the excited state is resonance Raman spectroscopy. Its use in the application of Heller-Zink theory has been mentioned above. In resonance Raman spectroscopy, the excitation source is in resonance with an electronic absorption of the compound of interest.[54] If a Raman line becomes stronger under resonance conditions, then the molecule is distorted along the normal coordinate (corresponding to that line) during the electronic

transition.[55] Thus, resonance Raman can provide detailed information about the vibrational modes that are coupled to the electronic excitation and that may lead to ultrafast photochemistry. This technique has been applied to the photochemistry of $Cr(CO)_6$[11] and $[CpFe(CO)_2]_2$.[56] It was also applied to $Cr(CNPh)_6$[57], one of the compounds studied in this work, the results of which will be discussed.

1.5 Overview of Dissertation

Of recent interest in inorganic photochemistry is the problem of photosubstitution arising from the excitation of low lying metal-to-ligand charge transfer (MLCT) states.[34-36,57,58] MLCT states are generally considered to be unreactive towards substitution because they have little metal-ligand antibonding character.[59] Substitutions from MLCT states are expected to be associative in nature due to the increased positive charge at the metal centre.

It has become increasingly clear that substitutions arising from MLCT excitations can be very efficient and follow dissociative mechanisms. The most common model for this reactivity is thermal population of higher lying antibonding ligand field (LF) states, from which ligand dissociation is known to occur.[34]

This dissertation covers the photochemistry of three d^6 metal complexes in which the lowest lying excited states are MLCT states and photosubstitution occurs on direct excitation into these states. The three systems studied here have different photochemical reactivities and wavelength dependences. The wavelength dependence of quantum yields or time resolved kinetics provides useful information about photochemical mechanism. It has been exploited in each of the three systems studied here. Most of the mechanistic conclusions are obtained directly from the interpretation of wavelength dependence.

The first compound investigated, $Cr(CNPh)_6$, is believed to undergo ligand dissociation in < 1 ps at 300 nm.[60] This places the photosubstitution in the ultrafast category. $Cr(CNPh)_6$ exhibits complex photochemistry - having both substitution and electron transfer modes of reactivity.[61] The wavelength dependences of photoinduced electron transfer, photosubstitution, and time resolved spectra and kinetics are all used to probe the photochemical mechanisms of this system.

The second compound, $Mo(CNPh)_6$, was investigated to compare with $Cr(CNPh)_6$ photochemistry. Again, the wavelength dependences were used to probe mechanism. The behaviour of these chromium and molybdenum arylisonitrile complexes is compared.

The third compound, $Ru(bpy)_2py_2^{2+}$, has been used to model photosubstitution in the well known photosensitizer $Ru(bpy)_3^{2+}$.[62] This compound has been shown to exhibit ultrafast, or semi-ultrafast behaviour and was chosen for study on this basis. The wavelength dependence of photosubstitution is used to draw conclusions about mechanism.

CHAPTER TWO: EXPERIMENTAL

2.1 Materials and Synthesis

2.1.1 Purification of Reagents

Table 2.1 Solvents purified by distillation and the corresponding drying agents

Solvent	Drying agent in distillation
Acetone	calcium hydride
Benzene	sodium benzophenone ketyl
Chloroform	calcium hydride
Ethanol	calcium hydride
Acetic Acid	P_2O_5
Methanol	calcium hydride
Pyridine	calcium hydride
Tetrahydrofuran	sodium benzophenone ketyl
Toluene	sodium benzophenone ketyl

Table 2.1 gives a list of solvents that required purification before use in quantum yield measurements or syntheses of metal complexes . All other materials were used as received from Aldrich (tert-butylamine, pyromellitic dianhydride, ammonium

hexafluorophosphate), BDH (chloroform, dichloromethane, ethyl acetate, acetic anhydride, ethanol, sodium hydroxide, potassium carbonate, P_2O_5), or Fisher (aniline, ammonium thiocyanate, ammonium dichromate, chromic chloride). Molybdenum hexacarbonyl (Aldrich) was purified by sublimation. Benzoquinone (Fisher) was recrystallized from hexane to give bright yellow needles.

2.1.2 Phenylisocyanide

Phenylisocyanide was prepared by the reaction of aniline with chloroform in the presence of a base.[63] Chloroform (10 mL; 0.23 mol), aniline (19 mL; 0.21 mol), dichloromethane (40 mL), aqueous sodium hydroxide (30 g NaOH in 60 mL H_2O), and benzyltriethylammonium chloride (0.31 g; 0.0014 mol) were stirred vigorously for three hours at room temperature in a 500 mL flask equipped with a condenser. 200 mL of water was added to quench the reaction. The mixture was transferred to a separatory funnel and the organic layer was washed once with distilled water (50 mL) and three times with brine (3 x 50 mL). The organic layer was dried over K_2CO_3 overnight. Phenylisocyanide is purified by vacuum distillation (75 - 78°C on a water aspirator at 10-15 torr). Yield is 15 g (74%). Phenylisocyanide is highly toxic and should always be handled in a hood.

2.1.3 Bis(*tert*-butyl) pyromellitic diimide

Pyromellitic diimides (benzene-1,2,4,5-tetracarboxydiimides) are prepared by the dehydration of the dianhydride in the presence of primary amines (see references 64 -66 for examples). Pyromellitic dianhydride (1.86 g; 0.0085 mol) and excess *tert*-butylamine (2 mL; 0.0188 mol) were refluxed for 22 hours in dimethylformamide (40 mL) in a 250 mL round bottom flask equipped with a condenser and drying tube. Once cool, the mixture was poured into 500 mL of water and the precipitate was filtered. Purification was by recrystallization from ethyl acetate. Yield = 1.7 g (66%) ^{1}H-NMR: δ 1.72 (s, 18 H), 8.14 (s, 2H). Elemental analysis: Calculated for $C_{18}H_{20}N_2O_4$: C, 65.83; H, 6.15; N, 8.53. Found: C, 65.73; H, 6.20; N, 8.46.

2.1.4 Hexakis(phenylisocyanide)chromium(0)

$Cr(CNPh)_6$ was obained through the reaction between chromous acetate and phenylisocyanide in methanol.[67] A slurry of $Cr_2(OAc)_4 \cdot 2\ H_2O$ (8.23 g; 0.0219 mol) in methanol (20 mL) was added to phenylisocyanide (30.0 g; 0.291 mol). The chromous acetate immediately dissolves and the dark mixture was stirred for one hour at 45°C. The mixture was then cooled to 0°C and a bright red precipitate formed. The precipitate was filtered, washed twice with cold methanol (2 x 10 mL), and recrystallized from

toluene/ethanol. Purified yield = 0.17 g (2%). The reaction proceeds via a thermodynamically unfavourable disproportionation mechanism (see $E^{o'}$s in reference 68) , explaining the low yield. Elemental analysis: Calculated: C, 75.20; H, 4.52; N, 12.53. Found: C, 75.04; H, 4.57; N, 12.86.

2.1.5 Tetrakis(acetato)dimolybdenum(II)

Tetrakis(acetato)dimolybdenum(II) was prepared according to Cotton.[69] A mixture of $Mo(CO)_6$ (2.01 g; 0.0076 mol), acetic anhydride (10 mL), and glacial acetic acid (100 mL) was refluxed for 20 hours under nitrogen. The brown/yellow solution was cooled to room temperature and the yellow crystals filtered and washed with ethanol (2 x 30 mL) and ether (2 x 50 mL). The product was dried in vacuo. Yield and purity were not determined.

2.1.6 Hexakis(phenylisocyanide)molybdenum(0)

Hexakis(phenylisocyanide)molybdenum(0) was prepared according to Mann.[70] All procedures were performed under a nitrogen atmosphere. $Mo_2(CH_3COO)_4$ (1.0 g; 0.0023 mol) was slurried in methanol (40 mL). A solution of phenylisocyanide (10 mL; 0.097 mol) in methanol (20 mL) was added to the slurry by needle transfer. The mixture

immediately turned brown. The reaction mixture was stirred for one hour in the dark. The product precipitated as a red powder. The product was filtered and washed with methanol (20 mL) and then recrystallized from toluene. After filtration, the crystals were washed twice with toluene (2 x 5 mL) to remove any phenylisocyanide. The final red crystals have yellow/green reflectances. Yield = 0.48 g (86% based on the disproportionation reaction). Purity was established by comparison to published UV-visible spectra.

2.1.7 *cis*-Bis(bipyridine)bis(pyridine)ruthenium(II) bis(hexafluorophosphate)

$[Ru(bpy)_2py_2][PF_6]_2$ was prepared according to Dwyer et al.[71] $[Ru(bpy)_2Cl_2] \cdot 2H_2O$ (0.246 g; 5.1×10^{-4} mol) and pyridine (1 mL) were heated in 15 mL H_2O/MeOH (1:1; v:v) at 80°C for three hours. The reaction mixture was filtered hot. Ammonium hexafluorophosphate (0.53 g; 3.25×10^{-3} mol) was added to the filtrate, producing an orange precipitate. The precipitate was filtered on a glass frit and washed with cold H_2O (10 mL). Purification was by recrystallization from acetone/H_2O (1:1; v:v) in the presence of excess NH_4PF_6. The crystallization was allowed to proceed overnight at 5°C. The crystals were filtered and washed with cold H_2O (10 mL). Purified yield = 0.26 g (60%). Elemental analysis: Calculated: C, 41.80; H, 3.05; N, 9.76. Found: C, 41.44; H, 3.00; N, 9.73.

2.1.8 Potassium Reineckate, $KCr(NH_3)_2(NCS)_4$

Reinecke's salt, $[NH_4][Cr(NH_3)_2(NCS)_4]$, was prepared by slowly adding 5 g $(NH_4)_2Cr_2O_7$ to 15 g of fused NH_4NCS (melted in an aluminum beaker with a bunsen burner).[72] The reaction is very exothermic and results in a hard, red mass once cooled. The mass is powdered using a mortar and pestle and washed with hot ethanol (50 mL) to remove unreacted NH_4NCS. $[NH_4][Cr(NH_3)_2(NCS)_4]$ is dissolved at 50°C in water and excess KNO_3 is added. When cooled, the $KCr(NH_3)_2(NCS)_4$ precipitate is filtered and recrystallized from 50°C water containing KNO_3. The product is dried over P_2O_5, and then in a 110°C oven. Yield of anhydrous potassium reineckate is 3.3 g (26%).

2.1.9 Potassium Ferrioxalate, $K_3Fe(C_2O_4)_3 \cdot 3H_2O$

Potassium ferrioxalate was prepared previously in the laboratory according to the procedure given by Calvert and Pitts.[73] Three volumes of a 1.5 M $K_2C_2O_4$ solution were mixed with one volume of a 1.5 M $FeCl_3$ solution and the crystals were allowed to precipitate overnight. The product was recrystallized three times from warm water and dried in a 40°C oven. The yield of green crystals was 15 g.

2.2 Steady State Quantum Yield Measurements

Steady state reactions were monitored by UV-visible spectroscopy. Molar absorptivities of reactants were determined by measuring the absorbance of solutions with an accurately weighed quantity of the appropriate compound. Molar absorptivities of products were determined by irradiating samples with known concentrations of reactant to 100% conversion and measuring the absorbance. Extinction coefficients measured this way have uncertainties of in the range of 5-10%. Absorption spectra for extinction coefficients and quantum yield measurements were recorded using a Hewlett Packard model 8452A diode array spectrophotometer interfaced to a PC computer. Resolution of the instrument is $\pm$ 2nm.

All samples were prepared in the dark with a red safety light. Due to the air sensitivity of many of the solutions, all samples were subject to 3-5 freeze/pump/thaw cycles (in the cell) under nitrogen to remove traces of oxygen. Solvents and solutions were transferred under nitrogen using transfer needles or syringes. Solutions were typically prepared first in a Schlenk tube and then transferred to the cell via a needle. Glassware was cleaned and then dried in a 110°C oven for one hour before use. The concentration of a metal complex was chosen such that samples absorbed >99% of light at the irradiation

wavelength. $Ru(bpy)_2py_2^{2+}$ concentrations ranged between 3×10^{-4} and 4×10^{-4} M. $Cr(CNPh)_6$ and $Mo(CNPh)_6$ concentrations were between 4×10^{-5} and 5×10^{-4} M.

One quartz cell was circular (Hellma, 1 cm pathlength, 19 mm diameter, 2.8 mL volume) with a fused quartz-glass joint to a teflon stopcock and side arm with bulb for freeze/pump/thaw cycles. A separate matched circular cell was used for ferrioxalate and reineckate actinometry. A rectangular quartz cell (1 cm pathlength, 4.1 mL volume) with similar attachments was used for irradiations of samples when fulgide actinometry was used. The fulgide actinometer was sealed in an identical, optically matched cell. In both arrangements, samples and actinometer solutions were stirred continuously during irradiations with a blue magnetic stir bar (9 mm long, 2 mm diameter) rotating perpendicular to the incident light.

The light source for 313, 365, 436, 488, and 532 nm was a PRA model ALH 215 xenon medium pressure arc lamp (150 W) coupled with the appropriate interference filter. For 514.0 nm, a Spectra-Physics model 164 argon ion laser was used. The light sources were attenuated with neutral density filters to obtain intensities appropriate for measurements of small, accurate absorption changes over time intervals of 15-60 s. A schematic of the optical trains used for irradiations is in Figure 2.1.

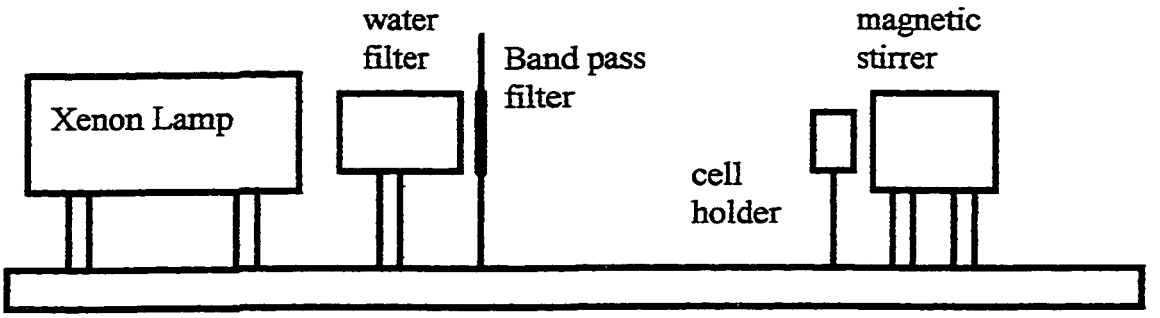

Irradiations using Xe lamp

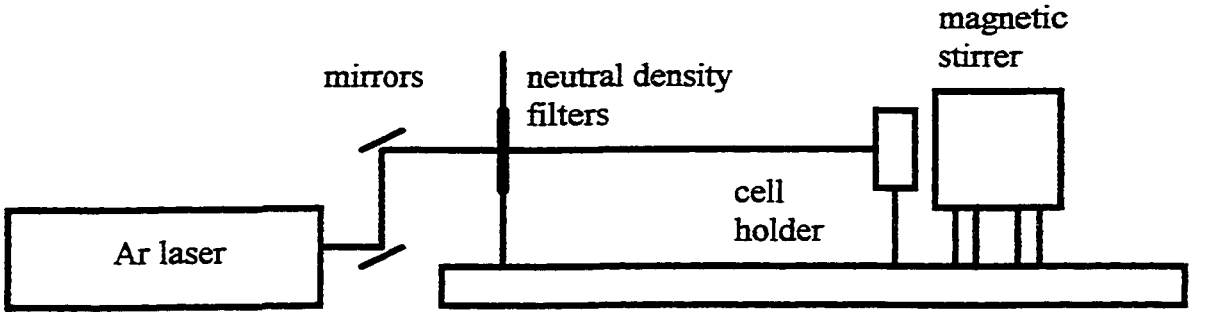

Irradiations using Argon laser

Figure 2.1 Schematic diagrams for optical trains used in quantum yield determinations.

The calculation of moles of product formed can be obtained by monitoring the decrease of reactant absorption (electron transfer reactions) or by increase of product absorption (all substitution reactions). The relevent calculations are given below.

Light intensities at 313, 365, and 436 nm were determined using the potassium ferrioxalate actinometer based on the photochemical reduction of Fe^{3+}.[74] Light intensities at 488, 514, and 532 nm were determined by either Reineckate actinometry[75], based on the photoaquation of the Reinecke anion, or by fulgide actinometry[76], based on the reversible ring closure of the commercially available compound Aberchrome 540.

For 313 and 365 nm, 0.006 M ferrioxalate solutions were used. For 436 nm, 0.15 M ferrioxalate solutions were required for conditions of >99% light absorption. 0.006 M ferrioxalate was prepared by dissolving 0.3 g $K_3Fe(C_2O_4)_3 \cdot 3H_2O$ in 100 mL 0.1 M H_2SO_4. 0.15 M ferrioxalate was prepared the same way, but with 7.4 g $K_3Fe(C_2O_4)_3 \cdot 3H_2O$. A 0.1% phenanthroline developer solution was prepared by dissolving 0.5 g of 1,10-phenanthroline in 500 mL of deionized water. A buffer solution consisting of 41 g $NaCH_3COO \cdot 3H_2O$ and 5 mL of conc. H_2SO_4 diluted to 500 mL with deionized water was also prepared. Following irradiation of the appropriate ferrioxalate solution (2.8 mL), the irradiated solution was transferred quantitatively to a 25 or 50 mL volumetric flask containing 1.5 mL of the buffer solution. 6 mL of the phenanthroline developer was then

added. The colour was allowed to develop for at least one hour before diluting to volume and measuring the absorbance at 510 nm. Deionized water was used throughout. A blank was prepared by performing all of the above procedures on a ferrioxalate solution that was not exposed to the irradiation source. The blank was used to correct for background light sources.

In Reineckate actinometry, the free NCS^- formed from the photoaquation of $KCr(NH_3)_2(NCS)_4$ is analyzed. Actinometer solutions of $KCr(NH_3)_2(NCS)_4$ were made to absorb >95% of the incident light. Solutions were made immediately before the irradiation and were filtered through 50 μm nylon filters to remove particulates. A dark blank sample for each solution is required in order to correct for thermal aquation and background light sources. The developer solution consisted of 0.1 M $Fe(NO_3)_3$ and 0.5 M HNO_3 in distilled water. Following irradiation, the blank and irradiated samples (2.8 mL each) were diluted quantitatively up to 25 mL using developer solution. The absorbance of each developed solution was measured at 450 nm. This wavelength corresponds to the strongly absorbing iron-thiocyanate complex that is formed. A new reineckate solution was prepared for each measurement in order to minimize the effects of thermal aquation.

The reineckate actinometer was calibrated against the ferrioxalate actinometer at 436 nm. The results (Table 2.2) show that there is less than 1% error between the actinometers, and no correction was necessary.

Table 2.2 Comparison of 436 nm Light Intensities Measured by Ferrioxalate and Reineckate Actinometers

Time*	Ferrioxalate (photons/sec)	Reineckate (photons/sec)
1:30 pm	2.92×10^{15}	2.86×10^{15}
2:30 pm	3.03×10^{15}	3.03×10^{15}

*Light intensities can fluctuate over time as the lamp warms up.

Fulgide actinometry can be used to measure light intensities of either ultraviolet or visible radiation.[76] Irradiation in the UV (< 400 nm) leads to the conrotatory ring closure of Aberchrome 540 (1→2 in Figure 2.2), leading to colour formation. Visible irradiation leads to ring opening and photobleaching (2→1). Fulgide actinometry was only used for visible irradiations (488, 532 nm) because it was observed that it gave incorrect intensities for wavelengths < 450 nm when compared to ferrioxalate actinometry. The discrepancy between ferrioxalate and fulgide actinometry became worse over repeated use of the fulgide actinometer, presumably due to the formation of a byproduct that

absorbs ultraviolet light but does not react photochemically. Visible actinometry was not affected.

The fulgide actinometer was prepared by dissolving approximately 9 mg of Aberchrome 540 into 4.1 mL of dry, distilled toluene, sealed in a quartz cell equipped with a teflon stopcock under nitrogen. Several actinometer readings were taken for each experiment and averaged. When the absorbance of the actinometer at the irradiation wavelength fell below 2.0, the actinometer was exposed to UV light to generate more of compound (2), which absorbs in the visible.

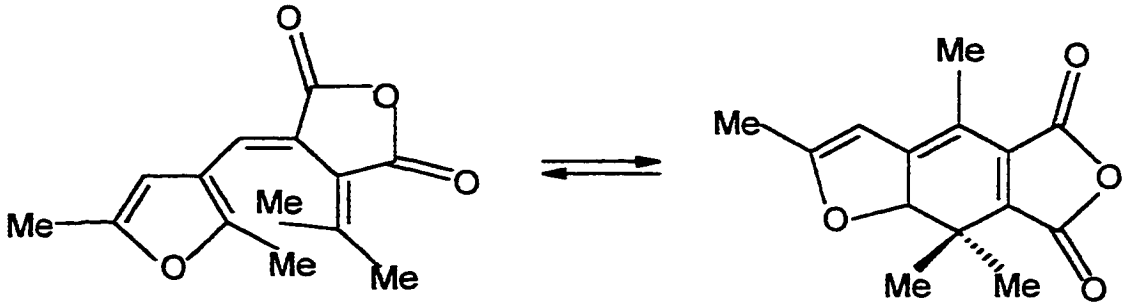

(1) (2)

Figure 2.2 The photoisomerization of Aberchrome 540. Compound (1) does not absorb in the visible, but compound (2) has a strong visible absorption.

The errors in quantum yields reported in the results refer to the reproducibility of the measurement as reflected in the standard deviation of 3-10 trials. Systematic errors may

account for differences between the actual and measured quantum yields on the order of 10%. This is much larger than reproducibility errors which are typically below 5% of the measured quantum yield. Thus, the quantum yields reported in the results are precise enough to report trends, but are not accurate to better than 10% of the actual yield.

Calculations:

A. Moles reacted

i) Calculation of molecules product formed by monitoring decrease of reactant

$$A_r^t = A_{Total}^t - \left[\frac{A_o - A_{Total}^t}{\varepsilon_r - \varepsilon_p}\right] \cdot \varepsilon_p$$

$$n_p = \left(\frac{A_o - A_r^t}{A_o}\right) \cdot [\text{reactant}] \cdot V \cdot A$$

ii) Calculation of molecules product formed by monitoring increase of product

$$A_p^t = \left[\frac{A_o - A_{Total}^t}{\varepsilon_r - \varepsilon_p}\right] \cdot \varepsilon_p$$

$$n_p = \left(\frac{A_p^t}{A_{100}}\right) \cdot [\text{reactant}] \cdot V \cdot A$$

A^t_{Total} = total absorbance at time t

A_o = total absorbance at t = 0 (no irradiation)

ε_r, ε_p = molar absorptivity of reactant or product ($M^{-1}cm^{-1}$)

A^t_p, A^t_r = corrected absorbance (product or reactant only)

[reactant] = initial concentration of reactant (M)

V = volume of cell

A = Avogadro's number (6.023×10^{23} molecules/mole)

A_{100} = absorbance at 100% conversion (product only)

n_p = number of molecules or product formed

B. Calculation of light intensity

i) Ferrioxalate actinometry

$$n_{Fe} = \frac{A_{510} V_1 A}{V_2 V_3 \varepsilon_{Fe} l}$$

$$I_a = \frac{n_{Fe}}{\phi_{fe} I_f t}$$

n_{Fe} = number of Fe^{2+} molecules produced

A_{510} = absorbance of Fe^{2+} complex at 510 nm

V_1 = volume irradiated (2.8 mL)

V_2 = volume complexed (2.8 mL)

V_3 = total volume of developed solution (25 or 50 mL)

ε_{Fe} = molar absorptivity of Fe^{2+}(phenanthroline) at 510 nm (1.11×10^4 $M^{-1}cm^{-1}$)

l = path length (1 cm)

I_a = number of photons per second

ϕ_{Fe} = quantum yield for formation of Fe^{2+} (1.24 @ 313 nm; 1.21 @ 365 nm; 1.01 @ 436 nm)

I_f = fraction of light absorbed by actinometer ($\cong$ 1)

t = irradiation time (s)

ii) Reineckate actinometry

$$n_{NCS} = \frac{A_{450} V_1 A}{V_2 V_3 \varepsilon_{NCS} l}$$

$$I_a = \frac{n_{NCS}}{\phi_{NCS} I_f t}$$

n_{NCS} = number of NCS^- molecules produced

A_{450} = absorbance of iron-thiocyanate complex at 450 nm

V_1 = volume irradiated (2.8 mL)

V_2 = volume complexed (2.8 mL)

V_3 = total volume of developed solution (25 or 50 mL)

ε_{NCS} = molar absorptivity of iron-thiocyanate complex at 450 nm (4.3×10^3 $M^{-1}cm^{-1}$)

l = path length (1 cm)

I_a = number of photons per second

ϕ_{NCS} = quantum yield for formation of NCS^- (0.30 @ 488 nm))

I_f = fraction of light absorbed by actinometer ($\cong$ 1)

t = irradiation time (s)

iii) Fulgide actinometry

The quantum yield for bleaching of the fulgide (process 2→1 in Figure 2.2) is dependent on temperature and excitation wavelength. At 21°C, ϕ is given as:

$\phi = 0.178 - (2.4 \times 10^{-4} \times \lambda_{ex})$

where λ_{ex} is the excitation wavelength. The bleaching process was monitored at 560 nm. Plots of ΔA_{560} vs. Δt were made and the slope substituted into the following equation to obtain the light intensity:

$$I_a = \left[\frac{\Delta A_{560}}{\Delta t}\right]\left[\frac{A}{\varepsilon_{560} V l}\right]\left[\frac{1}{\phi I_f}\right]$$

I_a = number of photons per second

$\Delta A_{560} / \Delta t$ = slope from plots of absorbance vs. time

A = Avogadro's number (6.023×10^{23} molecules/mole)

$\varepsilon_{560} = 1315\ M^{-1}cm^{-1}$

V = volume of cell (4.1mL)

l = path length (1 cm)

ϕ = quantum yield for bleaching (see above)

I_f = fraction of light absorbed by fulgide ($\cong$ 1)

C. Quantum yield

$$\Phi = \frac{n_p}{I_{f,r} I_a t}$$

$I_{f,r}$ = fraction of light absorbed by reactant

t = irradiation time (s)

2.3 Time Resolved Spectroscopy

2.3.1 Nanosecond Flash Photolysis

The nanosecond flash photolysis experiments were performed in the chemistry department at the University of Victoria.[77] The flash photolysis apparatus uses a Spectra Physics YAG laser model GCR-12 (355 nm $\leq$ 70 mJ/pulse; 532 nm $\leq$ 150 mJ/pulse). Laser pulse energies are attenuated to less than 20 mJ using neutral density filters. The

laser excitation source and the analyzing beam are oriented at 90° to each other. The analyzing beam is from a pulsed 150 W Xenon lamp (Oriel housing model 66057, power supply PTI model LPS-220). Light from the probe beam passes through a monochromator (CVI Digikrom 240) to separate wavelengths. The light intensities at fixed wavelengths are detected using a photomultiplier (Hamamatsu 240). The voltage for the photomultiplier tube (PMT) is set using a programmable power supply interfaced to a computer. Timing for laser pulsing, lamp pulsing, and detection are controlled by a custom built pulse generator driving a Stanford Research System delay generator Model DG535. Time resolution is 20 ns.

Light intensities for the background light intensity, or ground state signal, (V_o) and the transient signal (V_t) are measured on a Tektronix TDS 520 digital oscilloscope. The entire system is integrated to a MacIntosh IIci computer, with all of the components interfaced to a GPIB bus. The computer program controlling the experiments was written using Labview 3.1.1 (National Instruments). This program converts the data collected (V_t) on the oscilloscope into units proportional to absorbance values:

$\Delta A = \log(V_t)-\log(V_o)$

In this case, ΔA is not a change in true absorbance units because the lamp intensity before passing through the sample is not taken into account in this single beam setup.

Cells were custom made and had a 0.7 cm pathlength. Cells were equipped with septa and all samples were continuously bubbled with nitrogen via a small needle. Absorbance measurements were taken before and after experiments to determine the extent of photolysis, which was kept to below 20%. Absorbance values before flash photolysis were less than 0.2 at the wavelength that was monitored. Higher absorbances would lead to errors due to non-linear PMT response.

2.3.2 Picosecond Flash Photolysis

Picosecond studies were performed at the Canadian Centre for Picosecond Laser Spectroscopy, Montreal, Quebec.[23] A schematic for the picosecond flash photolysis apparatus is in Figure 2.3. The excitation source is a mode locked Nd:YAG laser (Quantel YG 402G) with a 1064 nm fundamental output wavelength. Passive mode locking is obtained with a solution of the dye Q-switch I (Kodak 9470). A train of 12 picosecond pulses is emitted and an appropriate one is selected by a Quantel PF 302 pulse selector. The selector consists of a Glan-air polarizer to remove the minor vertical component of light, a pockels cell (a birefringent crystal of KD*P, potassium deuterium phosphate) to change the polarity of one pulse, and a second polarizer to select the unique pulse. The first few rejected mode locked pulses trigger electronics to supply a short, high voltage through the pockels cell to make it birefringent. The duration of the

voltage is such that only one pulse is rotated through 90° and can pass through the second polarizer. The selected pulse is successively amplified by two Nd:YAG rods (Quantel SF 410-07 and SF 410-09 respectively).

The amplified 1064 nm pulse is frequency doubled to 532 nm with approximate 20% efficiency by passing through a KD*P type I crystal. Subsequent passage of the combined 532 and 1064 nm pulse through a KD*P type II crystal produces the third harmonic by frequency mixing. The frequency mixing technique does not convert all of the 1064 nm light into the third harmonic. 1064, 532, and 355 nm wavelengths are separated using dichroic mirrors. The remaining 1064 nm fundamental is focused into a Raman active aqueous solution of D_3PO_4 (50% D_2O by volume) and results in the generation of a transient birefringent to produce Stokes and anti-Stokes Raman effects. This produces a pulse of 400 - 700 nm white light continuum with the same temporal pulse width as the laser pulse, to be used as a probe pulse. 355 and 532 nm wavelength components are used independently as pump pulses. The pump pulse is passed along a delay line to vary its arrival time relative to the probe pulse from 0 ps to 10 ns. Final pump and probe pulses are 35 ps at half maximum intensity. Pump energies are between 1.0 and 2.5 mJ per pulse.

The probe pulse is split into reading (I) and reference (I_o) pulses. The ground state absorption of the sample is taken before excitation and the excited state absorption is taken after excitation. Reading and reference probes are passed through a double monochromator and then a detection system consisting of two silicon enhanced photodiode arrays corresponding to I and I_o, each containing 250 diodes which detect specific wavelengths. Signals are sent to a microcomputer (PAR) and analyzed on a PC to calculate excited state absorptions.

An average of 7-8 excited state and ground state absorptions are taken for each time delay in an experiment. Rejection of a sample shot resulted from: 1) the pump pulse being too high or to low in energy; 2) a double train of pulses coming from the oscillator; 3) saturation of the photodiodes by a probe pulse; 4) generation of an unsatisfactory continuum in the D_3PO_4 cell. In the calculation stage, a shot was rejected if the noise was too high. For these experiments, sample shots with noise values greater than 7 were rejected.

Samples for picosecond spectroscopy were in 2 mm quartz cell fitted with a glass bulb for freeze/pump/thaw cycles and a teflon stopcock. All samples were degassed by 3-5 freeze/pump/thaw cycles. Concentrations of metal complex were adjusted so that

absorbances were between 0.2 and 0.5 in order to stay in the linear range of the detection system.

Calculations:

a) Noise:

$$N_i = \sum_k \frac{(a_{ik} - a_k)^2}{a_k}$$

N_i = noise for the spectrum

a_{ik} = the absorbance change at each shot at wavelength k

a_k = average absorbance at wavelength k for all shots of a specific time delay

b) Absorbance change

$$\Delta A = Log\left[\frac{I_{o,ex}}{I_{ex}}\right] - Log\left[\frac{I_{o,gr}}{I_{gr}}\right]$$

$I_{o,ex}$, $I_{o,gr}$ = continuum intensity for excited state or ground state absorbance measurement

I_{ex} = transmitted light intensity for excited state (after pump pulse)

I_{gr} = transmitted light intensity for ground state (determined with no excitation)

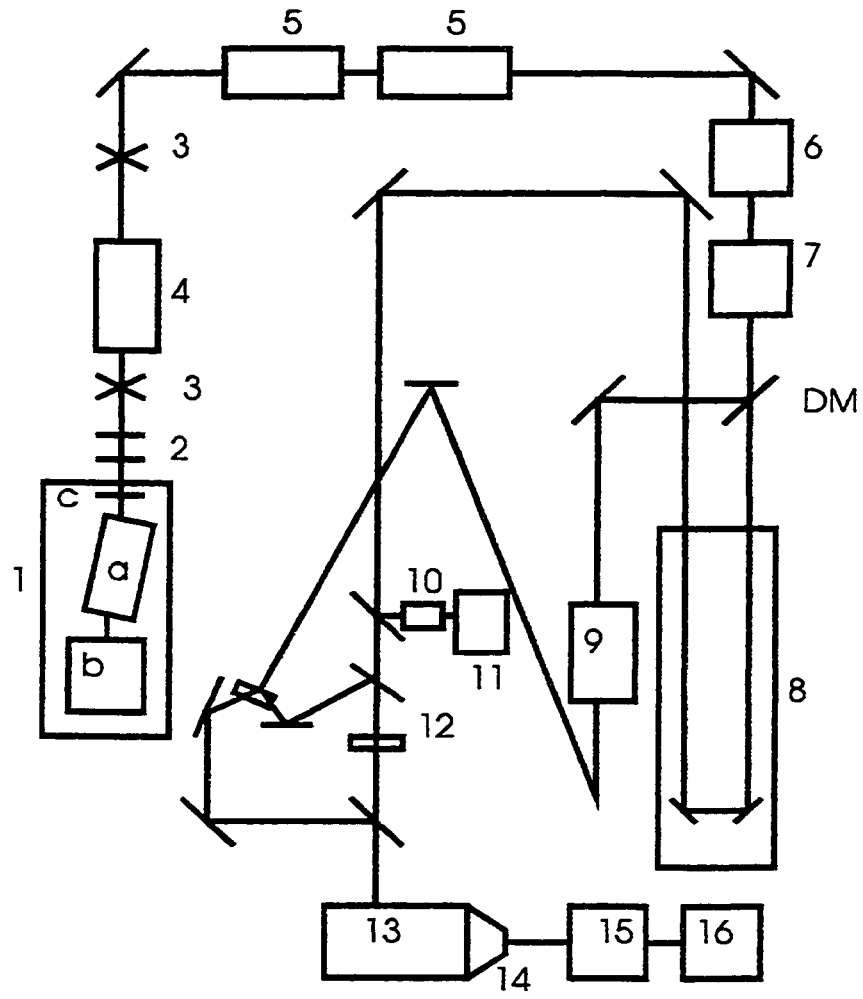

Figure 2.3. Schematic representation of the picosecond flash photolysis apparatus

1. Laser: a) head;
   b) mode locking cell
   c) mirror
2. Beam expander
3. Glan-air polarizers
4. Pulse selector
5. Amplifier
6. Second harmonic crystal
7. Third harmonic crystal
8. Delay ramp
9. Continuum cell
10. Energy Detector
11. Energy Meter
12. Sample cell
13. Double monochromator
14. Photodiode array detector
15. Multichannel analyzer
16. Computer

DM. Dichroic mirror

CHAPTER THREE: THE PHOTOCHEMISTRY OF $Cr(CNPh)_6$

3.1 Introduction

3.1.1 Bonding and Molecular Orbital Description

The structure of $Cr(CNPh)_6$ (CNPh = phenylisocyanide) has octahedral local symmetry at the metal centre. The phenyl rings are oriented to minimize steric interactions, in such a way that the plane of each adjacent phenyl ring is orthogonal to the others. This gives rise to approximate T_h symmetry. This symmetry is further broken by a uniform, small Cr-C-N bend ($\cong 7°$), reducing the complex to S_6 symmetry.[78]

The isocyanide group of a ligand CN-R is isoelectronic to carbon monoxide. The bonding of isocyanides to transition metals is entirely analogous to the coordination of CO. The M-CNR bond involves a strong σ bond with significant π back-bonding from the metal centred d(π) orbitals into empty π^* orbitals localized on the ligand.[70] Compared to the carbonyl ligand, isocyanides are better σ-donors but poorer π-acceptors.[79]

When the organic R group is aryl, there are two ligand π^* orbitals that can interact with metal d(π) orbitals.[70,78] One of these lies in the plane of the ring and has been labelled

π_h*. The second, labelled π_v* lies out of the plane and is in resonance with the π system of the aryl ring. Both π_h* and π_v* orbitals can act as acceptor orbitals in a metal-to-ligand charge transfer (MLCT) transition. However, the π_v* orbital is lower in energy and can stabilize a MLCT state through resonance with the aryl ring.

π_h* π_v*

Figure 3.1 The π* orbitals of PhNC. Only one of the degenerate π_v* orbitals is shown.

The molecular orbitals of $Cr(CNPh)_6$ are analogous to those for $Cr(CO)_6$.[80] However, unlike the carbonyl ligand, the π and π* orbitals are each split into two sets (in plane and out of plane) in PhNC. A molecular orbital diagram for $Cr(CNPh)_6$ appears in Figure 3.2. The orbital diagram shows the approximate ordering of molecular orbitals. The highest occupied molecular orbital (HOMO) is $t_g(\pi)$, and is metal centred. The lowest unoccupied orbitals (LUMO's) are the $t_u(\pi_v^*)$ and $t_g(\pi_v^*)$ ligand centred orbitals. The relative ordering of the next three orbitals (i.e. $e_g(\sigma^*)$, $t_u(\pi_h^*)$, and $t_g(\pi_h^*)$) is unclear. The absorption spectrum in given in Figure 3.3.

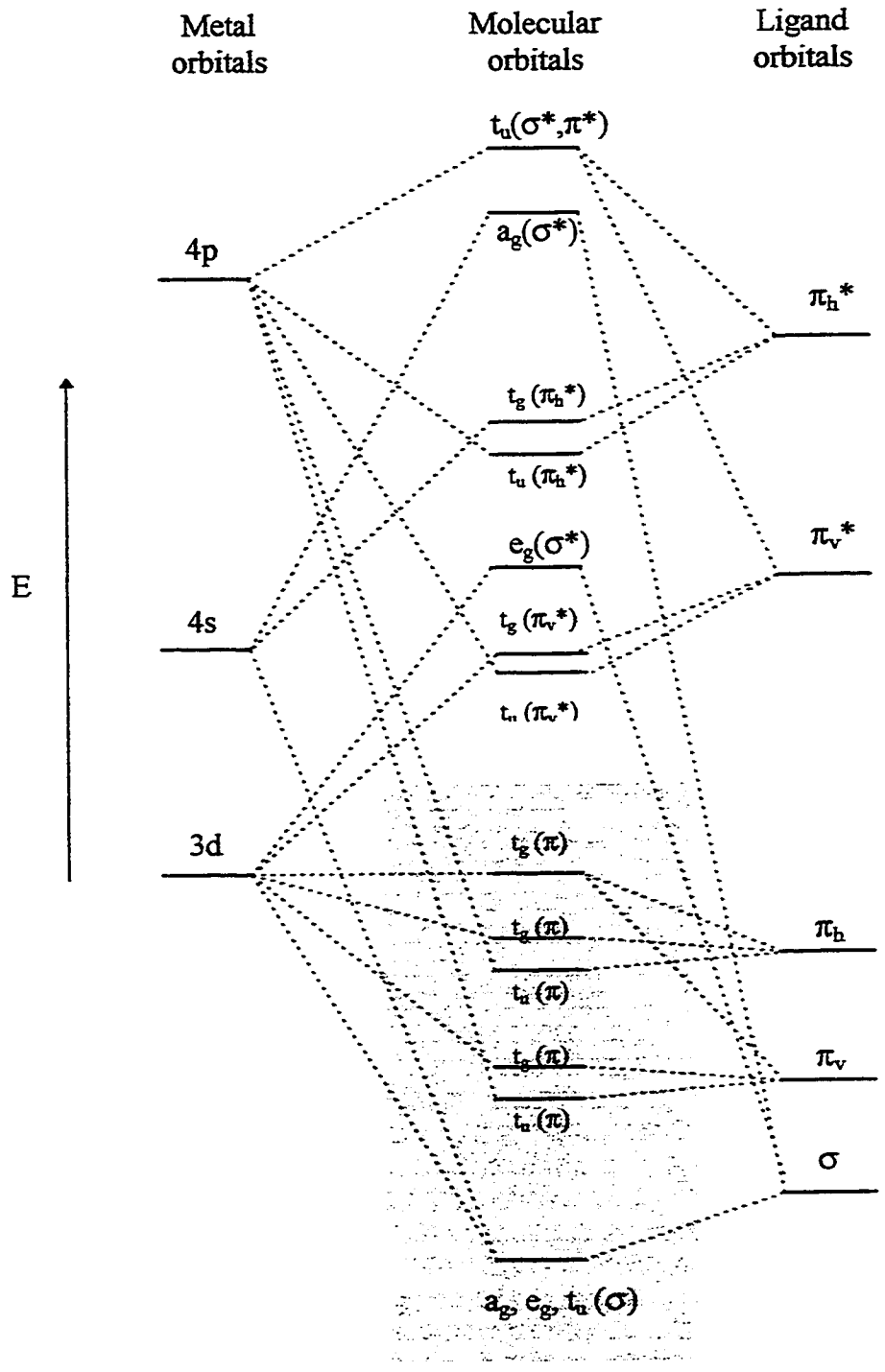

Figure 3.2 Molecular orbital diagram for $Cr(CNPh)_6$, restrained to T_h symmetry. Note that the relative orbital positions are approximate. The shaded region represents filled orbitals.

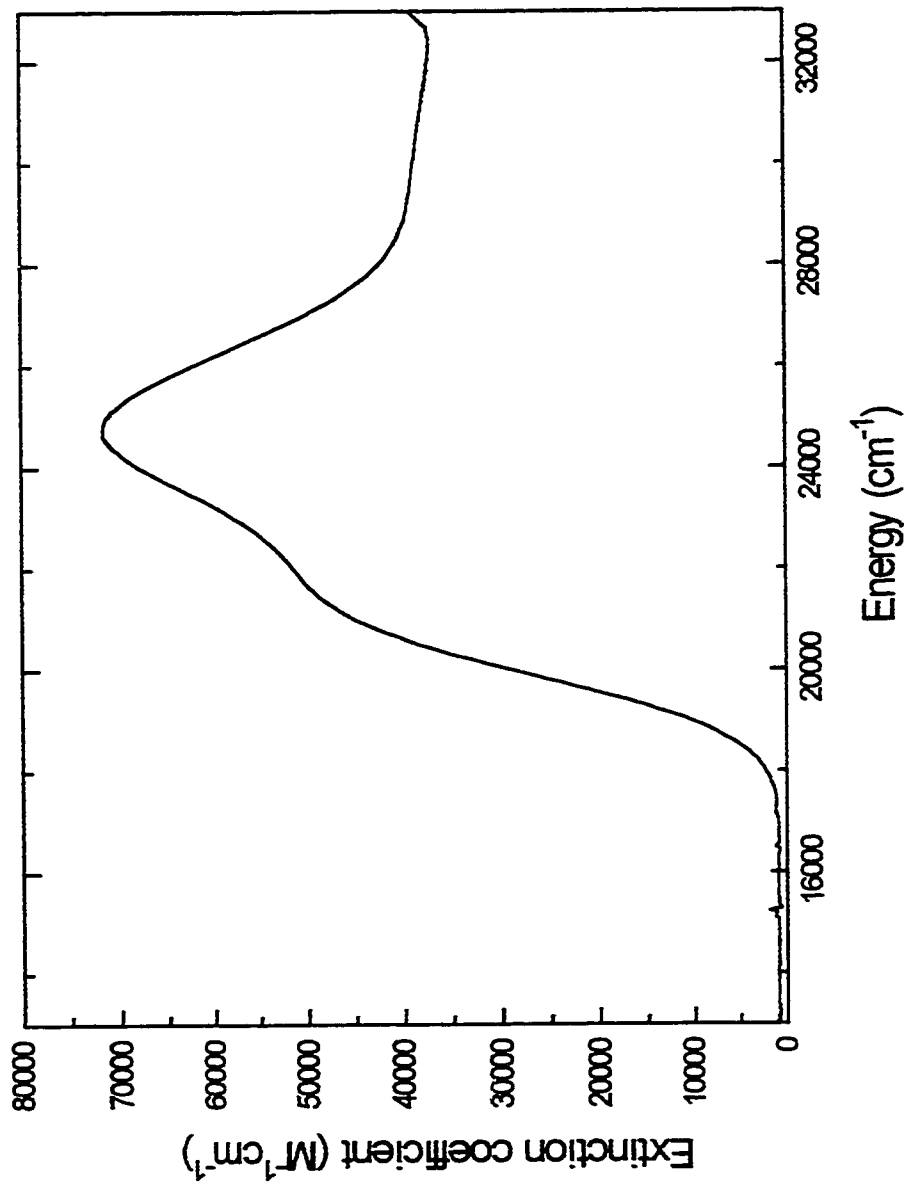

Figure 3.3 Absorption spectrum of $Cr(CNPh)_6$ in benzene.

The lowest energy excited states in $Cr(CNPh)_6$ are MLCT states.[70] In T_h symmetry, these states are $(t_g)^5(t_g)^1$ and $(t_g)^5(t_u)^1$. The symmetry allowed transition $(t_g)^6 \rightarrow (t_g)^5(t_u)^1$ gives four excited states: $2T_u + E_u + A_u$.[57,78] In the actual S_6 molecular symmetry, the T_u states must split into other A_u and E_u states.[57] Thus, the broad MLCT absorption in $Cr(CNPh)_6$ is composed of a set of electronic transitions. The transition $(t_g)^6 \rightarrow (t_g)^5(t_g)^1$ has been ignored in the literature because it is formally symmetry forbidden, being a $g \rightarrow g$ transition. It is well known that this symmetry rule can be relaxed provided there is an asymmetrical vibration or ground state distortion that destroys the centre of inversion. The MLCT absorption band must include these additional $(t_g)^6 \rightarrow (t_g)^5(t_g)^1$ transitions, giving rise to $2T_g + E_g + A_g$ excited states in T_h symmetry. However, these transitions are expected to be less intense compared to the $(t_g)^6 \rightarrow (t_g)^5(t_u)^1$ transitions, with molar extinction coefficients of at least a few hundred.

Another consideration is the location of the $d(\pi) \rightarrow \pi_h^*$ transitions. Based on comparisons with $Mn(CNMe)_6^+$, the $t_g \rightarrow t_u\ \pi_h^*$ transitions of $Cr(CNPh)_6$ are predicted to be above 31800 cm^{-1}.[78] For the experiments presented here, the wavelength region above 32000 cm^{-1} is of minor importance because the highest energy wavelength used is 313-nm (31950 cm^{-1}). Ligand field states likely appear at energies above 25000 cm^{-1}.[78] The d-d transitions should produce relatively weak bands compared to the intense MLCT

absorptions. All of the experiments here involve the MLCT absorptions arising from $d(\pi) \rightarrow \pi_v^*$ transitions.

3.1.2 Photochemistry and Photophysics

Photosubstitution and photoinduced electron transfer have been observed in $Cr(CNPh)_6$.[61,78] In neat pyridine, $Cr(CNPh)_6$ undergoes photosubstitution:

$$Cr(CNPh)_6 \xrightarrow{436\ nm,\ pyridine} Cr(CNPh)_5py + PhNC$$

The ligands PhNC and 2,6-diisopropylphenylisocyanide (CNIph) were used in order to compare the substitutional reactivity of $Cr(CNAr)_6$ complexes on the basis of steric effects.[61] In both $Cr(CNPh)_6$ and $Cr(CNIph)_6$, the quantum yield for photosubstitution in pyridine was 0.23 (at 436 nm). This similarity in quantum yields for complexes with significantly different steric environments around the metal centre led to the conclusion that the substitution proceeds via a dissociative mechanism.

A study of the wavelength dependence of the photosubstitution of $Cr(CNPh)_6$ in pyridine showed a decrease in ϕ_{sub} with increasing irradiation wavelength.[57] This is typical of

photodissociations where greater excitation energy corresponds to a greater probability of cage escape.

Only one time-resolved study has previously been reported on $Cr(CNPh)_6$, using THF as the solvent.[60] Using 1 ps pulses at 300 nm, it was observed that the substitution product $Cr(CNPh)_5(THF)$ was formed within the pulse. Thus, ligand dissociation occurs in less than 1 ps. This places the photodissociation in the ultrafast regime observed for $M(CO)_6$ (M = Cr, Mo, W).

An extremely weak emission from $Cr(CNPh)_6$ with $\tau < 10$ ns has been observed.[78] The emission maximum is also subject to a significant Stokes shift. These observations are suggestive of weakly bound excited states (i.e. the system does not thermally relax into a well defined potential well from which emission can occur). This agrees with the ultrafast nature of the ligand dissociation.

Photoinduced electron transfer has been observed in $Cr(CNAr)_6$ complexes.[61,78] The early model for this electron tranfer reactivity is based on electron transfer directly from the MLCT excited state. In $Cr(CNIph)_6$, irradiation at 436 nm in degassed chloroform gives the one electron oxidation product $Cr(CNIph)_6^+$ with a quantum yield of 0.19. The quantum yield rises to 0.70 in air-saturated chloroform. The interpretation is that oxygen

acts to enhance the cage escape of the electron transfer products (i.e. radicals) that are formed from excited state electron transfer to the electron acceptor solvent. In $Cr(CNPh)_6$, a Cr(II) product is formed on irradiation in chloroform. This will be discussed further in a later section.

3.2 Photosubstitution

3.2.1 Nucleophile Dependence

In order to confirm the dissociative mechanism of photosubstitution in $Cr(CNPh)_6$, the dependence of ϕ_{sub} on nucleophile was studied. Quantum yields were determined in benzene containing a low concentration of nucleophile. This avoids the complications of solvent effects, which can account for large variations in substitution quantum yields. The nucleophiles pyridine and triphenylphosphine (PPh_3) were used. Tetrahydrofuran was chosen as a third nucleophile but the product $Cr(CNPh)_5(THF)$ undergoes thermal back substitution to give $Cr(CNPh)_6$ and ϕ_{sub} could not be measured.

Table 3.1 gives the quantum yields for photosubstitution in benzene containing 0.1 M of nucleophile, at various wavelengths. Within experimental error, there is no difference in ϕ_{sub} with pyridine or PPh_3. The insensitivity to entering group indicates a dissociative mechanism. The wavelength dependence will be discussed in a later section.

Table 3.1 Nucleophile Dependence of Photosubstitution Quantum Yields for $Cr(CNPh)_6$ in Benzene		
Wavelength (nm)	0.1 M pyridine	0.1 M PPh_3
365	0.42 ± 0.01	0.42 ± 0.01
436	0.38 ± 0.01	0.39 ± 0.01
514	0.29 ± 0.01	0.28 ± 0.01

3.2.2 Nucleophile Concentration Dependence

The dependence of ϕ_{sub} on nucleophile concentration was determined. Table 3.2 gives the dependence of ϕ_{sub} on pyridine concentration at 538 nm. The concentration of $Cr(CNPh)_6$ was between 2.2×10^{-4} and 3.2×10^{-4} for these experiments. Thus, the

Table 3.2 Dependence of ϕ_{sub} on Pyridine Concentration in benzene	
Pyridine concentration (M)	ϕ_{sub}
1.0×10^{-2}	0.28 ± 0.01
2.0×10^{-3}	0.29 ± 0.01
4.0×10^{-4}	0.28 ± 0.01

pyridine concentration was brought to within a factor of two of [$Cr(CNPh)_6$]. Quantum yields were determined from the first 10% conversion so that pseudo first order conditions were maintained.

3.3 Electron Transfer

3.3.1 Background

The previous study on photoinduced electron transfer in $Cr(CNPh)_6$ used the solvent chloroform as the electron acceptor.[61,78] In the case of $Cr(CNPh)_6$, formation of a Cr(II) species was found. IR analysis of the product mixture showed the presence of free PhNC. It was proposed that $Cr(CNPh)_6^{2+}$ is initially produced photochemically and that this undergoes a reaction with the Cl^- produced in the electron transfer reaction:

$$Cr(CNPh)_6^{2+} + Cl^- \leftrightharpoons Cr(CNPh)_5Cl^+ + PhNC$$

This study assumed that the initial electron transfer occurred directly from the MLCT excited state. The chlorinated solvent acted as an efficient electron acceptor. This experiment did not allow for any estimate of the lifetime of the reactive state. Since the electron acceptor was always in a state of encounter with the complex, it is impossible to

estimate the lifetime of the reactive state using the acceptor concentration and the rate of diffusion in that solvent.

In order to avoid the possible complications that arise due to Cl radical formation and to estimate the lifetime of the reactive state, it was chosen to study the electron transfer using a dilute concentration of an organic electron acceptor in an inert organic solvent. A stable reduced organic acceptor avoids problems due to Cl radical attack on the metal centre. The second advantage is that the dependence of electron transfer efficiency on acceptor concentration can yield a crude estimate of the lifetime of the reactive species.

The organic electron acceptor must be chosen carefully. If the reduction potential of the acceptor is much larger than the oxidation potential of the metal complex, thermal electron transfer from the ground state will occur and the light induced process cannot be studied easily. Conversely, if the reduction potential of the acceptor is too low, back electron transfer will occur. In either case, a quantum yield for electron transfer would be difficult to quantify.

The potential for the Cr^{+}/Cr^{0} couple is $Cr(CNPh)_6$ is -0.53 V in CH_3CN relative to Ag/AgCl.[81] The acceptor benzoquinone (BQ) was chosen because it has a similar reduction potential (-0.585 V vs. Ag/AgCl).[82] By having similar E^{0}'s, thermal electron

transfer from the ground state and back electron transfer among the photoproducts are hindered due to kinetic overpotential.

3.3.2 Electron Transfer to Benzoquinone

When $Cr(CNPh)_6$ is irradiated in benzene in the presence of BQ, precipitates are formed. This is evidence for an electron transfer reaction that forms ionic products which are insoluble in the non-polar solvent. The product(s) are likely $\{Cr^{II}L_6^{2+}, BQ^{-}\}$or $\{Cr^{III}L_6^{3+}, BQ^{-}\}$ salts, where L is either PhNC or BQ. In order to hinder precipitate formation, a solvent mixture of phenylisocyanide/benzene (10% by volume) was used. By using phenylisocyanide as the co-solvent, substitution processes do not complicate the data analysis. Figure 3.4 shows the spectral changes observed for this reaction.

Electron transfer quantum yields (ϕ_{et}) were obtained by monitoring the loss in $Cr(CNPh)_6$ absorption. Figure 3.5 shows the variation of ϕ_{et} with BQ concentration under 436-nm irradiation. It can be seen that a limiting value of ϕ_{et} is reached at BQ concentrations of 2-3 mM.

3.3.3 Electron Transfer to bis(t-butyl) pyromellitic diimide

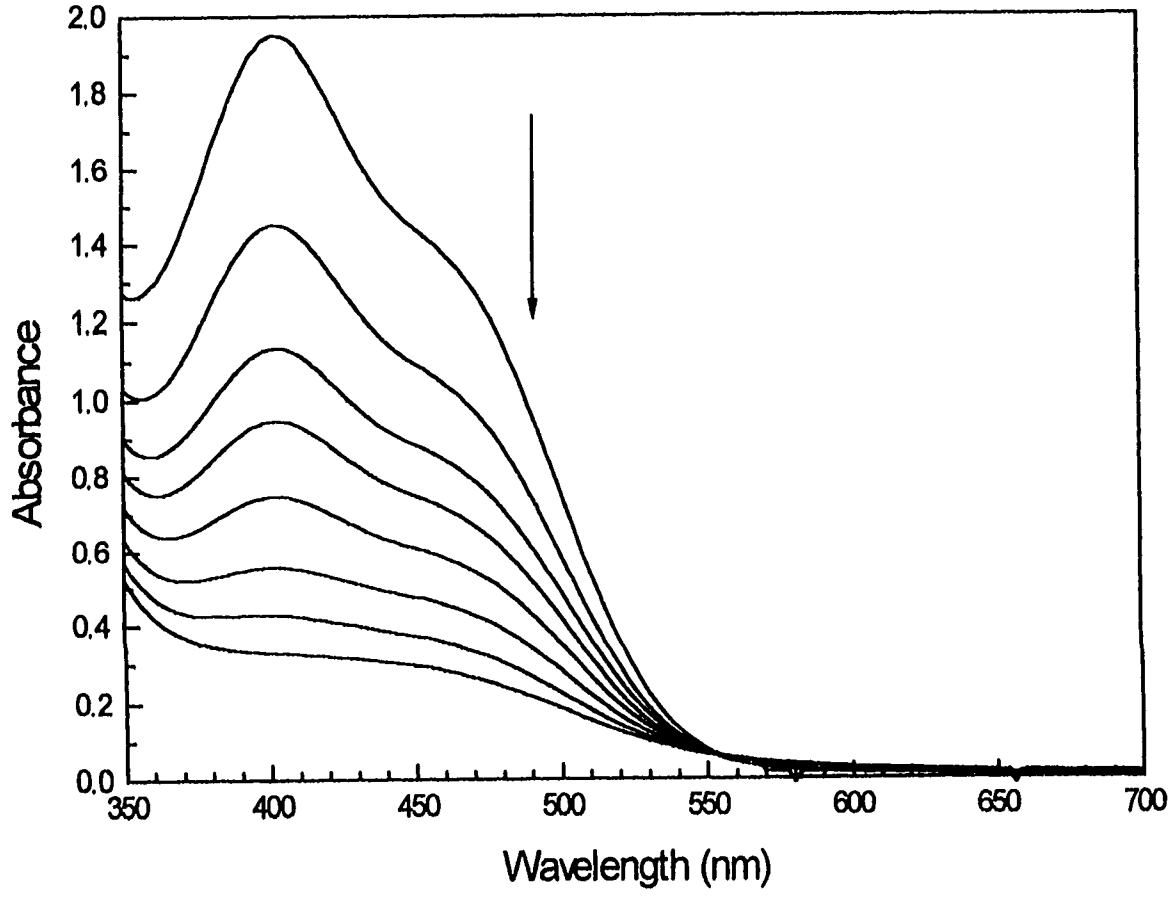

Figure 3.4 The visible spectral changes for the photoinduced electron transfer reaction of $Cr(CNPh)_6$ with benzoquinone. The final spectrum is similar to that of the remaining benzoquinone in solution.

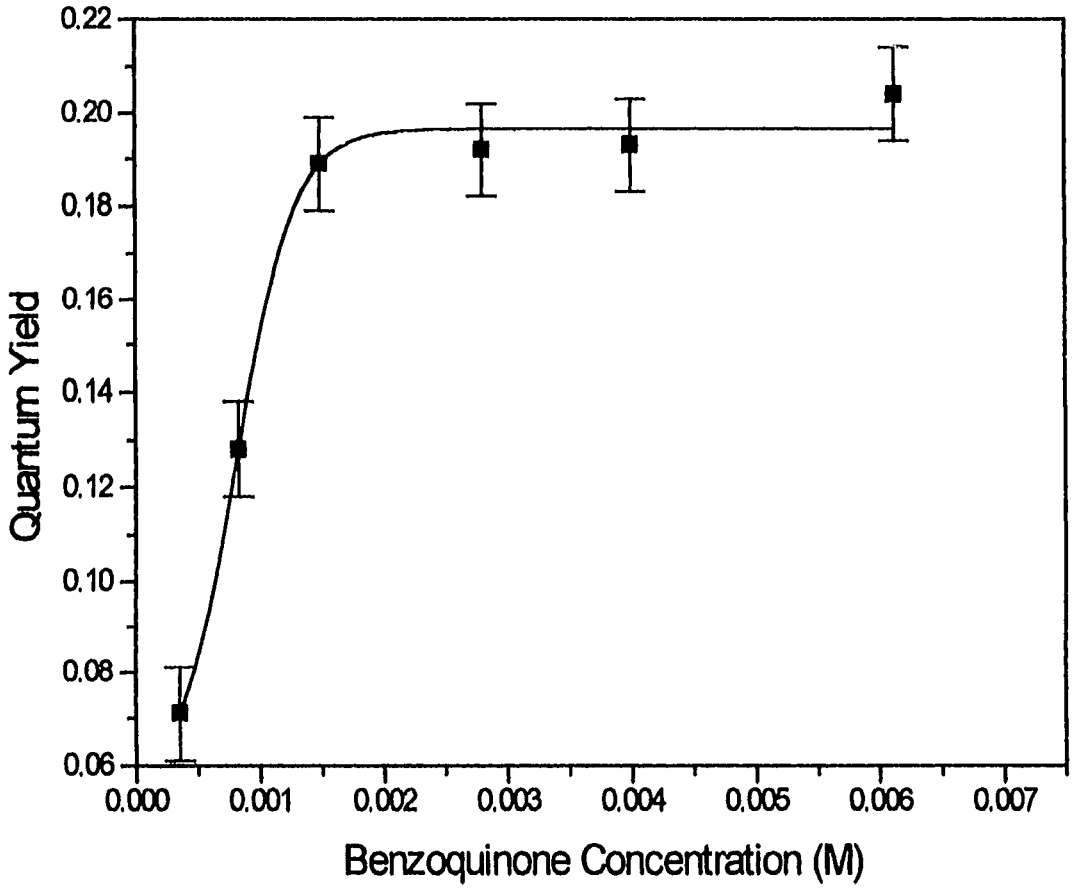

Figure 3.5 Benzoquinone concentration dependence of quantum yields for the decomposition of $Cr(CNPh)_6$ in 10% phenylisocyanide/benzene at 436 nm. Error bars represent standard deviation.

When the organic electron acceptor has a reduction potential that is significantly lower than that of the Cr^{+}/Cr^{0} couple in $Cr(CNPh)_6$, reversible electron transfer will occur. This is the case for bis(t-butyl) pyromellitic diimide (TBP).

When a benzene solution of $Cr(CNPh)_6$ and TBP is irradiated with intense visible light, a red-brown amorphous precipitate forms. On shaking, the precipitate redissolves in the dark and the newly formed visible absorptions recover to the original absorption spectrum of $Cr(CNPh)_6$ over a few minutes (Figure 3.6). Below critical $Cr(CNPh)_6$ concentrations of about 10^{-5} M, precipitates are not observed - although the final absorption recovery step is still seen.

The rate law for the recovery of the absorption spectrum was determined in order to gain insight into the nature of this reaction. Figure 3.7 shows that the spectral changes are first order in the absorbing species, which is assigned to $Cr(CNPh)_5S$ (S = solvent). Figure 3.8 shows the dependence of the pseudo first order rate constants on the concentration of PhNC. This leads to the rate law:

$$d[Cr(CNPh)_6] = k[Cr(CNPh)_5S][PhNC]$$

where $k = 36.5\ M^{-1}s^{-1}$

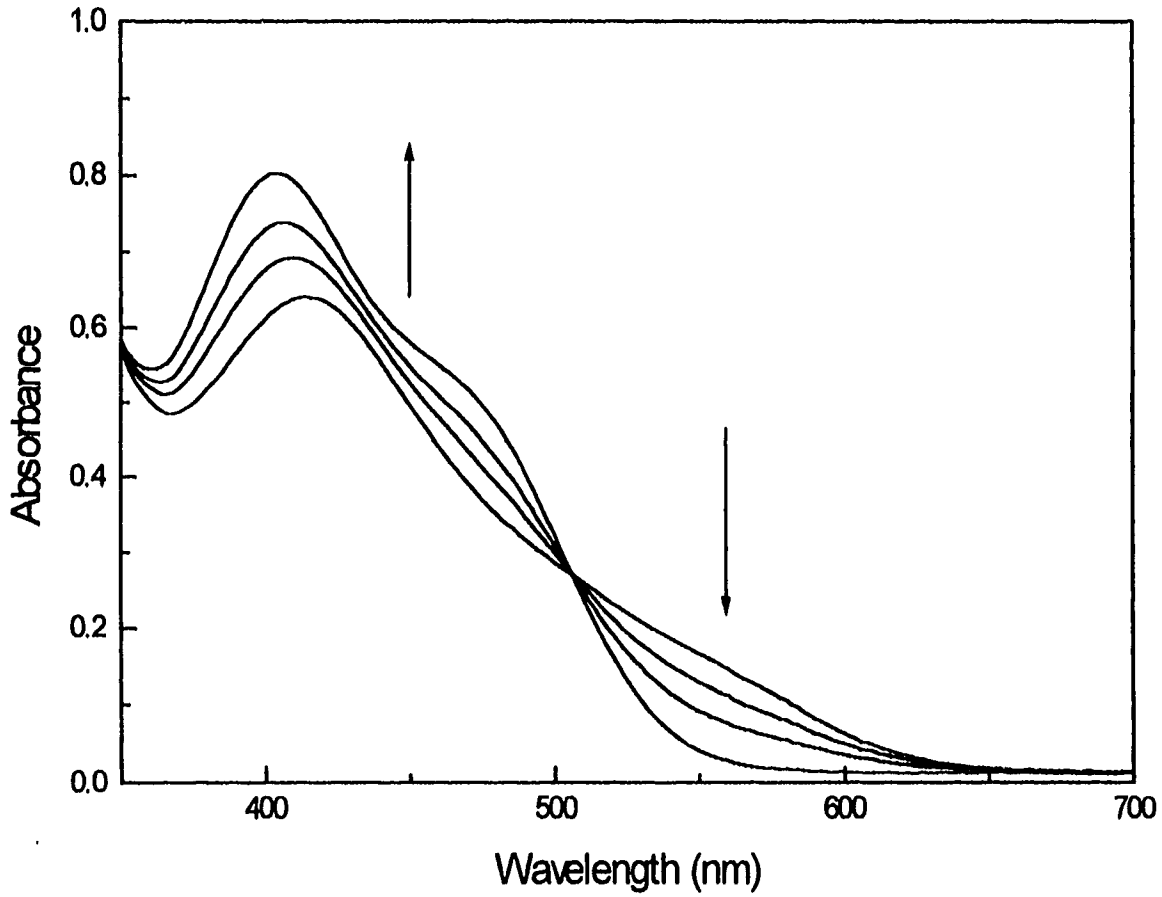

Figure 3.6 Absorbance changes for $Cr(CNPh)_5S$ + PhNC → $Cr(CNPh)_6$ in the 350 - 700 nm region following dissolution of the precipitate. Spectra were taken 0, 1, 3, and 35 minutes after dissolution. [TBP] = 5.0×10^{-3} M; [$Cr(CNPh)_6$] = 1.2×10^{-5} M.

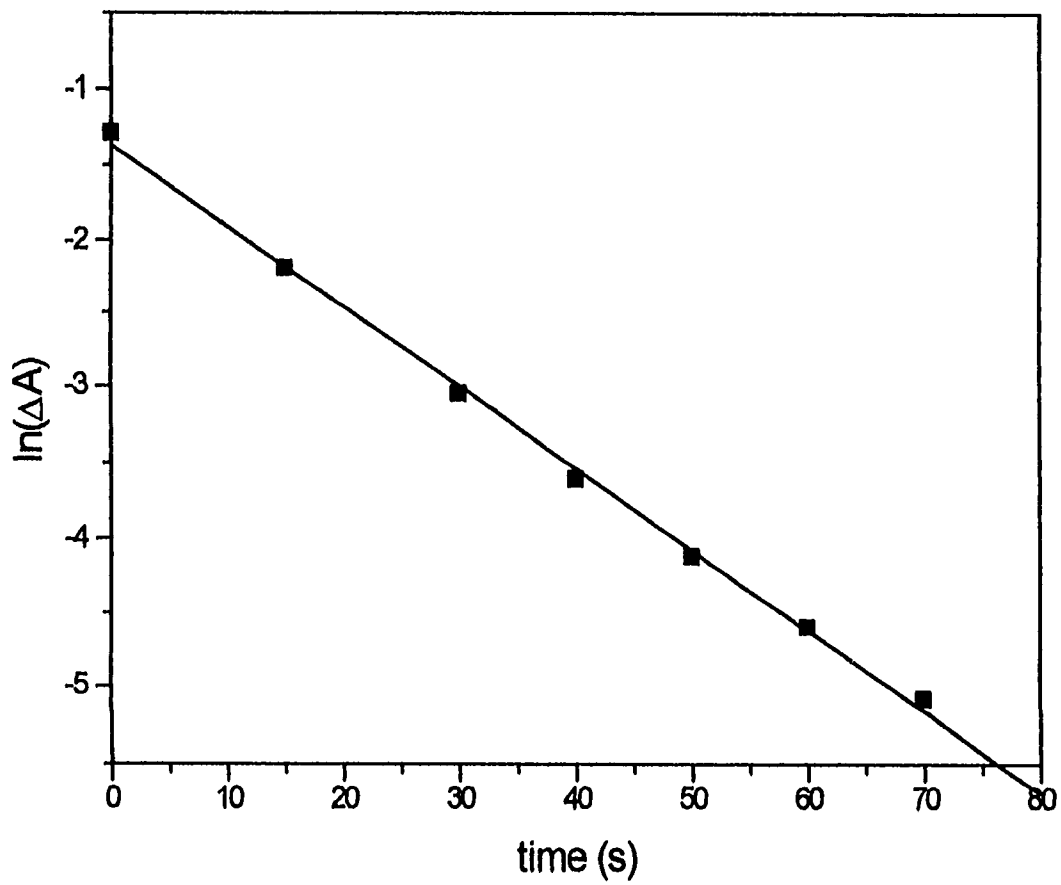

Figure 3.7 Plot of the logarithm of absorbance change at 532-nm following precipitate formation and dissolution. $[Cr(CNPh)_6]$ $=1.1 \times 10^{-4}$ M; [TBP] = 4.7×10^{-3} M; [PhNC] = 7.8×10^{-4} M. Regression output gives $k_{obs} = 0.0542\ s^{-1}$ ($r^2 = 0.99$).

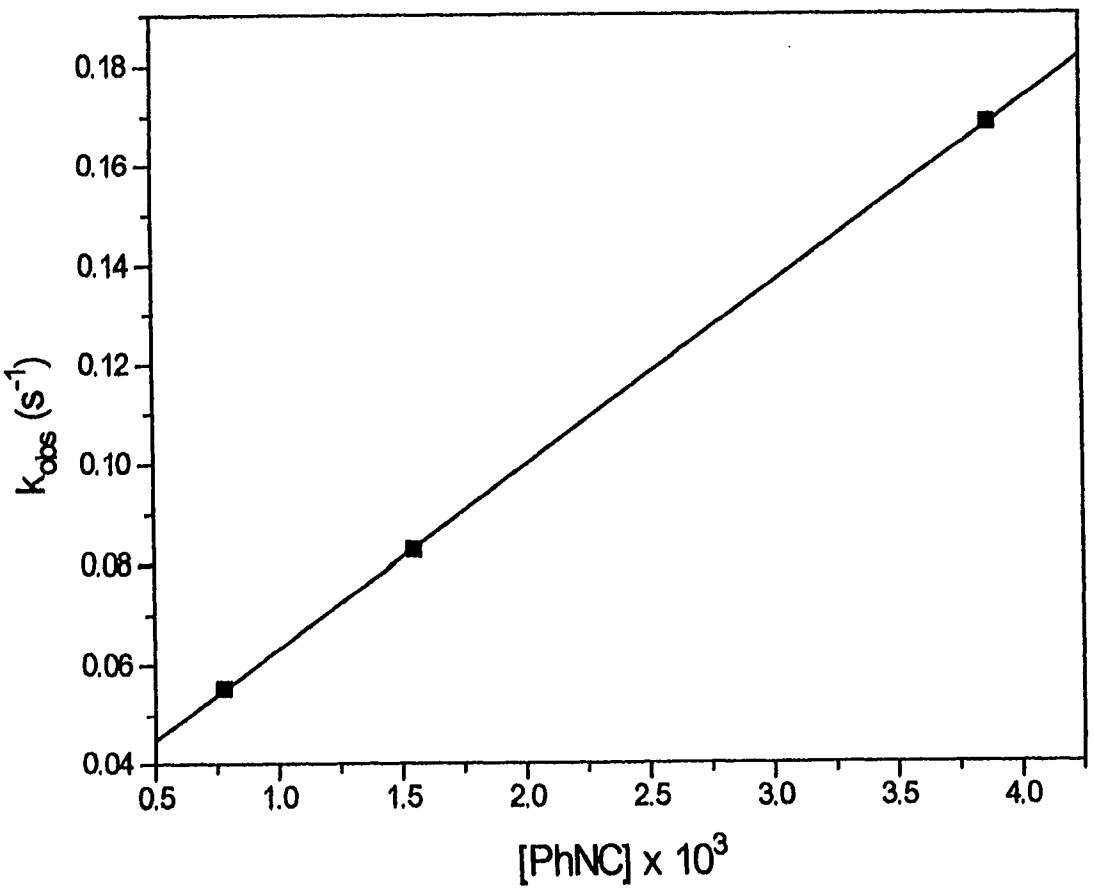

Figure 3.8 Dependence of pseudo first-order rate constants for $Cr(CNPh)_5S \rightarrow Cr(CNPh)_6$ on [PhNC]. The data provides a second order rate constant of 36.5 $M^{-1}s^{-1}$ ($r = 0.99$).

3.4 Wavelength Dependence

3.4.1 Photosubstitution Quantum Yields

The wavelength dependence of photosubstitution in $Cr(CNPh)_6$ was studied in various solvents. In benzene and neat pyridine, the quantum yields decrease with increasing wavelength (Figures 3.9 and 3.10). The differences in quantum yield between these two solvents are relatively small, and are attributed to solvent effects. The overall trends in ϕ_{sub} with wavelength are similar.

ϕ_{sub} in toluene is also large and independent of irradiation wavelength (Table 3.3). When $Cr(CNPh)_6$ is irradiated in neat toluene with no added nucleophile, the absorption spectra (Figure 3.11) show that a discrete product is formed (i.e. slow photodecomposition does not occur). For this reason, the quantum yields in toluene are discounted and cannot be compared to quantum yields in other non-coordinating solvents. This photochemical reaction is unusual and appears to be specific for toluene. This reactivity with solvent is not observed in benzene.

In dimethylsulfoxide (DMSO), quantum yields are also essentially independent of irradiation wavelength (Table 3.3). The wavelength independent, unit quantum yield in DMSO indicates either a different mechanism for photosubstitution (e.g. electron transfer

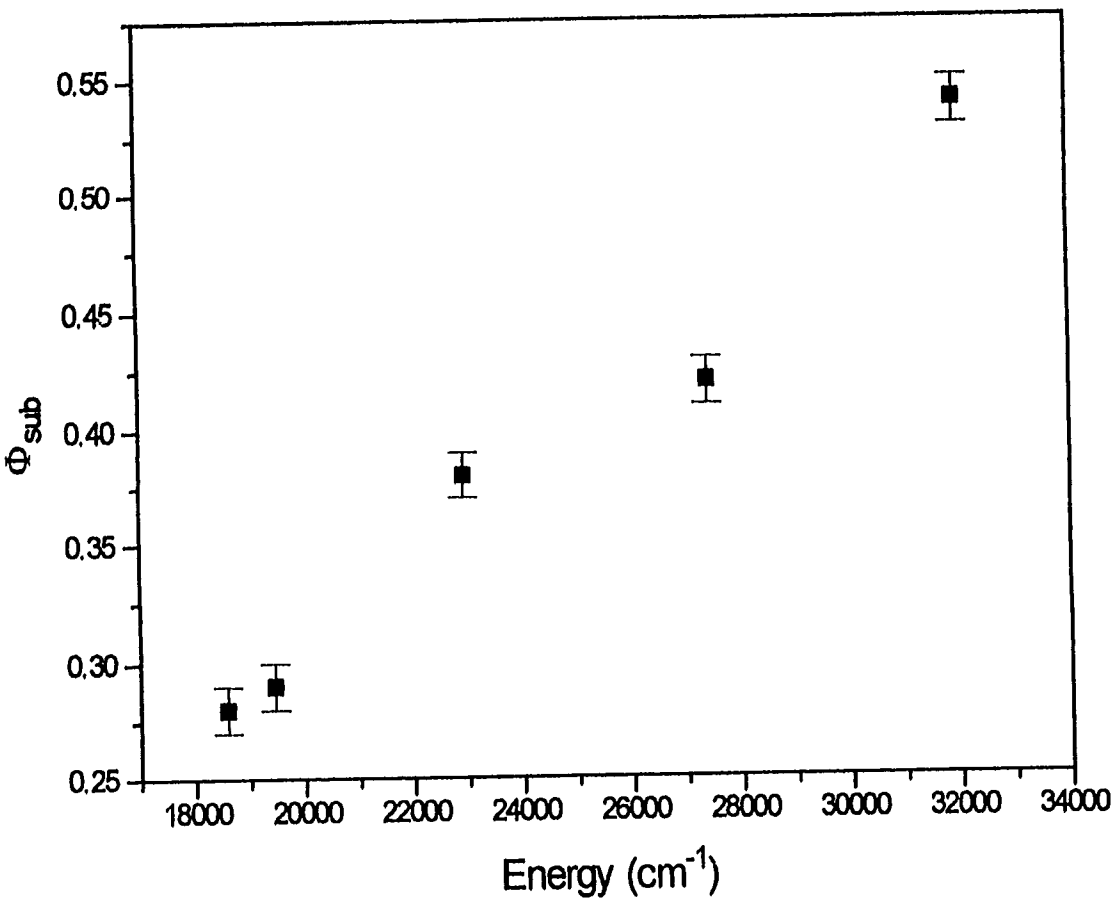

Figure 3.9 Excitation energy dependence of photosubstitution quantum yields ϕ_{sub} for $Cr(CNPh)_6$ in benzene (0.1 M pyridine). Error bars represent standard deviation for each data point. The linear regression output for these points is: $\phi = (1.89 \times 10^{-5})(E) - 0.0739$, where energy E is in cm^{-1}; $r^2 = 0.98$.

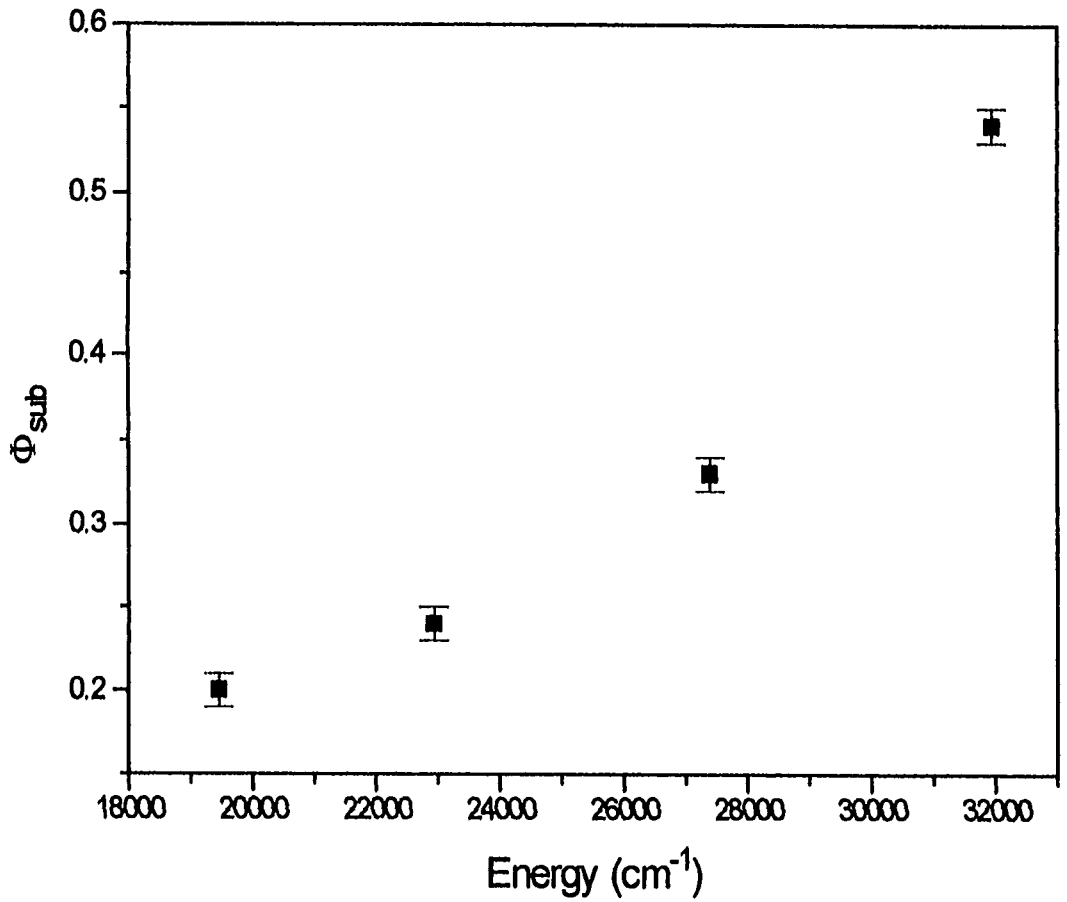

Figure 3.10 Excitation energy dependence of photosubstitution quantum yields ϕ_{sub} for $Cr(CNPh)_6$ in neat pyridine. Error bars represent standard deviation for each data point. The linear regression output for these points is: $\phi = (2.69 \times 10^{-5})(E) - 0.355$, where energy E is in cm^{-1}; $r^2 = 0.92$.

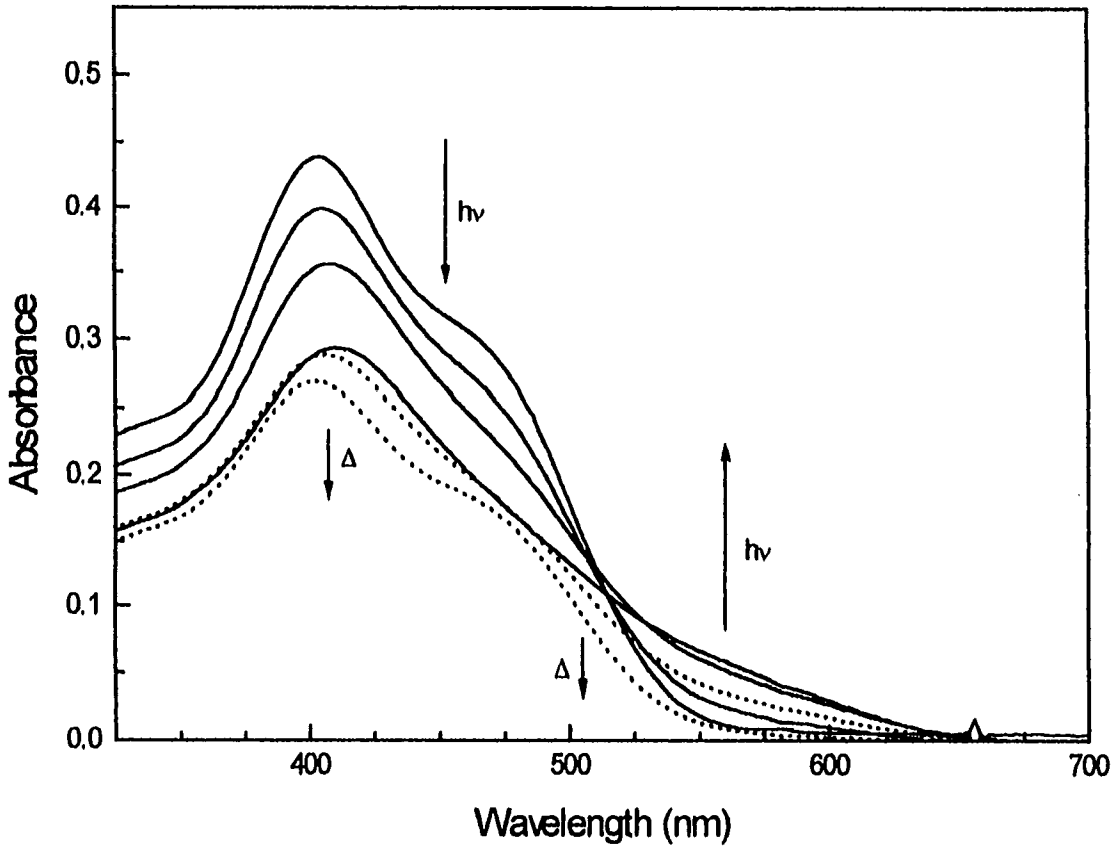

Figure 3.11 UV-visible absorption changes for $Cr(CNPh)_6$ irradiated at 436 nm in toluene. The solid lines are spectra taken immediately after 0, 5, 15, and 35 seconds of irradiation. Dashed lines are spectra taken following dark periods of 4 and 17 minutes. The arrows indicate the direction of photochemical (hν) or thermal (Δ) changes.

mediated) or exceptional solvation of the primary products. Picosecond absorption spectra in DMSO show similar signals to those in other solvents (see Appendix C), which suggests similar primary processes. Chains of events which act to increase the overall substitution efficiency may take place after 10 ns.

Table 3.3 Wavelength Dependence of Photosubstitution Quantum Yields in Various Solvents*

Wavelength (nm)	Benzene (0.1 M pyridine)	Pyridine	DMSO	Toluene (0.01 M) pyridine
313	0.54	0.54	1.01	0.82
365	0.42	0.33	1.04	0.81
436	0.38	0.24	1.01	0.83
514	0.29	0.20	-	-
532	0.28	-	1.01	0.81

* All values are $\pm$ 0.01.

3.4.2 Photoinduced Electron Transfer Quantum Yields

The wavelength dependence for the photoinduced electron transfer reaction between $Cr(CNPh)_6$ and BQ is shown in Figure 3.12. The quantum yield increases from 0.07 at 365 nm to a limit of 0.29 between 514 and 532 nm. The quantum yield at 313 nm was

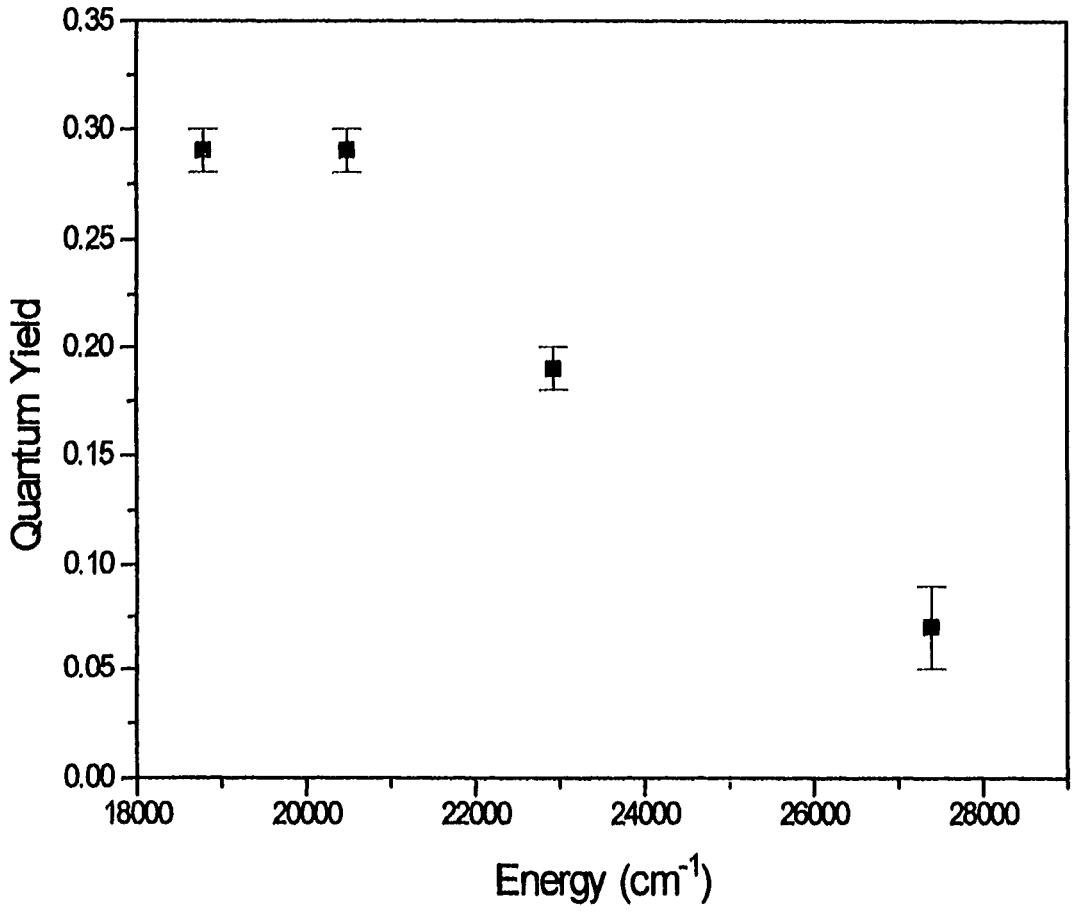

Figure 3.12 Excitation energy dependence of photoinduced electron transfer quantum yields between $Cr(CNPh)_6$ and benzoquinone. Error bars represent standard deviation for each data point.

not measured because of the large BQ absorption at this wavelength, which interferes with light absorption by $Cr(CNPh)_6$.

3.4.3 Interpretation of Steady State Wavelength Dependences

The steady state quantum yields for both substitution and electron transfer are wavelength dependent. In benzene and pyridine, ϕ_{sub} decreases monotonously with decreasing excitation energy. This is a typical pattern in photodissociation reactions of metal complexes, where greater excess excitation energy translates into more efficient cage escape.

The wavelength dependence of electron transfer is significantly different from the dependence for substitution. The interpretation of a quantum yield that *increases with decreasing excitation energy* is that there is a low energy state that is responsible for the electron transfer reaction, and that excitation at higher energies does not lead to efficient population of this state.

3.4.4 Nanosecond Flash Kinetics

The photochemistry of $Cr(CNPh)_6$ was examined using nanosecond flash photolysis. In neat benzene $Cr(CNPh)_6$ is relatively non-reactive, although there is a small degree of permanent bleaching ($\phi \approx 0.05$ at 436-nm). This makes benzene an appropriate medium in which to monitor the fate of photoproducts over time. $Cr(CNPh)_6$ in benzene was excited with both 355- and 532-nm flashes. There are two absorption features observed in the time resolved spectra of $Cr(CNPh)_6$: 1. bleach signal; 2. excited state absorption (ESA). Here, an ESA is operationally defined as an absorption with a greater intensity than the ground state absorption at that wavelength. Either an excited state or initial photoproducts can be responsible for an ESA. The kinetics of bleach recovery (monitored at 400-nm) and ESA decay (monitored at 630-nm) were measured.

For 355-nm flashes, both the bleach recovery and ESA decay are simple monoexponentials, each having a lifetime $\tau = 23$ μs (Figures 3.13, 3.14). These single exponential fits must correspond to the first order reaction

$$Cr(CNPh)_5S + PhNC \xrightarrow{\tau = 23\mu s} Cr(CNPh)_6$$

The ESA signal observed in the long wavelength region (630-nm) is therefore assigned to $Cr(CNPh)_5S$.

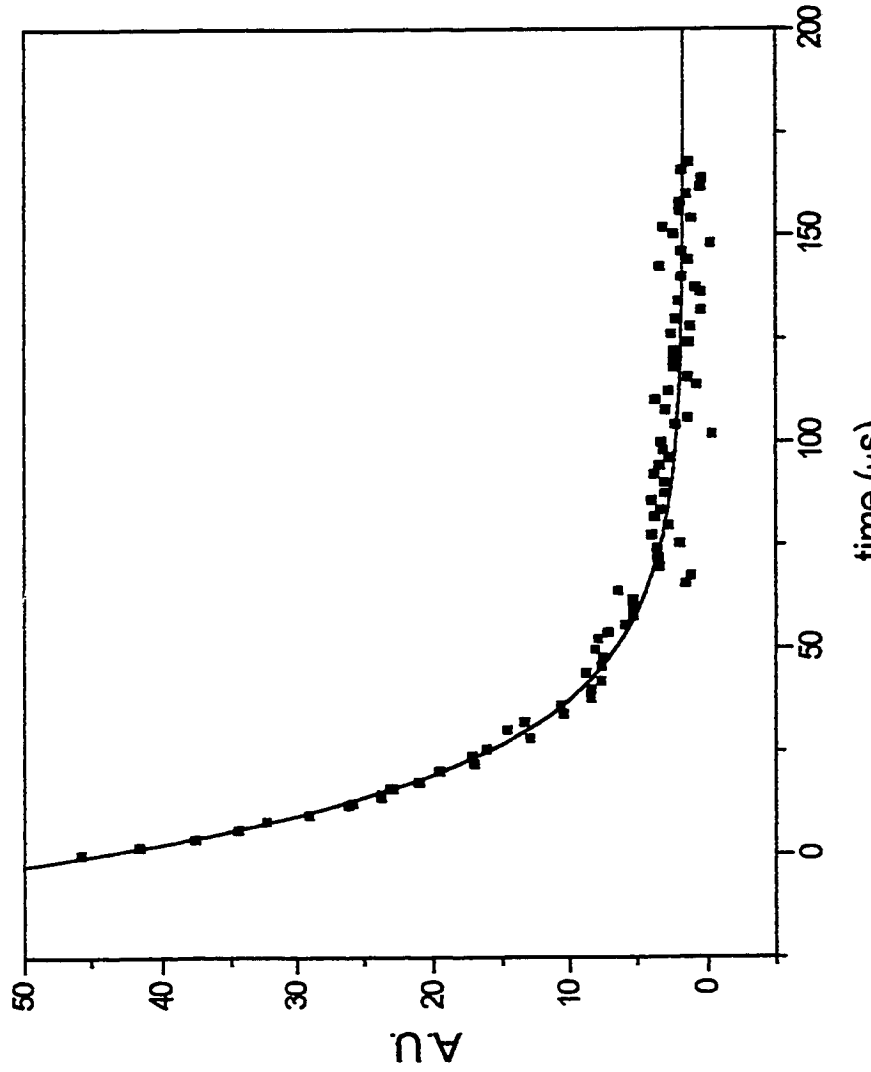

Figure 3.13 Decay of 630 nm signal for 355 nm flash photolysis with the exponential function $y = 1.66 + 42.71*\exp(-x/23)$ overlaid.

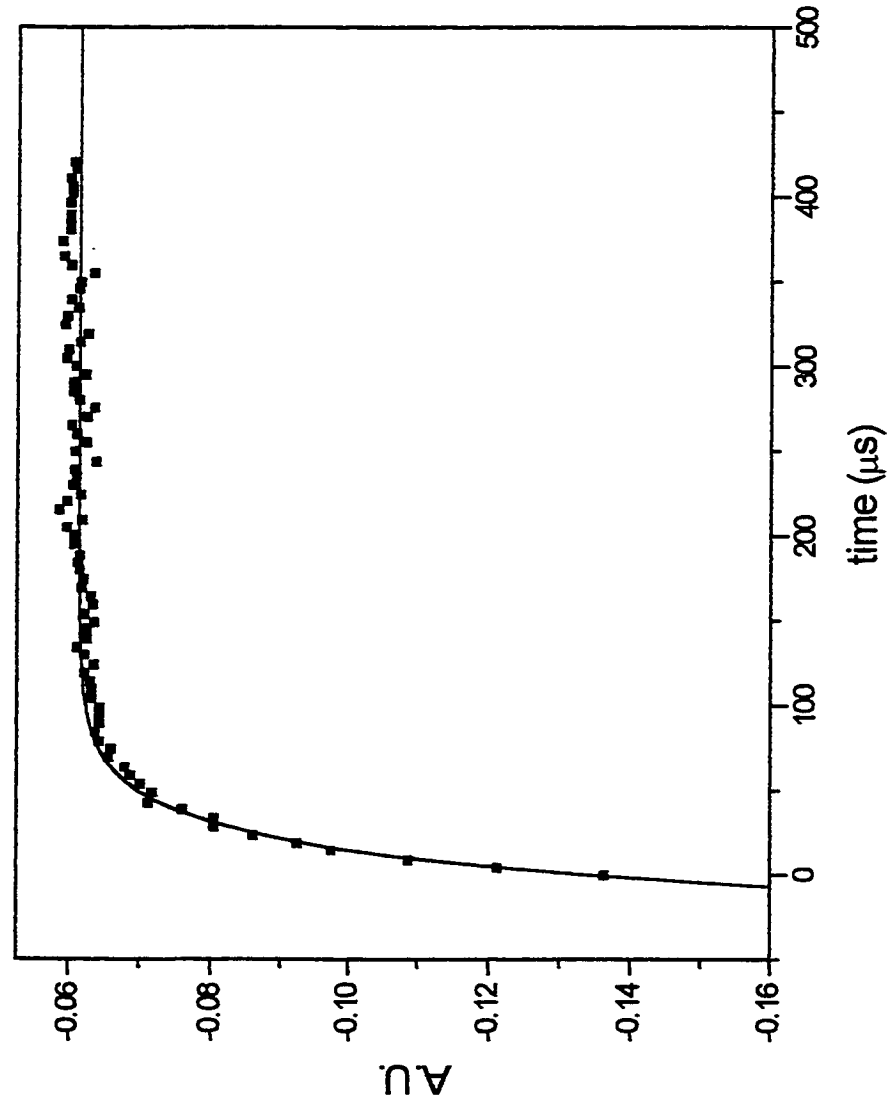

Figure 3.14 Bleach recovery at 400 nm for 355 nm flash photolysis with the exponential function y = -0.0614 - 0.0726*exp(-x/23) overlaid.

For 532-nm flashes, the $Cr(CNPh)_5S$ signal at 630-nm also decays as a single exponential, but with a slightly different lifetime of $\tau = 29$ μs. However, the data for this experiment are noisy compared to the other nanosecond kinetic data. When a $\tau = 23$ μs exponential is fit to the data (Figure 3.15), a plot of residuals vs. time (Figure 3.16) reveals a sinusoidal pattern in the noise, indicative of an instrumental or optical artifact. None of the other residuals in the nanosecond flash results revealed similar artifacts, but showed only random noise. The original 29 μs lifetime is most likely perturbed as a result of the relatively small signal to noise ratio, and the nature of this noise.

The bleach recovery for 532-nm excitation is not a simple exponential, and it is clear from visual examination of the trace (Figure 3.17) that a fit requires two or more exponentials. Knowing that there must be a 23 μs component, the data were fitted with two additional unknown exponentials. These other components were found to have lifetimes of 12 μs and 214 μs. This fit suggests two other reactions at 532-nm that occur in addition to the charge neutral back reaction responsible for the 355-nm kinetics. Apparently, these other reactions do not significantly affect the decay of the 630 nm signal assigned to $Cr(CNPh)_5S$.

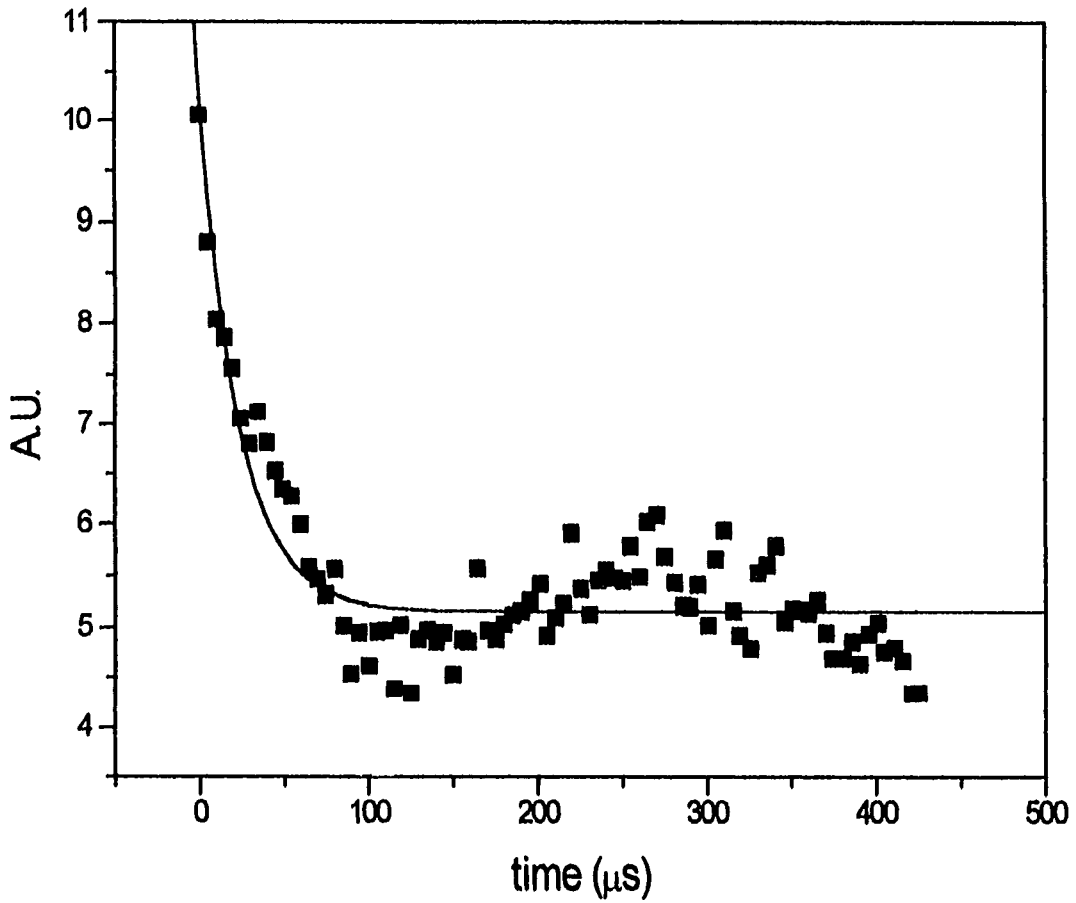

Figure 3.15 Decay of 630 nm signal for 532 nm flash photolysis with the exponential function $y = 5.16 + 5.04*\exp(-x/23)$ overlaid.

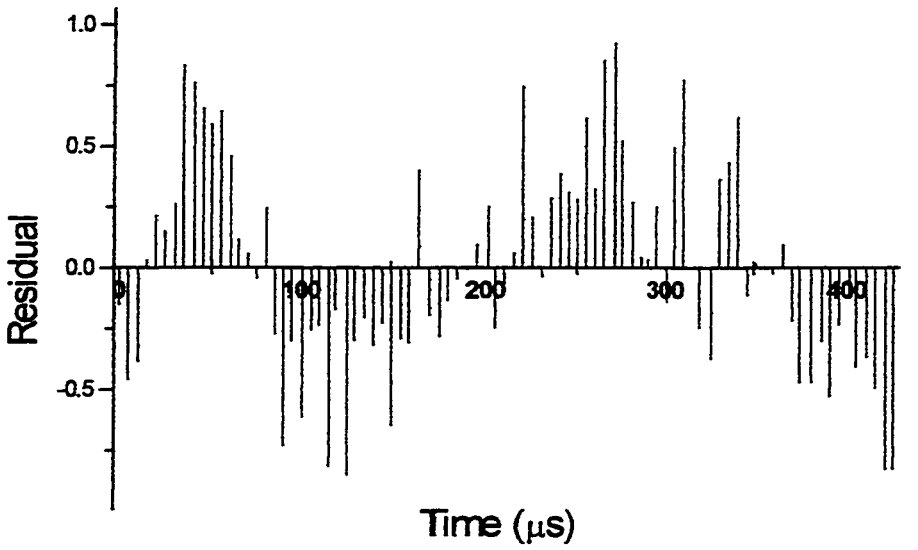

Figure 3.16 Plot of residuals (averaged every 5 μs) from the data shown in Figure 3.15 for decay of the 630-nm signal for 532-nm excitation. The repeating pattern suggests an instrumental artifact.

The relative intensities for the three exponential components in Figure 3.17 are proportional to the *component concentration multiplied by the corresponding extinction coefficient*. While the extinction coefficients of these species are unknown, they are likely of the same order of magnitude at 400-nm, all arising from MLCT transitions. This places the $Cr(CNPh)_5S$ component (i.e. 23 μs component) at a concentration at least an order of magnitude smaller than the 12 μs and 214 μs components. The charge neutral

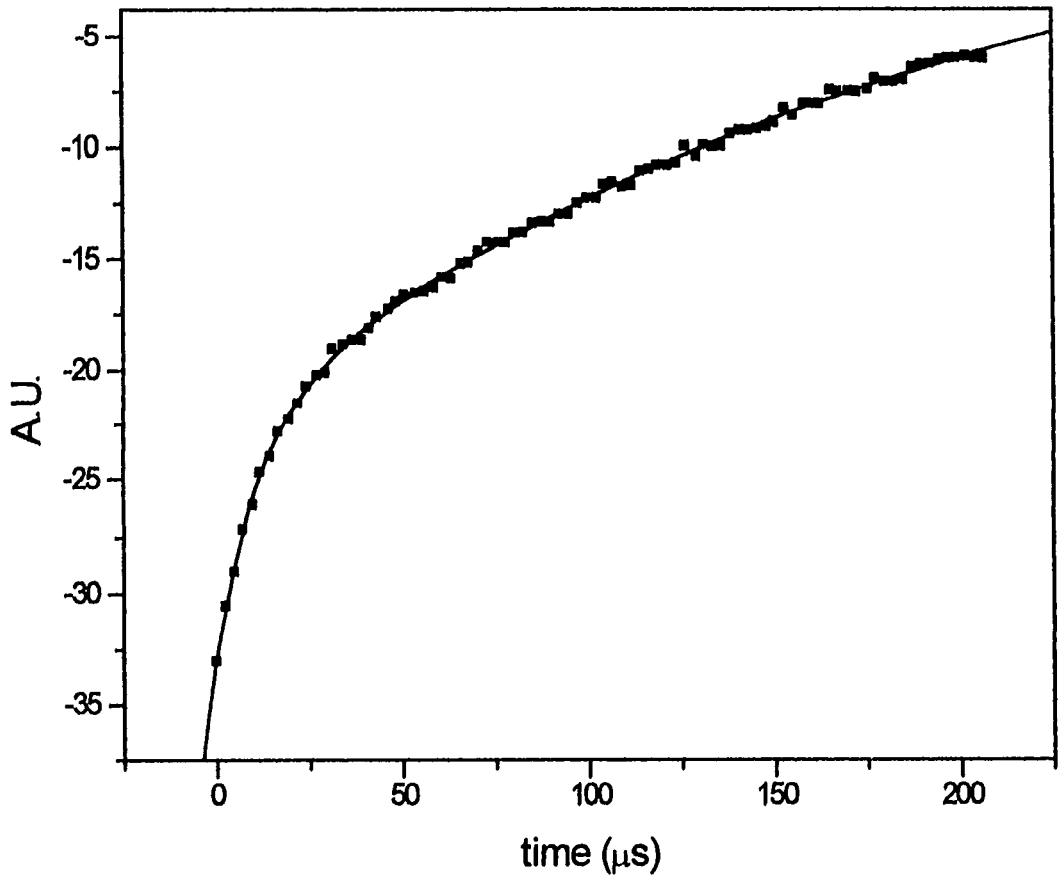

Figure 3.17 Bleach recovery at 400 nm for 532 nm flash photolysis with the exponential function y =4.69 - 0.101*exp(-x/23) - 10.5*(-x/12) - 27.1*exp(-x/214) overlaid.

pathway appears to account for only a small fraction of the total photochemistry at 532-nm. The smaller concentration of $Cr(CNPh)_5S$ produced by 532-nm excitation may be the cause of the poor signal to noise ratio seen in Figure 3.15. (Note that the intensities cannot be compared among the data in Figures 3.13 - 3.17 because of different photomultiplier gain and the fact that measured intensities are not in true absorbance units.)

3.4.5 Picosecond Absorption Spectroscopy

Picosecond absorption spectra of $Cr(CNPh)_6$ in neat benzene for 355-nm and 532-nm excitation are shown for the 0 ps - 1 ns time period in Figures 3.18 - 3.21. When interpreting these spectra, the standard deviation of up to $\pm$ 0.05 absorbance units must be considered.

The picosecond spectra with a 355-nm pump wavelength show a large bleach signal (approximately 420-520 nm) and a large ESA in the long wavelength region (520-640 nm). This ESA was assigned to the solvated species $Cr(CNPh)_5S$ in the previous section. The long wavelength $Cr(CNPh)_5S$ signal is fully formed within the 355-nm pulse (i.e. < 20 ps).

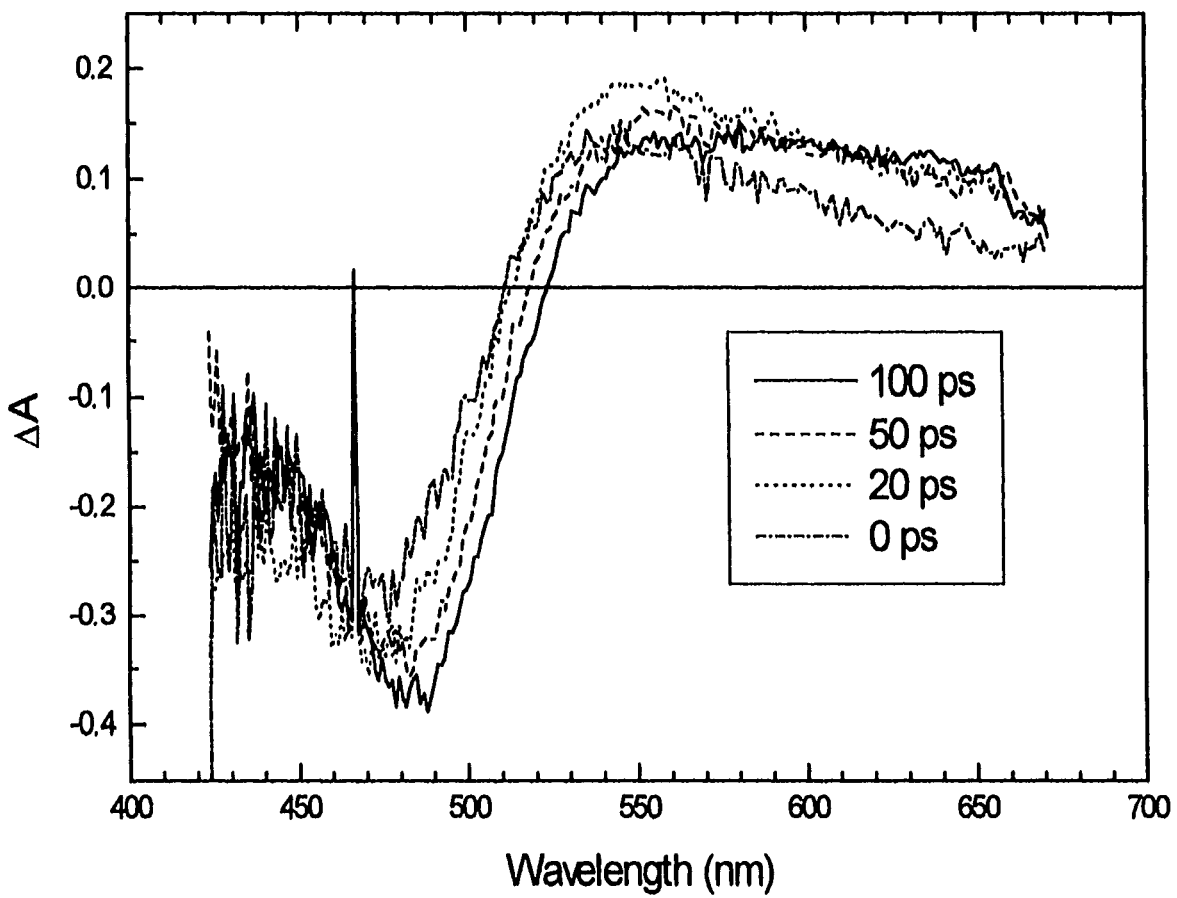

Figure 3.18 Picosecond absorption spectra of $Cr(CNPh)_6$ in neat benzene. 355-nm pump, $[Cr(CNPh)_6] = 3 \times 10^{-5}$ M. Time delays 0 ps, 20 ps, 50 ps, and 100 ps.

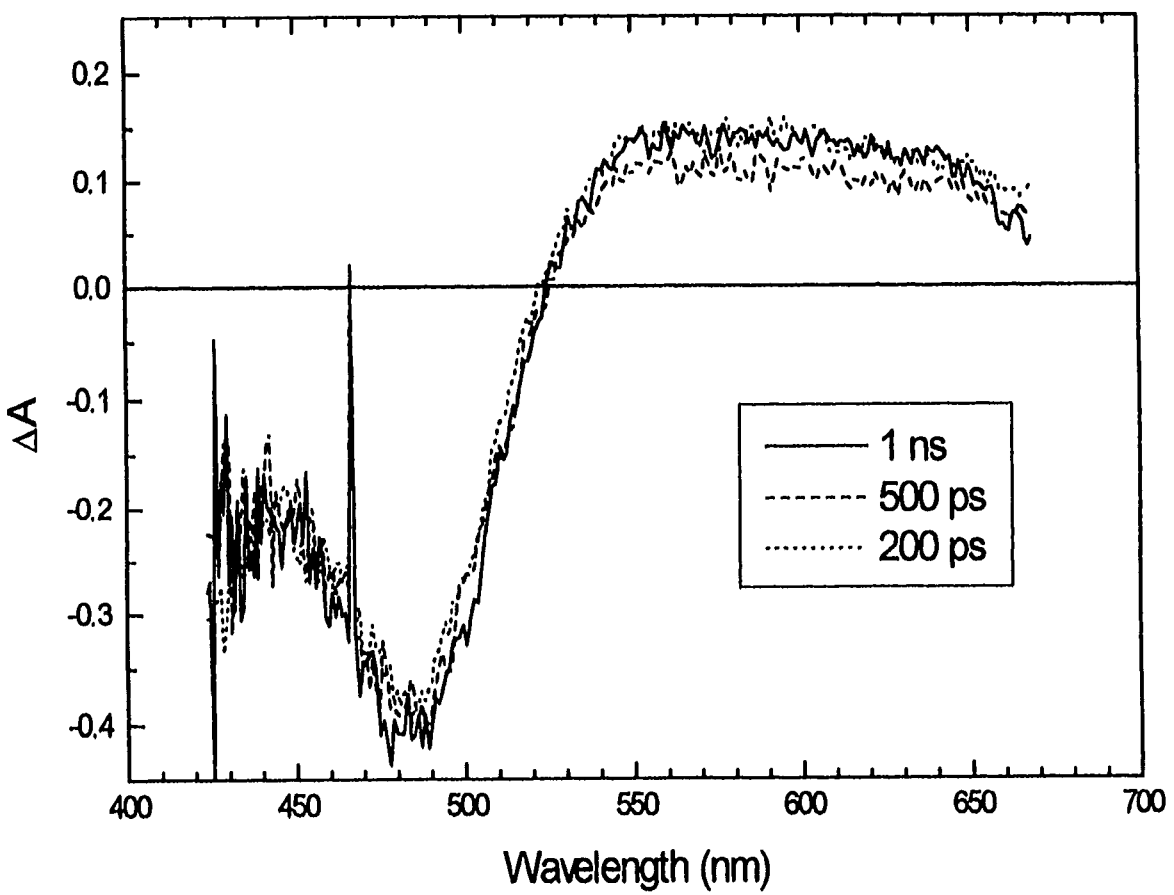

Figure 3.19 Picosecond absorption spectra of of $Cr(CNPh)_6$ in neat benzene. 355-nm pump, $[Cr(CNPh)_6] = 3 \times 10^{-5}$ M. Time delays 200 ps, 500 ps, and 1 ns.

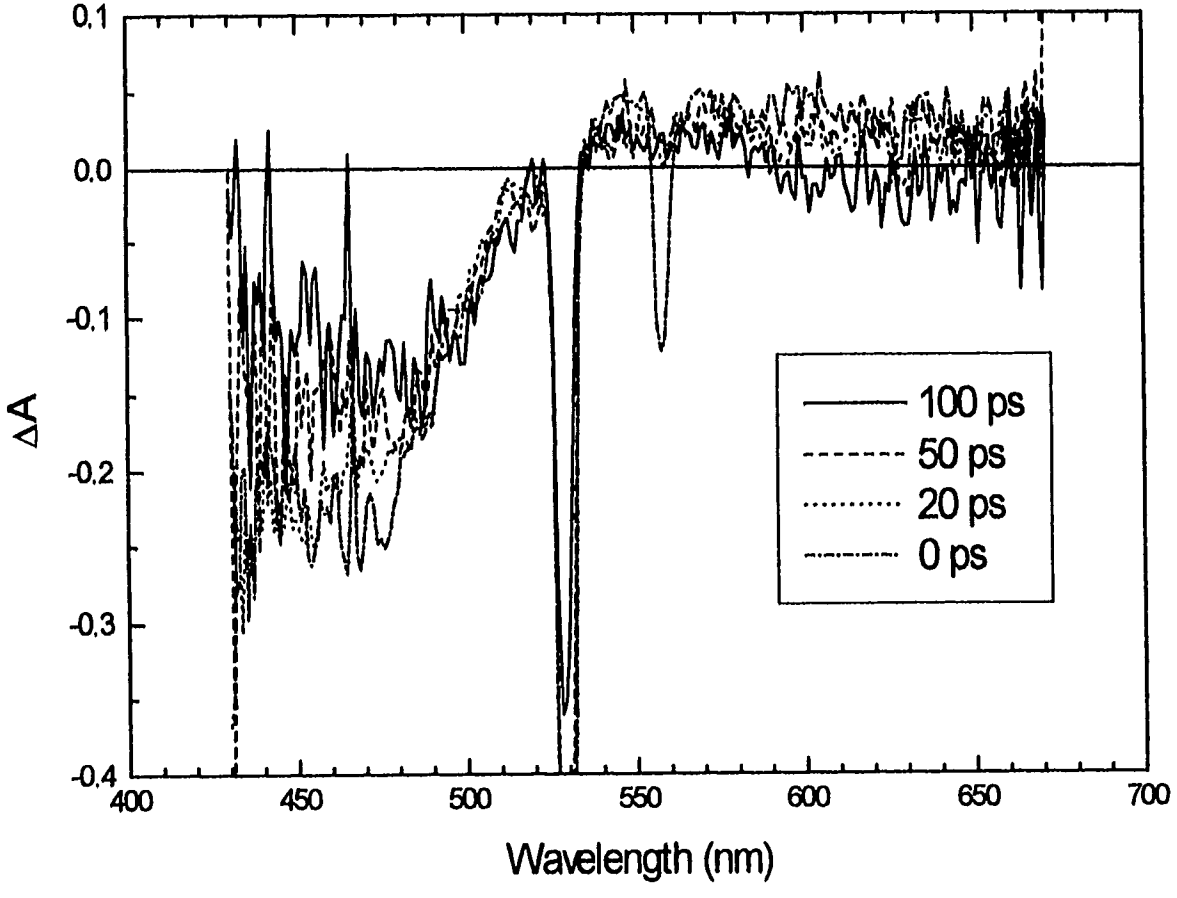

Figure 3.20 Picosecond absorption spectra of of $Cr(CNPh)_6$ in neat benzene. 532-nm pump, $[Cr(CNPh)_6] = 9 \times 10^{-5}$ M. Time delays 0 ps, 20 ps, 50 ps, and 100 ps.

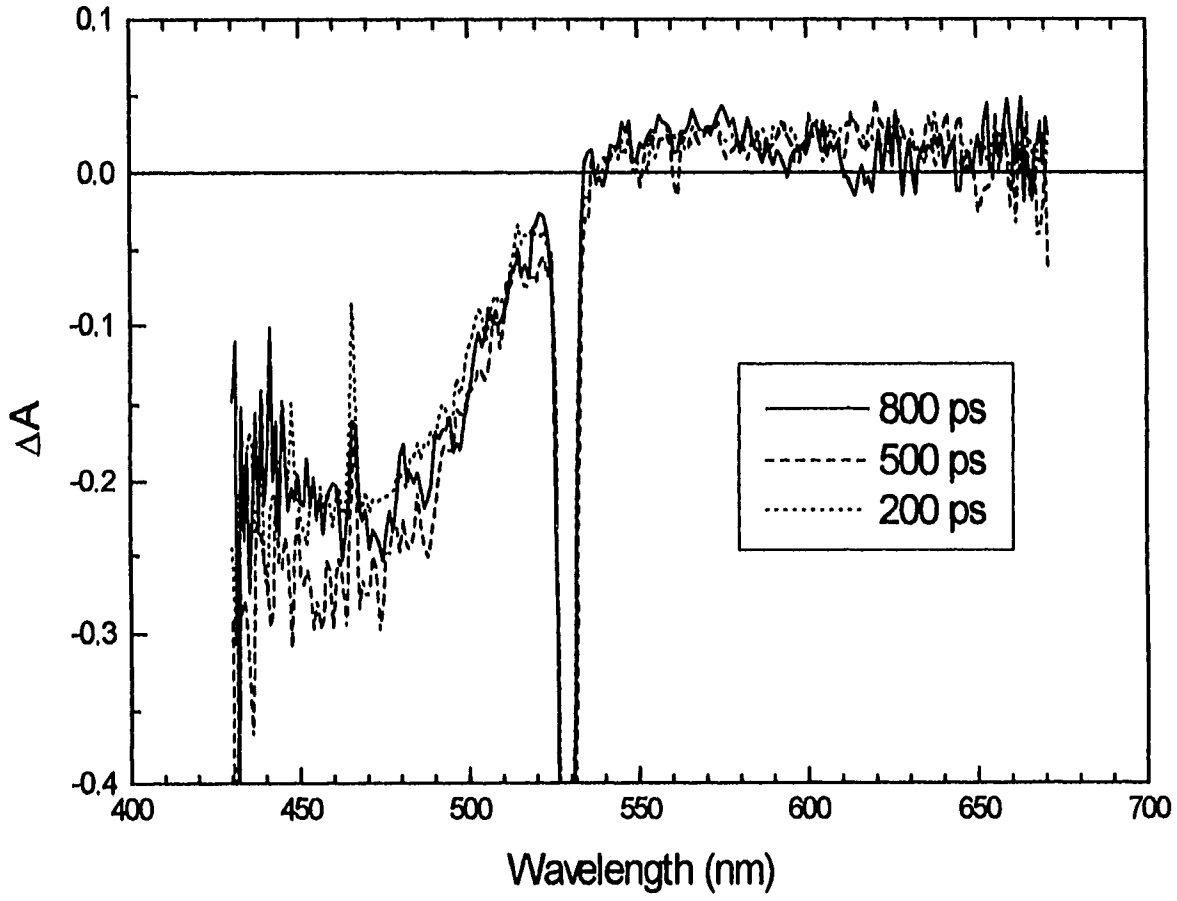

Figure 3.21 Picosecond absorption spectra of of $Cr(CNPh)_6$ in neat benzene. 532-nm pump, $[Cr(CNPh)_6] = 9 \times 10^{-5}$ M. Time delays 200 ps, 500 ps, and 800 ps.

The picosecond spectra for 532-nm excitation are noticeably different. The bleach signal remains, but the $Cr(CNPh)_5S$ absorption is significantly weaker than under 355-nm excitation. Unlike the nanosecond data above, these spectra provide measurements in true absorbance units. This allows for quantitative comparisons between spectra, provided that ground state absorbances (or concentrations) are known. At the laser intensities used here, 100% of all absorbing molecules exposed to the laser flash are excited, thus simplifying the comparisons.

The relative efficiencies for $Cr(CNPh)_5S$ formation between 355- and 532-nm can be calculated according to:

$$\frac{\phi_{355}}{\phi_{532}} = \frac{\left(\frac{\Delta A_{600,355}}{[Cr(CNPh)_6]_{355}}\right)}{\left(\frac{\Delta A_{600,532}}{[Cr(CNPh)_6]_{532}}\right)}$$

The change in absorbance ΔA_{600} was used because the ground state absorbance is negligible at this wavelength and there should be no bleach overlap. The concentrations of $Cr(CNPh)_6$ were determined from UV-vis absorption. All other terms cancel out, and are not shown in the equation. Using this equation and the data in Figures 3.19 and 3.21, $\phi_{355}/\phi_{532} \cong 20$. This means that the relative efficiency for $Cr(CNPh)_5S$ formation is 20 times greater at 355-nm than at 532-nm. This supports the interpretation of intensities of

the exponential components from Figure 3.17 that the charge neutral pathway accounts for a small amount of the total photochemistry at 532-nm.

Figures 3.22 - 3.24 show picosecond absorption spectra of $Cr(CNPh)_6$ in highly concentrated solutions of triphenylphosphine (PPh_3) under 355-nm excitation. Figure 3.22 shows the case for 1.0 M PPh_3. The initial $Cr(CNPh)_5S$ signal evolves to the final $Cr(CNPh)_5PPh_3$ product signal with $t_{1/2} \cong 30$ ps. Figures 3.23 and 3.24 show the case for 0.1 M PPh_3. The substitution process takes significantly longer, with $t_{1/2} \cong 200$ ps. This will be discussed in a later section.

Picosecond transient absorption spectra of $Cr(CNPh)_6$ were also obtained in toluene, tetrahydrofuran, dimethylsulfoxide, and pyridine. The changes observed in these other solvents are generally similar to those observed in benzene. These spectra are provided in Appendix C.

3.5 Excited State Model

From the time resolved data and the photosubstitution and electron transfer reactivity of $Cr(CNPh)_6$, it is reasonable to propose that there are two main photochemical pathways:

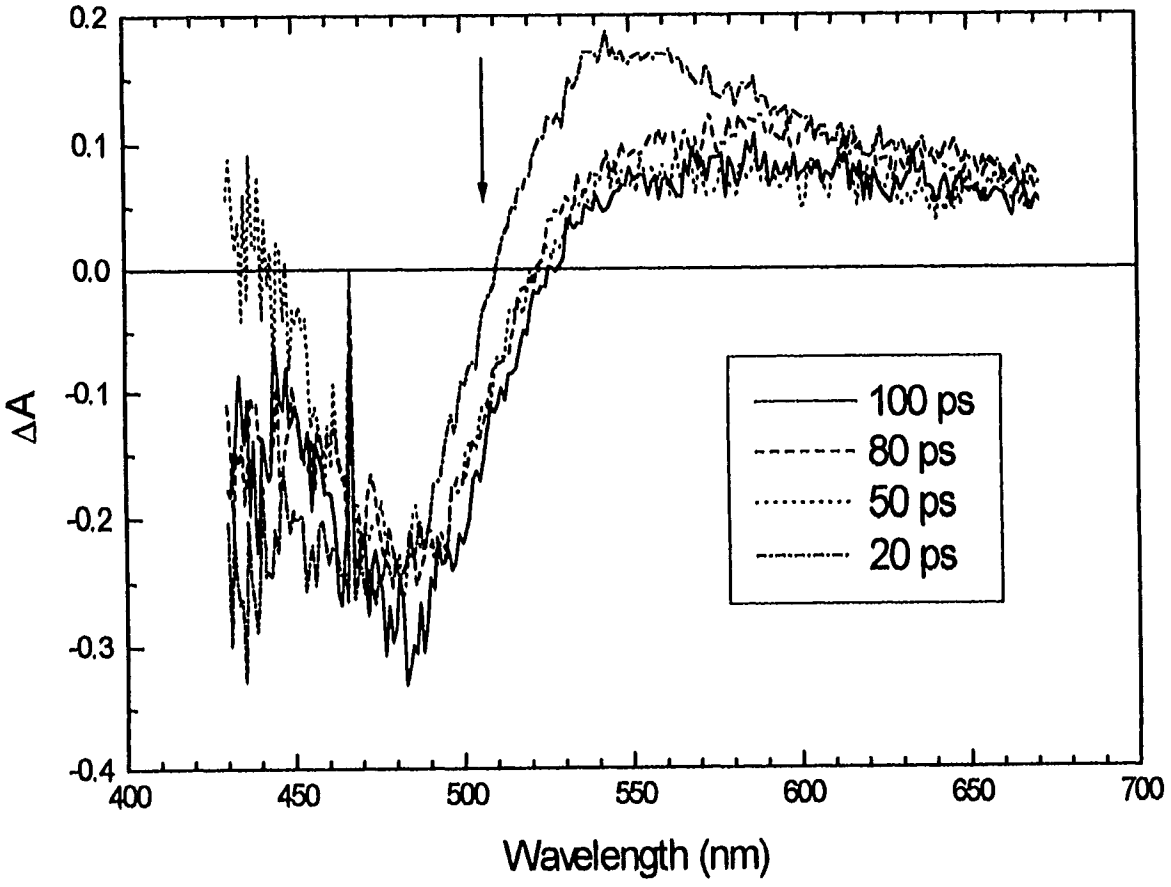

Figure 3.22 Picosecond absorption spectra of $Cr(CNPh)_6$ in 1.0 M PPh_3 benzene. 355-nm pump. Time delays 20 ps, 50 ps, 80 ps, and 100 ps.

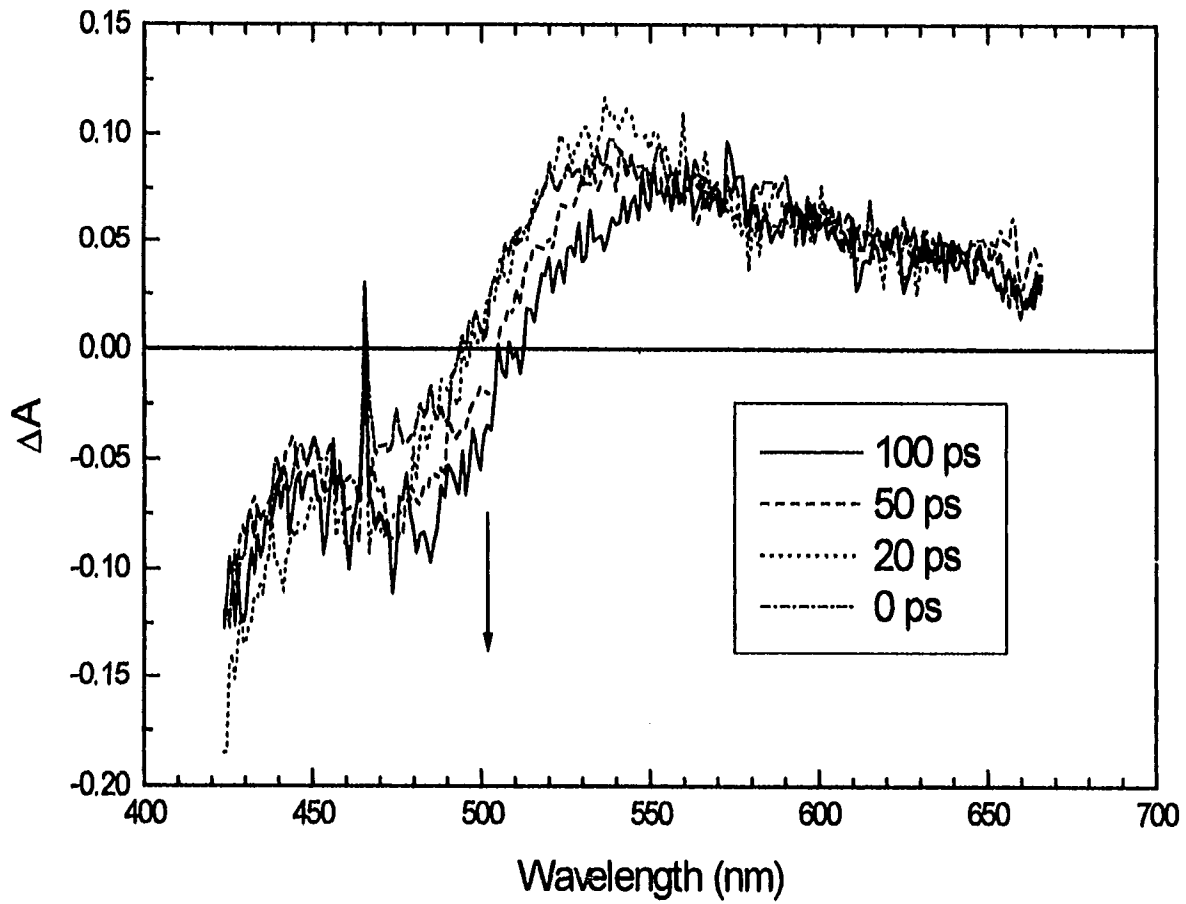

Figure 3.23 Picosecond absorption spectra of $Cr(CNPh)_6$ in 0.1 M PPh_3 benzene. 355-nm pump. Time delays 0 ps, 20 ps, 50 ps, and 100 ps.

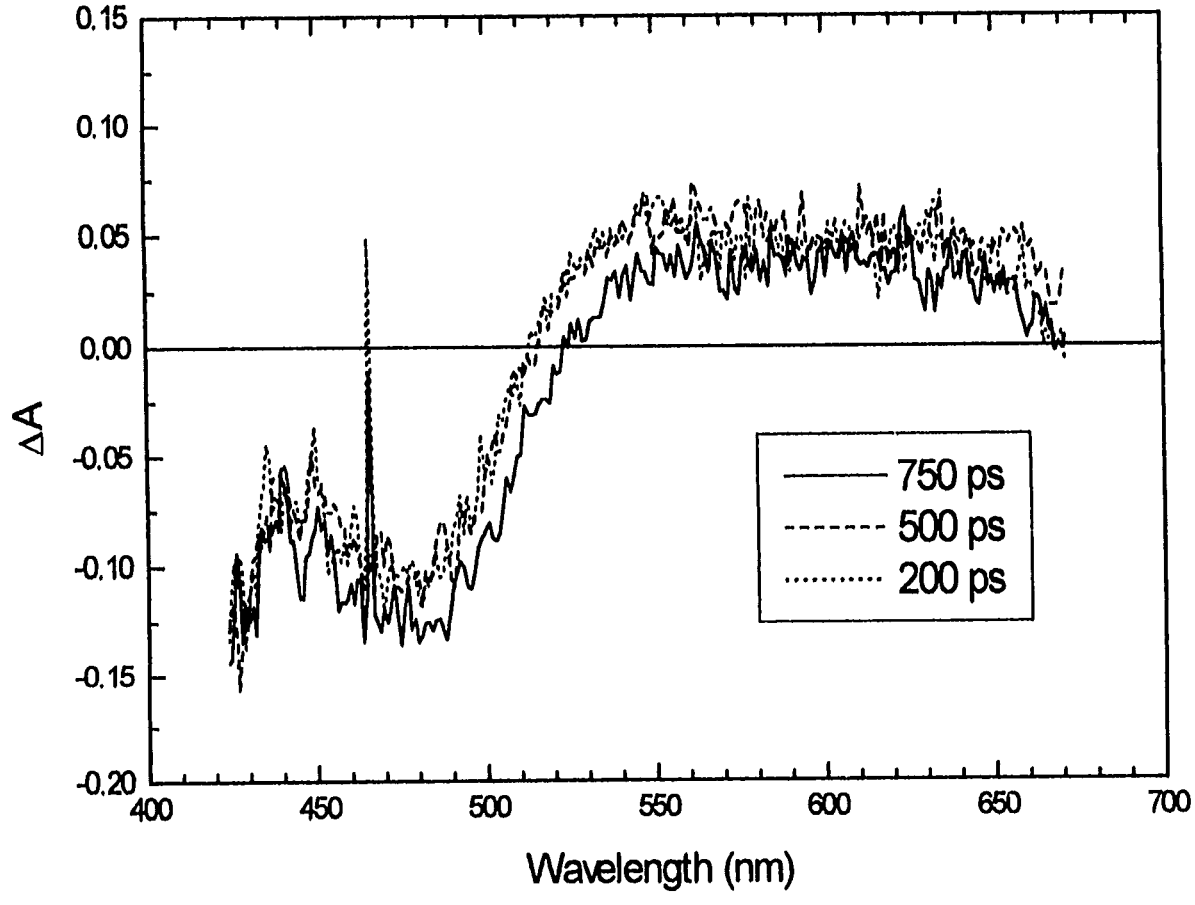

Figure 3.24 Picosecond absorption spectra of $Cr(CNPh)_6$ in 0.1 M PPh_3 benzene. 355-nm pump. Time delays 200 ps, 500 ps, and 750 ps.

1. Charge neutral photosubstitution.

$$Cr(CNPh)_6 \xrightarrow{h\nu, S} Cr(CNPh)_5S + PhNC$$

This involves the heterolytic dissociation of a neutral PhNC ligand. This pathway is responsible for the simple monoexponential 23 μs recoveries in the nanosecond data for 355 nm excitation.

2. Electron transfer mediated photosubstitution

This pathway is dominant in the long wavelength region and is summarized in Figure 3.25. The dissociation of a phenylisocyanide radical anion directly and promptly from a MLCT state would give rise to the unusual combination of *both* substitution and electron transfer processes that are observed. At 532 nm, the quantum yields for both substitution and electron transfer are identical. The processes responsible for the additional kinetic components of bleach recovery from 532 nm excitation (Figure 3.17) are assigned as:

$$\{Cr^{+}(CNPh)_5, PhNC^{-\bullet}\} \rightarrow Cr(CNPh)_6 \qquad \tau = 12\ \mu s$$

$$\{Cr^{+}(CNPh)_5S, PhNC^{-\bullet}\} \rightarrow Cr(CNPh)_6 \qquad \tau = 214\ \mu s$$

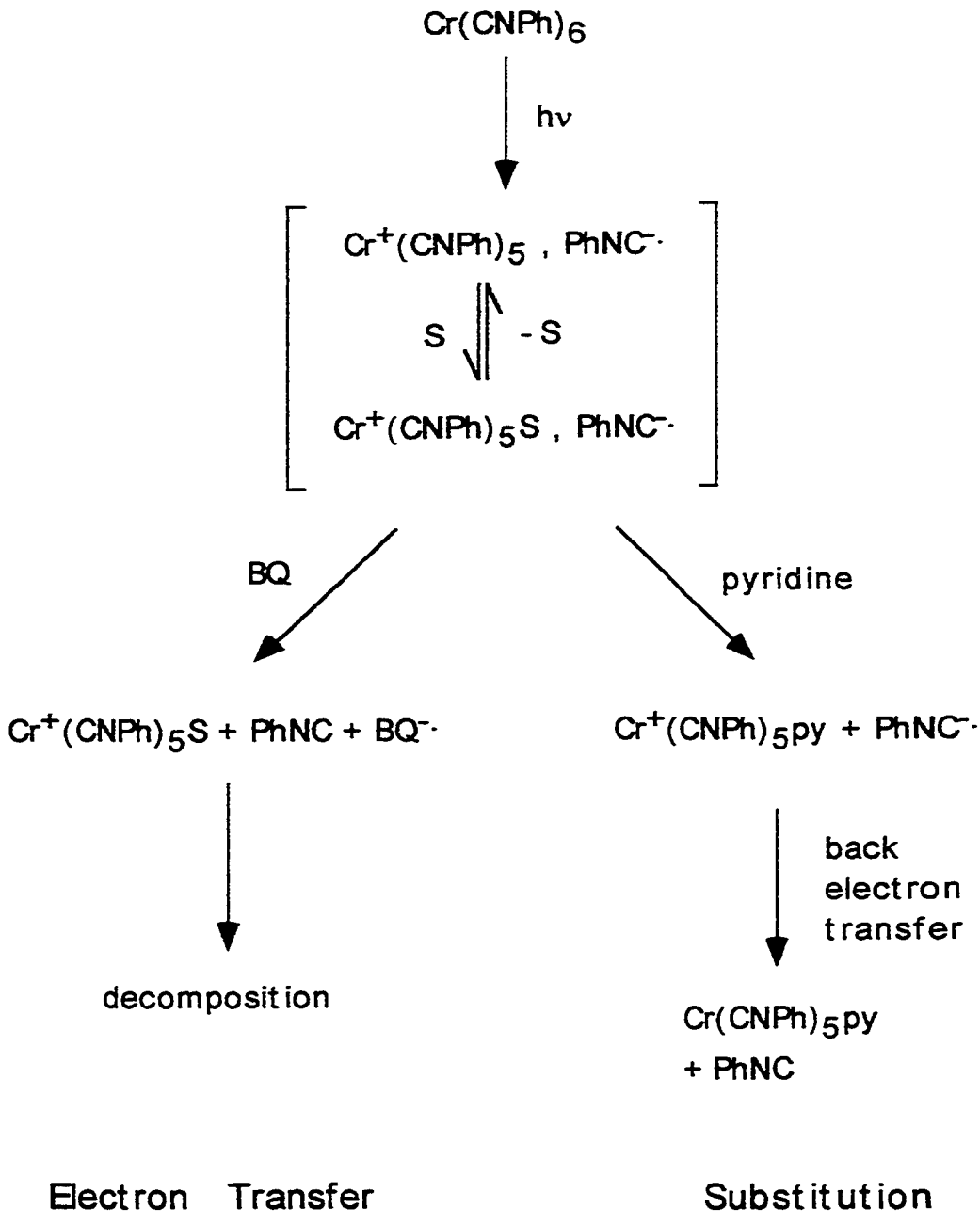

Figure 3.25 Electron transfer mediated photosubstitution pathway in $Cr(CNPh)_6$. The braces around the initial photoproducts indicate that both 'naked' and solvated species are each potentially responsible for the overall reactions, and that there may be an interchange between the two forms.

Resonance Raman experiments have shown the presence of a unique absorption in the long wavelength region.[57] Between 454.5 nm and 514.5 nm, the signals for the δ(Cr-C-N) and δ(C-Cr-C) bending modes dramatically increase in intensity. The excited state displacements along two normal coordinates (Δ_a , Δ_b) can be compared according to:

$$\frac{I_a}{I_b} = \frac{\omega_a^2 \Delta_a^2}{\omega_b^2 \Delta_b^2}$$

where I_a and I_b are the intensities of the bands in the preresonance Raman spectrum and ω_a and ω_b are the frequencies. Relative to the ν(C≡N) mode, the relative displacements of the δ(Cr-C-N) and δ(C-Cr-C) modes increase from 2.7 to 7.2 and 0 to 11.7 respectively, on going from 454.5 to 514.5 nm. There is clearly a unique absorption in the tail of the broad MLCT absorption that is responsible for these large excited state distortions.

The excited state diagram in Figure 3.26 provides a possible framework for the interpretation of the resonance Raman data and the wavelength dependences of picosecond spectra, nanosecond kinetics, and the quantum yields for electron transfer and substitution.

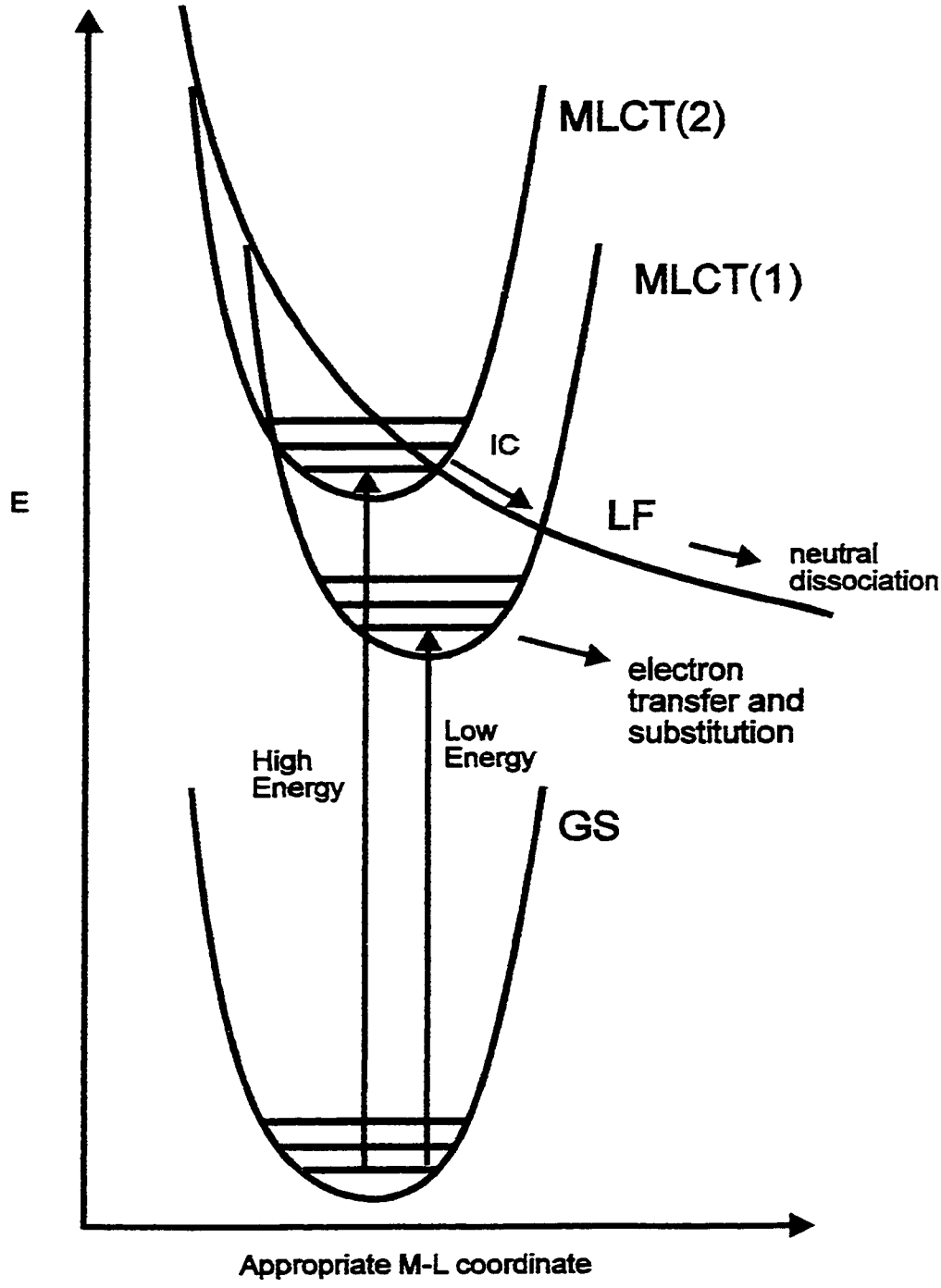

Figure 3.26 Excited state diagram of $Cr(CNPh)_6$. The charge neutral pathway comes from population of MLCT(2), followed by internal conversion (IC) to a ligand field (LF) state. Electron transfer mediated substitution comes from MLCT(1).

When $Cr(CNPh)_6$ is irradiated with a high energy photon ($\cong$ 300 - 450 nm), the higher MLCT(2) state is populated. An internal conversion (IC) to a ligand field state can occur, leading to charge neutral dissociation of a PhNC ligand. The photochemical loss of CO in $Mn_2(CO)_{10}$ and $MnCl(CO)_5$ has been studied theoretically.[83-85] In both systems, the antibonding LF states responsible for CO dissociation are at high enough energy at equilibrium ground state geometries that they are not directly populated by irradiation into the lowest energy states, which are $\sigma \rightarrow \sigma^*$ states (antibonding for the Mn-Mn and Mn-Cl bonds). Despite this, CO loss occurs on excitation into these low energy absorptions. There is significant theoretical evidence[83-85] that there is a precipitous decrease in the energies of the LF states with small increases in the Mn-CO bond length. A strongly avoided crossing between the LF state and the lowest energy excited state leads to an essentially barrierless CO dissociation. $Cr(CNPh)_6$ is similar to these manganese carbonyls: the LF states are expected to lie at much higher energies than the MLCT states, yet the presence of a charge neutral, heterolytic pathway strongly implies the involvement of antibonding LF states.

The MLCT(1) state is populated with low energy photons ($\cong$ 450 - 550 nm). This MLCT absorption is strongly coupled to the δ(Cr-C-N) and δ(C-Cr-C) bending vibrations[57], providing distortions that may lead to substitution. The maximum yield for electron transfer occurs when this state is populated. The limiting yields for both substitution and

electron transfer are the same in this region. Both reactions occur from the same primary process - the formation of a radical pair:

$$Cr(CNPh)_6^* \rightarrow \{Cr^+(CNPh)_5, PhNC^{-\bullet}\}$$

From the wavelength dependence of electron transfer (Figure 3.12), it is clear that there is a wavelength region ($\cong$ 360 - 480 nm) where the MLCT(1) pathway is present but does not account for 100% of the total substitution reactivity (Figure 3.9). There may be some overlap of MLCT absorptions that accounts for this behaviour, or internal conversions between MLCT(1) and MLCT(2) are occurring - most likely from MLCT(2) to MLCT(1).

3.6 Discussion

The nucleophile and electron acceptor concentration dependences provide information about the lifetime of reactive species in solution. In benzene, the diffusion controlled rate constant can be estimated by the Smoluchowski-Stokes-Einstein equation[47]:

$$k_{diff} = \frac{8RT}{3\eta} 10^3$$

where R is the gas constant, T is the temperature, and η is the viscosity. For reactions at 20° C in benzene, k_{diff} is estimated at 1.0×10^{10} $M^{-1}s^{-1}$.

From the ϕ_{sub} dependence on pyridine concentration (Table 3.1), ϕ_{sub} remained limiting at 4×10^{-4} M pyridine. The reactive intermediate must have a lifetime in excess of $\tau = [(4 \times 10^{-4}\ M) \times (1.0 \times 10^{10}\ M^{-1}s^{-1})]^{-1} = 250$ ns, since the maximum rate constant is k_{diff}. The minimum lifetime of a reactive intermediate is important mechanistically. Substitution likely occurs on a solvated intermediate $Cr(CNPh)_5S$ or $Cr^{+}(CNPh)_5S$, which were found to have lifetimes of 23 μs and 214 μs respectively - much longer than the minimum lifetime calculated above.

From the picosecond absorption experiments with large PPh_3 concentrations, it is apparent that much of the reaction occurs on a time scale that is much faster than the minimum lifetime of 250 ns. To understand these results, the equilibrium constant for the pre-equilibrium

$$Cr(CNPh)_6 + PPh_3 \rightleftharpoons \{Cr(CNPh)_6,PPh_3\}$$

was estimated using the Fuoss-Eigen equation for charge neutral species[86]:

$$K = \frac{4\pi}{3} a^3 N_A$$

where N_A is Avogadro's number and **a** is the sum of molecular radii in angstroms. The molecular radius of $Cr(CNPh)_6$ was estimated at 8.5 Å, based on the X-ray structure. The radius for PPh_3 was estimated at 6.7 Å. This provides $K \cong 8.9\ M^{-1}$.

Figure 3.27 depicts the relevant pre-equilibria to explain the photochemistry observed in the picosecond experiments. At 1.0 M PPh_3, the fraction of $Cr(CNPh)_6$ molecules in encounter with PPh_3 is estimated at 0.90. Thus, 90% of the $Cr(CNPh)_5S$ formed is also in encounter with PPh_3 (pathway 2 in Figure 3.27). The other 10% goes through pathway 1, and the reaction with PPh_3 is subject to the limits of diffusion (i.e. $k_1 \cong k_{diff}$). The fast absorbance changes seen for 1.0 M PPh_3 are due to the dominance of pathway 2, which is not diffusion controlled.

At 0.1 M PPh_3, the fraction of $Cr(CNPh)_6$ in encounter with PPh_3 is estimated at 0.47. Significant absorption changes occur in under 100 ps, as in the case of 1.0 M PPh_3. However, the absorption changes that are resolved up to 700 ps are due to pathway 1, responsible for the remaining 53% of $Cr(CNPh)_6$ molecules.

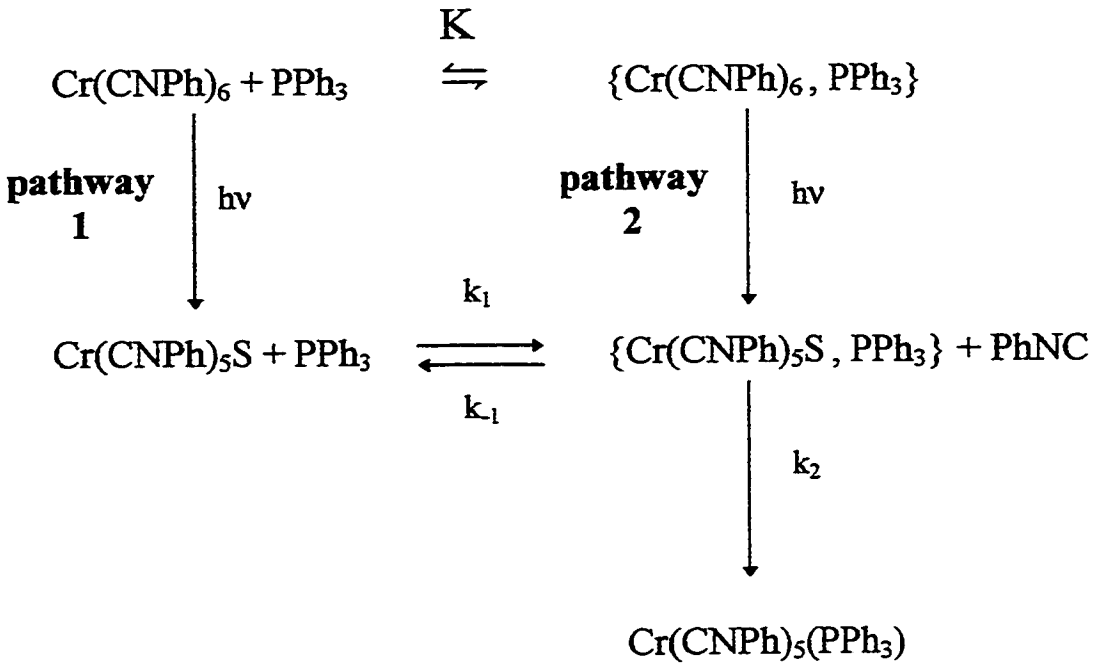

Figure 3.27 Pre-equilibria in $Cr(CNPh)_6$ - PPh_3 systems. Note that this only includes the charge neutral pathway. The picosecond experiments on these systems involved 355 nm flashes, and at this wavelength the charge neutral pathway is dominant. Pathway 1 involves species that are not initially in encounter. In pathway 2, the reactants are already in encounter when a photon is absorbed.

A previously reported wavelength dependence for photosubstitution in $Cr(CNPh)_6$ had an unusual increase in ϕ_{sub} in the long wavelength region.[57] This was interpreted using the resonance Raman data above. This work has shown that the original wavelength dependence is incorrect - probably due to errors in fulgide actinometry in the 400 - 450 nm region.

The wavelength dependence for substitution in both benzene and pyridine (Figures 3.9, 3.10) show a simple decrease in ϕ_{sub} with decreasing energy across the wavelengths studied. The monotonous decreases are not interrupted with the change in substitution mechanism that occurs. The wavelength dependence of ϕ_{sub} seems to be independent of mechanism in $Cr(CNPh)_6$.

The picosecond data on $Cr(CNPh)_6$ indicate that products are formed in less than 20 ps at both 355 and 532 nm. Both reaction mechanisms involve primary photosteps that occur on the ultrafast time scale. The overall quantum yield is highly dependent on the excess excitation energy. If both reaction modes were occurring from thermally equilibrated excited states, ϕ_{sub} would change abruptly as the different states were populated. This is not the case here, and ϕ_{sub} seems more dependent on the caging dynamics of the system than on the nature of excited state populations.

An integral part of the coupled electron transfer - substitution mechanism is that $PhNC^{-\bullet}$ is responsible for electron transfer. An alternate possibility is that photoproduced $Cr(CNPh)_5S$ is oxidized by benzoquinone. If that were the case, the quantum yields for electron transfer would be as high as the substitution yields at every wavelength studied. This is not the case.

The mechanism for the photochemical cycle in section 3.3.3 also depends on electron transfer from $PhNC^{-\bullet}$. The cycle is depicted in Figure 3.28. Electron transfer from $PhNC^{-\bullet}$ to TBP leads to the formation of a transient precipitate $\{Cr^{+}(CNPh)_5S, TBP^{-\bullet}\}$, leading to back electron transfer and back substitution to form $Cr(CNPh)_6$. With TBP as an electron acceptor, back electron transfer to $Cr^{+}(CNPh)_5S$ is favourable and negligible decomposition occurs, in contrast to the case with benzoquinone.

This cycle suggests a type of photochemical switch, where the opacity of a medium increases with irradiation as the precipitate forms, but recovers to a transparent state in the dark. Below critical $Cr(CNPh)_6$ concentrations of about 10^{-5} M, precipitates are not observed - although the final bimolecular step is still seen. The changes in solution absorption for this step are large, enough to provide for a second potential application in photochemical switching (i.e. reversible colour change). The properties of the cycle can be controlled by changing the concentrations of $Cr(CNPh)_6$ and the excess ligand PhNC.

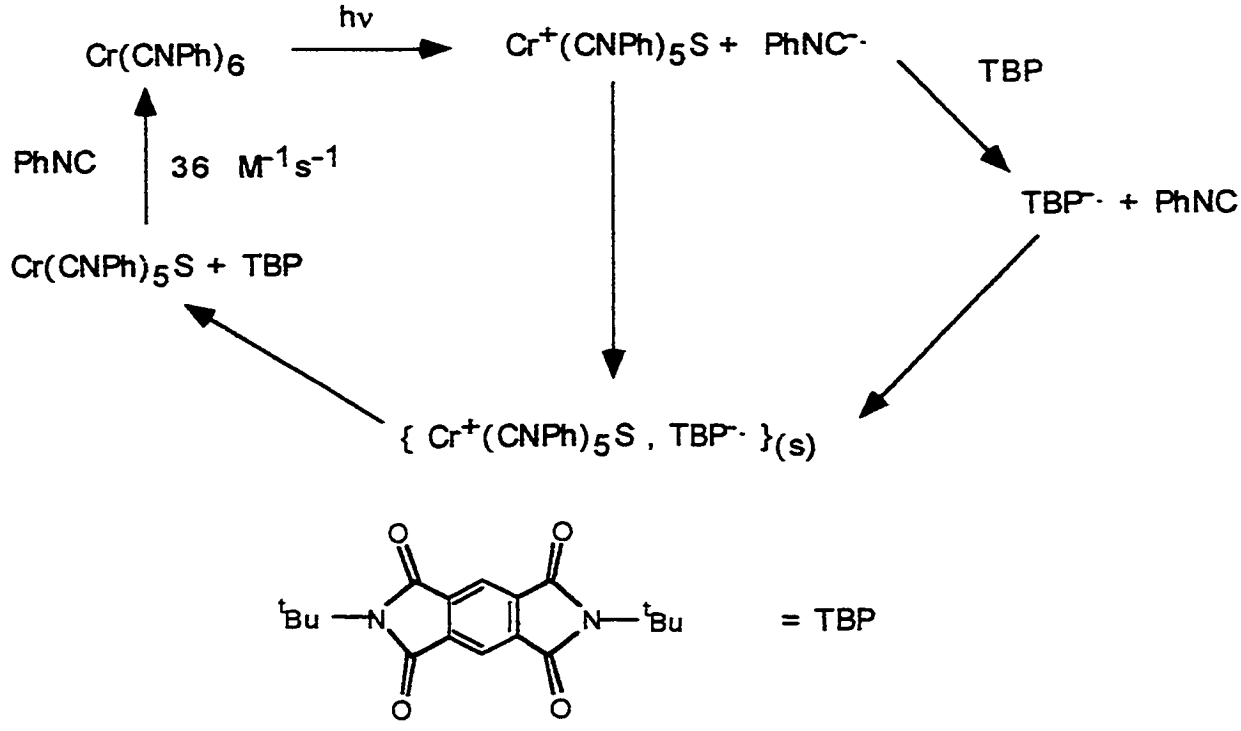

Figure 3.28 Mechanism for photoinduced electron transfer cycle in $Cr(CNPh)_6$.

The $Cr(CNPh)_6$ system may constitute the first case of a photodissociation of an organic ligand radical *anion* directly and promptly from the corresponding MLCT state. Photochemical homolytic dissociation of alkyl, halide, or metal complex fragment radicals in Group 7 complexes containing α-diimine ligands is well known.[35,36,87,88] Such reactions are thought to arise from σ–π^* states, labilizing bonds on the axis orthogonal to the metal- α-diimine ligand plane. The mechanism presented here for the low energy $Cr(CNPh)_6$ photochemistry is complementary to σ–π^* reactivity in the sense that the excitation is localized on the ligand that is to be dissociated rather than on a neighoring group. The microscopic reasons for the dissociation of $PhNC^{-\bullet}$ on MLCT excitation are not entirely clear at this time. However, resonance enhancement of the Raman bands corresponding to the δ(C-Cr-C) and δ(Cr-C-N) bending vibrations indicates that these molecular distortions are coupled to the MLCT transition in the long wavelength region.[57] These distortions may lead to the ultrafast dissociation of $PhNC^{-\bullet}$. The mechanism for the low excitation energy substitution pathway is further discussed in Chapter Four.

3.7 Future Work

Future work includes a complete study of the solvent dependence of ϕ_{sub}. This is challenging with $Cr(CNPh)_6$ due to its insolubility in many common polar solvents and

its unexpected photochemistry in DMSO and toluene. Both classical and thermal cage effects are expected in this system. Time resolved spectroscopy on the femtosecond time scale may hold insights into the ultrafast photochemical processes (e.g. internal conversions) that appear to play a role in $Cr(CNPh)_6$ photochemistry. Electron paramagnetic resonance (EPR) spectroscopy may confirm the presence of radicals in the low excitation energy pathway. However, EPR experiments are potentially challenging because the photochemical instability of the complex and fast rate of radical recombination are likely to prevent the formation of a detectable steady-state concentration of radicals.

CHAPTER FOUR: THE PHOTOCHEMISTRY OF $Mo(CNPh)_6$

4.1 Introduction

In $Mo(CNPh)_6$, stuctural and electronic properties are very similar to those of the chromium analogue which has been discussed in Chapter Three. The visible spectrun of $Mo(CNPh)_6$ is dominated by intense MLCT absorptions. Ligand field states are expected to be at higher energies than the chromium analogue due to the larger ligand field splitting of molybdenum. The photochemistry of $Mo(CNPh)_6$ is similar to $Cr(CNPh)_6$ although the photochemical mechanisms prove to be different.

Unlike the Cr analogue, $Mo(CNPh)_6$ has an emissive excited state.[61,78] The emission is not substantially Stokes shifted (i.e. there is significant overlap of the lowest energy MLCT absorption and the emission maximum at 17900 cm^{-1}). This is suggestive of a thermally equilibrated excited state. At 77 K, the quantum yield of emission is 0.78. The emission lifetimes are 21 ns (298 K) and 23 μs (77 K).[78]

Molybdenum arylisocyanide complexes undergo photosubstitution in the presence of pyridine[61]:

$$Mo(CNAr)_6 \xrightarrow{hv,\ py} Mo(CNAr)_5py + CNAr$$

As in the case of $Cr(CNAr)_6$ complexes, the substitutional reactivity of homoleptic complexes of CNPh and CNIph were compared in order to establish the mechanism of photosubstitution on the basis of steric effects.[61] At 436 nm, the quantum yield for photosubstitution, ϕ_{sub}, was 0.055. The more sterically hindered complex $Mo(CNIph)_6$ had a quantum yield of 0.022. This was interpreted to mean that the photosubstitution has some associative character.

In $Mo(CNPh)_6$, ϕ_{sub} is 0.11 at 313 nm, different from the quantum yield at 436 nm.[78] Although limited to two points, the wavelength dependence is unusual considering the assignment of an associative mechanism - which would be expected to occur from the thermally equilibrated excited state. However, it is possible that nucleophilic attack on vibrationally 'hot' $Mo(CNPh)_6$ excited states would lead to a greater fraction of successful substitutions if nucleophiles are in encounter. Thus, only the solvent is a good candidate for 'hot' nucleophilic attack.

Photoinduced electron transfer chemistry in chloroform of the molybdenum complexes is less complicated than in $Cr(CNPh)_6$ due to the formation of well characterized products from one path.[78] When $Mo(CNPh)_6$ is irradiated in chloroform, the seven coordinate,

two electron oxidation product $[Mo(CNPh)_6Cl]^+$ is formed. Similar complexes have been synthesized independently. It was proposed that $[Mo(CNPh)_6Cl]^+$ is formed via the following mechanism:

$$Mo(CNPh)_6 \xrightarrow{h\nu} \{Mo(CNPh)_6^{+\cdot}\cdots CHCl_3^{-\bullet}\}$$

$$\{Mo(CNPh)_6^{+\cdot}\cdots CHCl_3^{-\bullet}\} \rightarrow \{Mo(CNPh)_6Cl^{+\cdot}\cdots CHCl_2^{\bullet}\}$$

$$\{Mo(CNPh)_6Cl^{+\cdot}\cdots CHCl_2^{\bullet}\} \rightarrow [Mo(CNPh)_6Cl]^+ + CHCl_2^{\bullet}$$

Excited state electron transfer leads to the formation of the radical pair $\{Mo(CNPh)_6^{+\cdot}\cdots CHCl_3^{-\bullet}\}$. Subsequent chlorine atom transfer to the $Mo(CNPh)_6^+$ provides the final product. The quantum yield for this reaction was reported to be 0.11 at 436 nm.[61]

The purpose of this investigation into the photochemistry of $Mo(CNPh)_6$ is to compare photochemical reactivity and mechanism with those of $Cr(CNPh)_6$. The associative mechanism of photosubstitution is tested via nucleophile dependence. Wavelength dependences of both photosubstitution and photoinduced electron transfer are also measured and compared to the chromium case.

4.2 Photosubstitution

4.2.1 Nucleophile Dependence

The nucleophile dependence of photosubstitution in $Mo(CNPh)_6$ was determined in order to test the putative associative mechanism. Quantum yields were determined in benzene with pyridine and triphenylphosphine as nucleophiles. At 436 nm, the quantum yield of photosubstitution was 0.17 ± 0.01 for both pyridine and PPh_3 (0.01 M). The spectral changes for these photochemical reactions are in Figures 4.1 and 4.2.

The absence of a nucleophile dependence is strong evidence for a dissociative mechanism. Thus, the previous assignment seems incorrect. The difference in reactivity of the CNPh and CNIph complexes may arise from differences in electronic structure. Alternatively, a Mo-C bond dissociation may require significant molecular distortions similar to those in $Cr(CNPh)_6$, seen in resonance Raman spectra.[57] The bulky, ortho isopropyl groups in the CNIph ligand could hinder C-Mo-C and Mo-C-N bending vibrations and hinder ligand dissociation.

4.2.2 Nucleophile Concentration Dependence

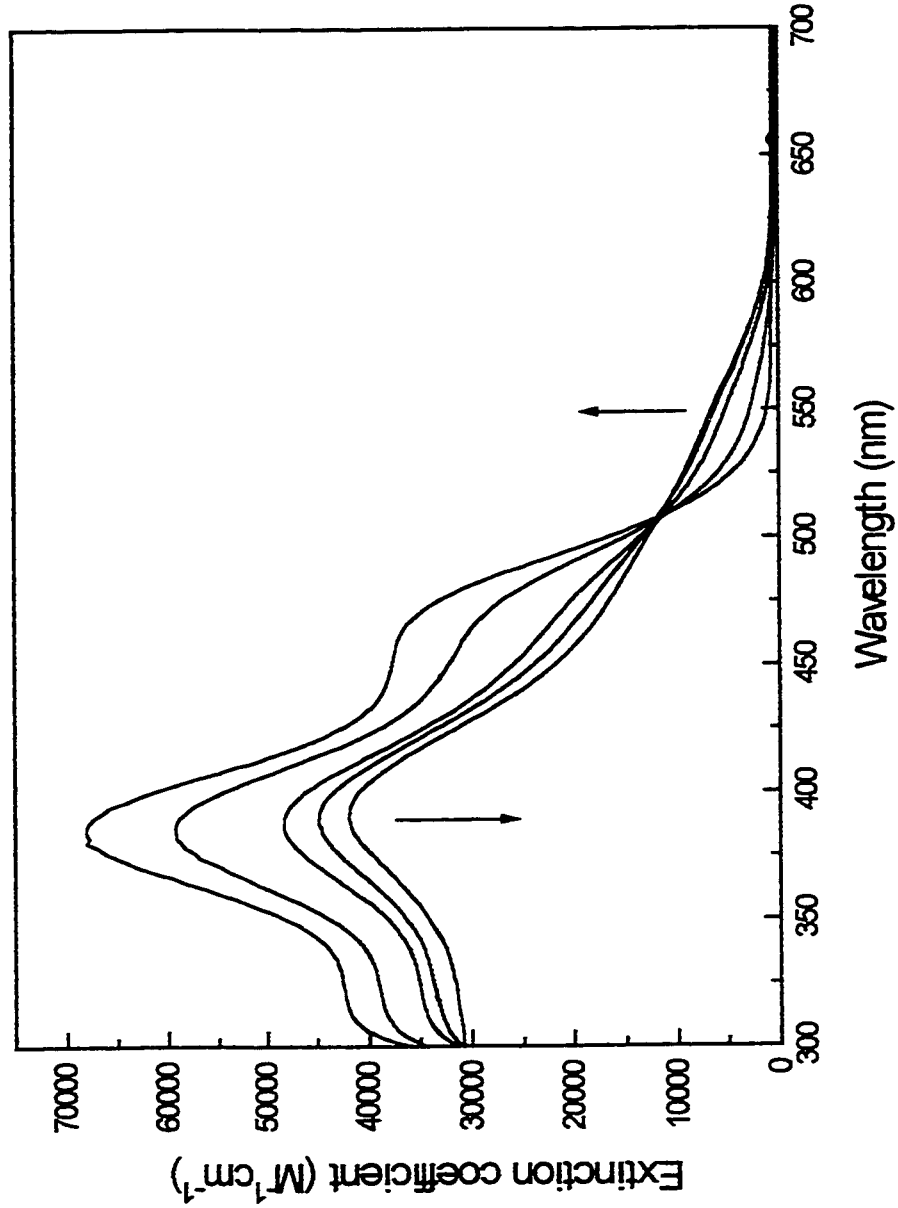

Figure 4.1 Spectral changes for the irradiation of $Mo(CNPh)_6$ in benzene with 0.01 M pyridine.

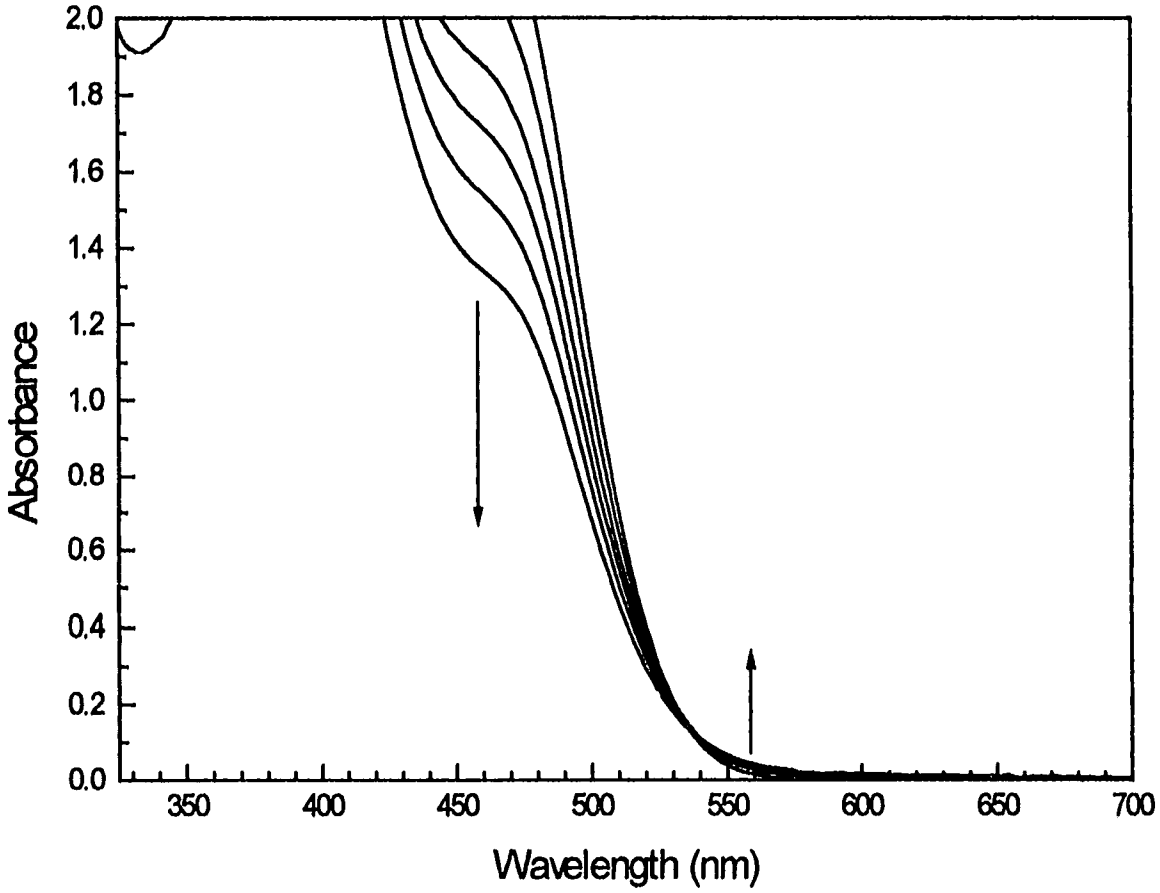

Figure 4.2 Spectral changes for the irradiation of $Mo(CNPh)_6$ in benzene containing 0.01 M PPh_3. $[Mo(CNPh)_6] = 7.0 \times 10^{-5}$ M.

Table 4.1 gives the dependence of ϕ_{sub} on pyridine concentration at 436 nm in benzene. The concentration of $Mo(CNPh)_6$ was between 4×10^{-5} and 2×10^{-4} M. Thus, the pyridine concentration was brought to within a factor of two of $[Mo(CNPh)_6]$. Quantum yields were determined from the first 10% conversion so that pseudo first order conditions were maintained independently of the overall order.

Table 4.1 $Mo(CNPh)_6$ Photosubstitution Quantum yield dependence on pyridine concentration in benzene

[py] (M)	Quantum yield (± 0.01)
0.10	0.18
1.0×10^{-2}	0.17
6.0×10^{-3}	0.16
2.0×10^{-3}	0.17
4.0×10^{-4}	0.17

Over three orders of magnitude in pyridine concentation there is no change in ϕ_{sub}. This supports the evidence above that the substitution is dissociative. The excited state has a lifetime of 21 ns at 298 K.[78] If substitution on the excited state was bimolecular, nucleophile concentration effects would be observed at nucleophile concentrations on the order of 5×10^{-3} M (estimated using the lifetime and the diffusion controlled rate

constant, $k_{diff} = 1.0 \times 10^{10}\ M^{-1}s^{-1}$ in benzene). This is not the case, so the nucleophile must be reacting with solvated species of the type "$Mo(CNPh)_5S$".

4.2.3 Wavelength Dependence

The wavelength dependence of ϕ_{sub} in neat pyridine was determined. Results are given in Table 4.2. Within experimental error, there is no wavelength dependence. These results confirm the previously reported 313 nm quantum yield but suggest that the previous 436 nm quantum yield (0.055)[61] is incorrect.

Table 4.2 Wavelength Dependence of Photosubstitution of $Mo(CNPh)_6$ in neat pyridine

Wavelength (nm)	Quantum yield (± 0.01)
313	0.11
365	0.11
436	0.12
488	0.12

A wavelength independent quantum yield is good evidence that the reaction is occurring from a thermally equilibrated excited state where 'memory' of the excess excitation energy is lost through vibrational relaxation prior to the process(es) leading to

substitution. This agrees with the emission data described above. For substitution to occur from a thermally relaxed MLCT excited state with negligible antibonding character, population of a higher lying dissociative LF state is most probably required (see discussion).

4.3 Electron Transfer

On the basis of the interpretation of wavelength dependence above, that photosubstitution occurs via population of a reactive LF state from a thermally relaxed MLCT state, it was hypothesized that the quantum yield for the photoinduced electron transfer reaction in chloroform should also be wavelength independent. If the MLCT state is thermally relaxed prior to electron transfer, there should be no dependence on irradiation wavelength.

The UV-visible spectral changes for the electron transfer reaction

$$Mo(CNPh)_6 \xrightarrow{h\nu,\ CHCl_3} [Mo(CNPh)_6Cl]^+$$

are shown in Figure 4.3. The presence of an isosbestic point confirms that a single Mo product is formed. The dependence of ϕ_{et} on excitation energy is shown in Figure 4.4.

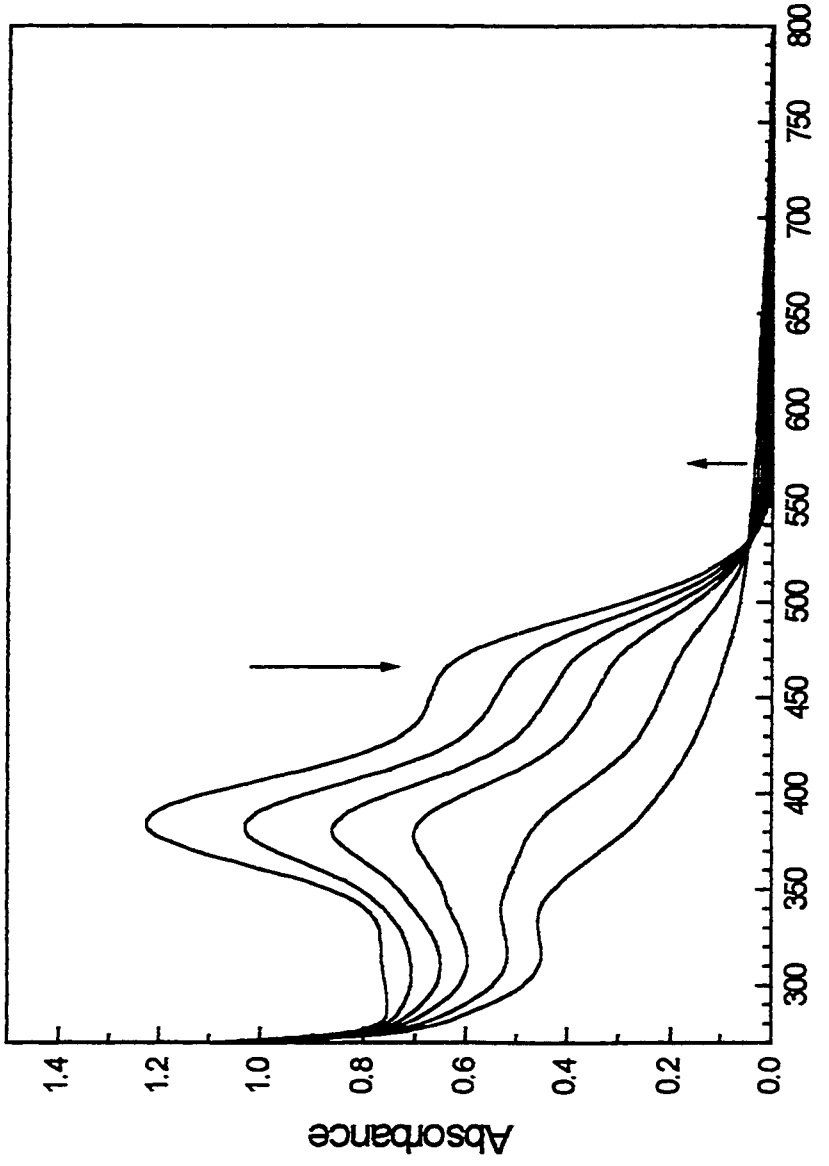

Figure 4.3 Spectral changes for the irradiation of $Mo(CNPh)_6$ in chloroform. $[Mo(CNPh)_6] = 1.1 \times 10^{-5}$ M.

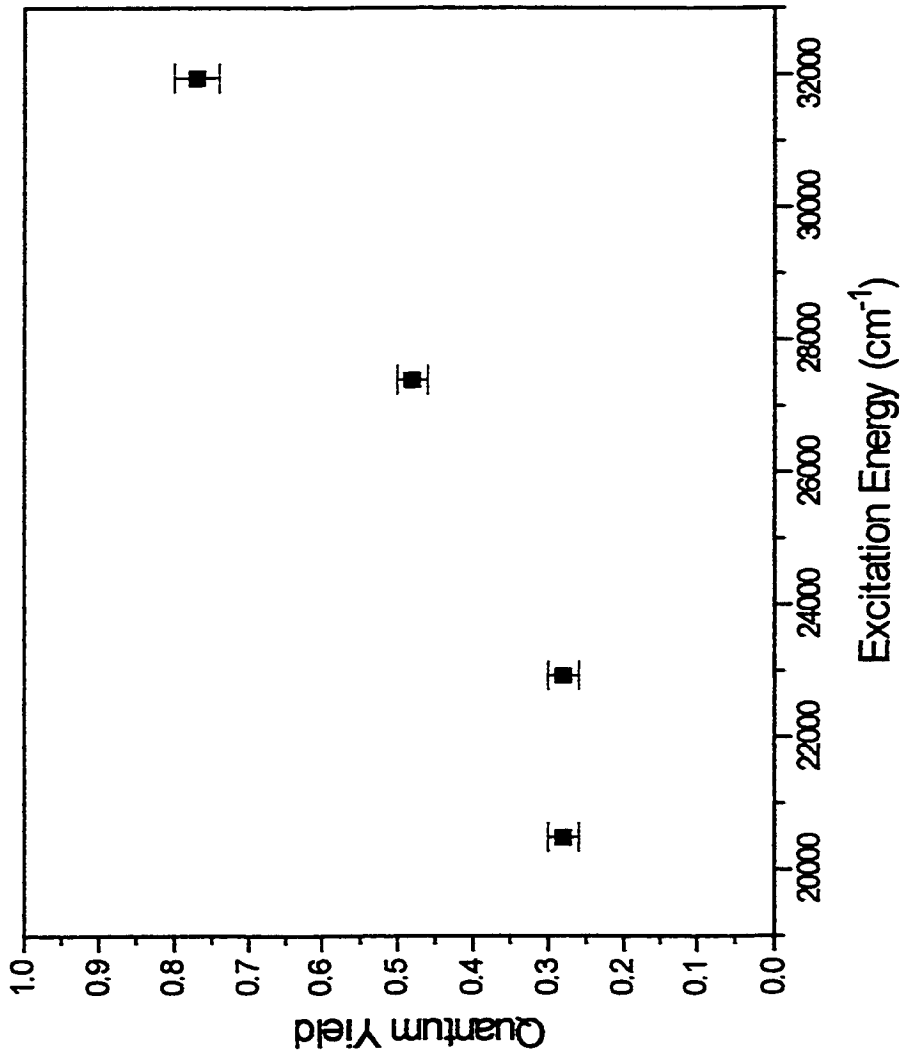

Figure 4.4 Excitation energy dependence of electron transfer quantum yield for $Mo(CNPh)_6$ in chloroform. Error bars represent standard deviation.

From Figure 4.4, there are two regions of wavelength dependence. At high excitation energies (corresponding to 313 and 365 nm) ϕ_{et} decreases with decreasing excitation energy. At low excitation energies (corresponding to 436 and 488 nm) ϕ_{et} has approached a limit and is no longer dependent on excitation energy.

Figure 4.5 provides a framework for understanding this result. First, the lowest lying MLCT state lies 17900 cm^{-1} above the zeroth vibrational level of the ground state.[78] The MLCT manifold of states extends much higher, to approximately 30000 cm^{-1} (a $d\pi \rightarrow \pi_v^*$ absorption at 26500 cm^{-1} and a $d\pi \rightarrow \pi_h^*$ absorption at 31950 cm^{-1} are the two highest energy MLCT absorptions). Thus, all irradiation wavelengths directly populate MLCT states.

The half wave potential $E_{1/2}$ for oxidation of $Mo(CNPh)_6$ is -0.19 V (vs. SCE).[89] The $E_{1/2}$ for the one electron reduction of chloroform is -1.67 V (vs. SCE).[90] From these $E_{1/2}$'s it is possible to calculate the relative energy of the primary electron transfer products $Mo(CNPh)_6^+ + CHCl_3^{\cdot-}$. Using the equation $\Delta G = -nFE$ (F = Faraday's constant, n = number of moles of electrons transferred) and converting to wavenumbers, the products are 13060 cm^{-1} above the ground state of $Mo(CNPh)_6$.

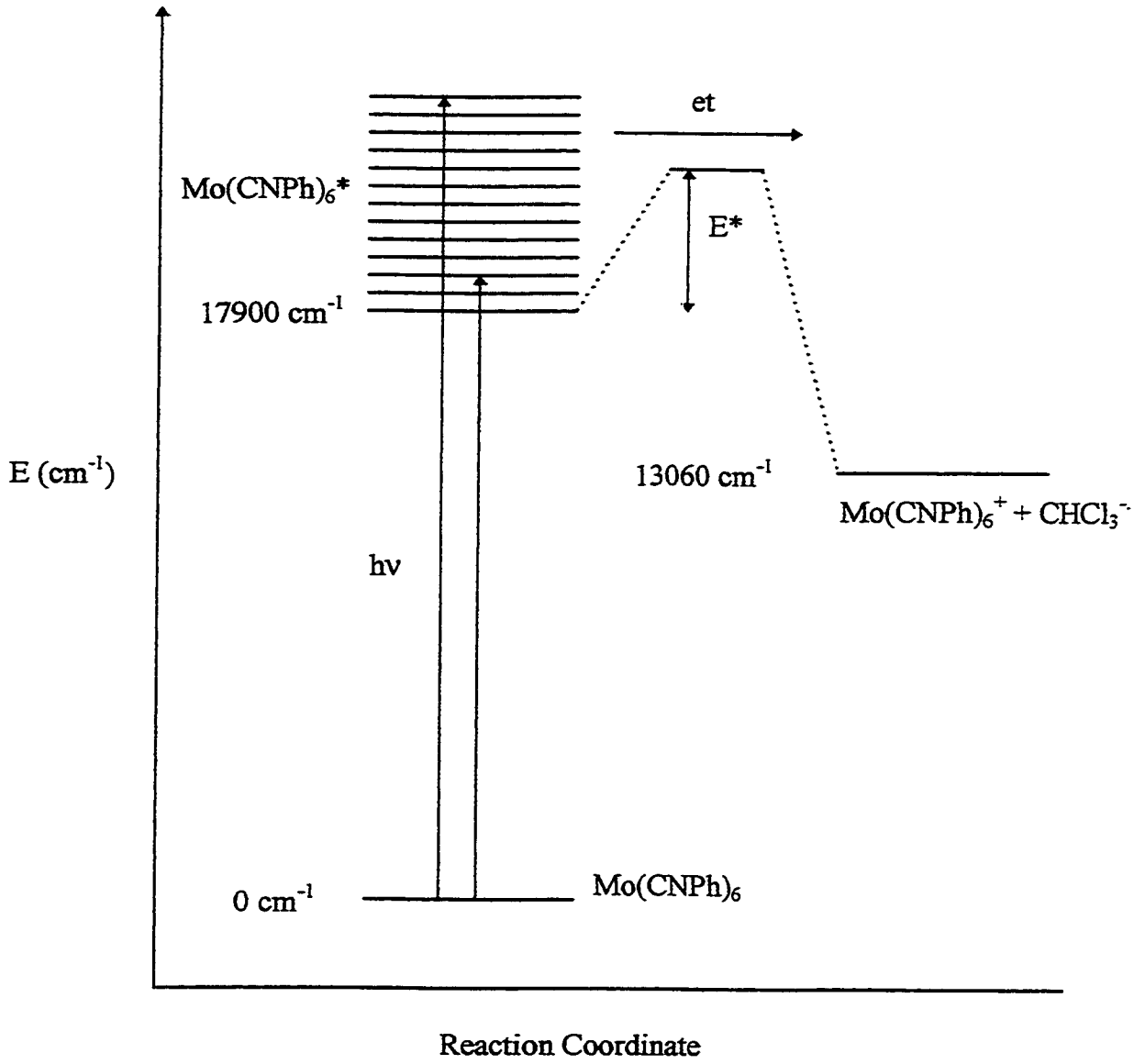

Figure 4.5 Hot electron transfer in $Mo(CNPh)_6$. When the photon energy exceeds the total activation energy (17900 cm^{-1} + E*), electron transfer may occur prior vibrational relaxation, leading to a larger ϕ_{et} than if the system cools first.

This electron transfer reaction is most likely in the "normal region" - where there is a classical activation energy requirement for the electron transfer to take place. If the excitation energy contained in a photon results in population of MLCT states that lie below this activation energy, the system may undergo vibrational relaxation prior to electron transfer to the solvent (chloroform) - thereby losing 'memory' of excess excitation energy and leading to wavelength independence. Alternatively, if the excitation energy is sufficient to populate MLCT states at or above the energy barrier to electron transfer, an excitation energy dependence may result: the higher the excess energy, the greater the probability that the system will undergo electron transfer prior to vibrational relaxation and trapping in the lower levels of the MLCT manifold. In other words, at shorter wavelengths, 'hot' electron transfer is possible.

4.4 Nanosecond Flash Photolysis

Preliminary flash photolysis experiments were performed on $Mo(CNPh)_6$ in pyridine to further explore the possibility of an associative photosubstitution mechanism. Figure 4.6 shows the increase in $Mo(CNPh)_5py$ absorption at 550 nm following a 532 nm flash. The product is formed completely within the 20 ns flash.

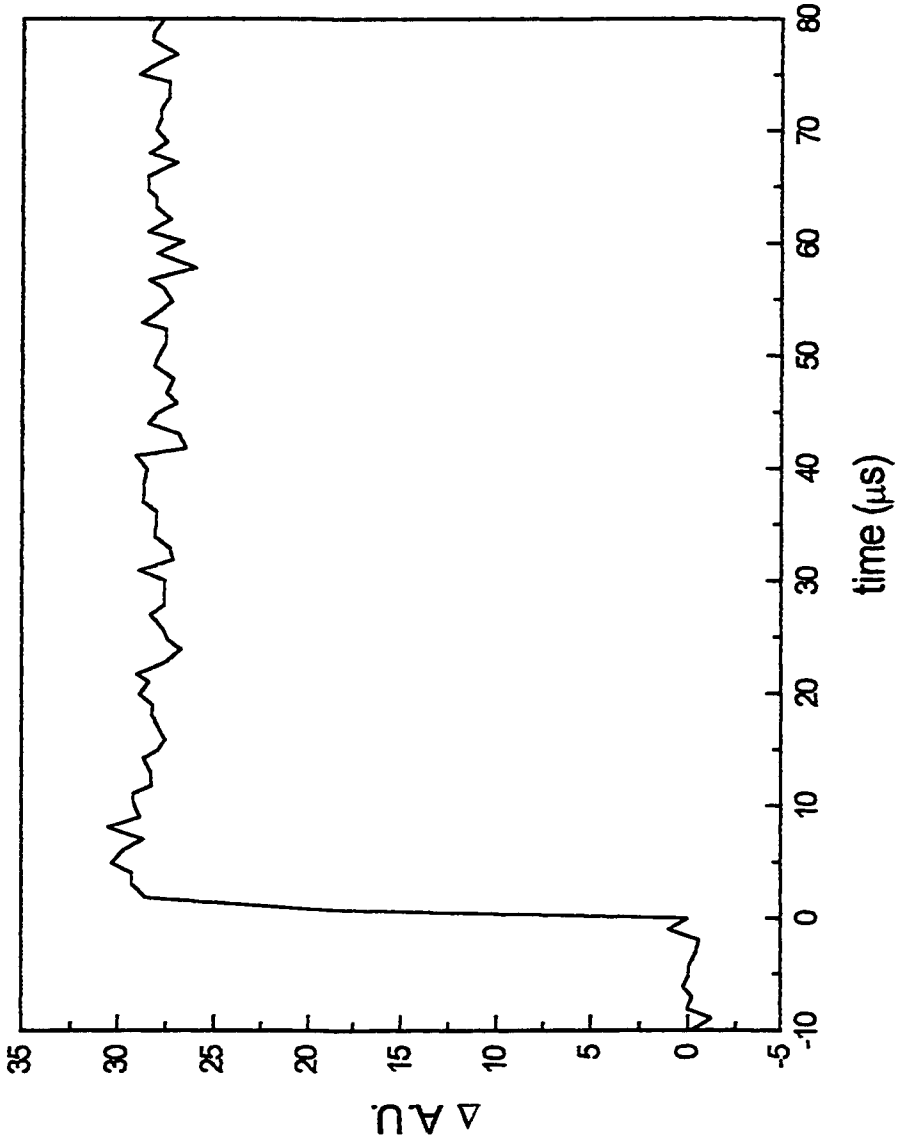

Figure 4.6 Nanosecond flash photolysis of $Mo(CNPh)_6$ in neat pyridine: kinetic trace monitoring the relative absorbance of the product at 550 nm.

By setting the monitoring wavelength to the isosbestic point of the reaction (506 nm), the presence of any intermediate different from $Mo(CNPh)_6$ and the product $Mo(CNPh)_5py$, for example a seven-coordinate intermediate "$Mo(CNPh)_6py$", would be detected. In this experiment, no change from zero absorption change was observed, suggesting that there is no such intermediate on this time scale.

Considering the 21 ns fluorescence lifetime, these observations are not surprising since primary photochemical processes must occur prior to excited state decay. However, a meta-stable intermediate of any kind with a sub-microsecond lifetime is not observed in this system. Time resolved studies on $Mo(CNPh)_6$ on the picosecond time scale are likely to provide more useful information.

4.5 Discussion

One purpose of this investigation into $Mo(CNPh)_6$ photochemistry was to gain insight into the complex photochemistry of $Cr(CNPh)_6$ by comparison. The differences between $Cr(CNPh)_6$ and $Mo(CNPh)_6$ photochemistry were initially thought to be much larger in light of the earlier suggestion that $Mo(CNPh)_6$ undergoes associative photosubstitution.[61] While that proposal has now been shown to be incorrect, the differences between $Cr(CNPh)_6$ and $Mo(CNPh)_6$ photochemistry remain non-trivial.

The only difference between $Cr(CNPh)_6$ and $Mo(CNPh)_6$ is the central metal atom. The complexes are isoelectronic and share almost identical electronic absorption properties. Due to the greater ligand field strength of second row transition metals, it is expected that the Mo complex should have stronger metal-ligand bonds and higher energy antibonding ligand field states than $Cr(CNPh)_6$. These features must then be responsible for the differences in photochemistry.

The mechanism for photosubstitution at Mo is likely to be thermal population of higher lying antibonding LF states from a thermally relaxed MLCT excited state. Since antibonding LF states are at higher relative energy in $Mo(CNPh)_6$ than in $Cr(CNPh)_6$, the system is more likely to thermally relax into the MLCT excited state than to promptly cross into an LF state that leads to dissociation. Such prompt internal conversion is responsible for the ultrafast ligand dissociation via the charge neutral, high excitation energy mechanism in $Cr(CNPh)_6$ and probably $M(CO)_6$ {M = Cr, Mo, W} as well.[11] Figure 4.7 shows an excited state model for $Mo(CNPh)_6$. This can be compared with Figure 3.26 for $Cr(CNPh)_6$.

There is no evidence for a second substitution pathway in $Mo(CNPh)_6$. The electron transfer mediated, low energy excitation substitution pathway in $Cr(CNPh)_6$ is unique. The smaller ligand field stabilization energy (LFSE) in the chromium complex may hold

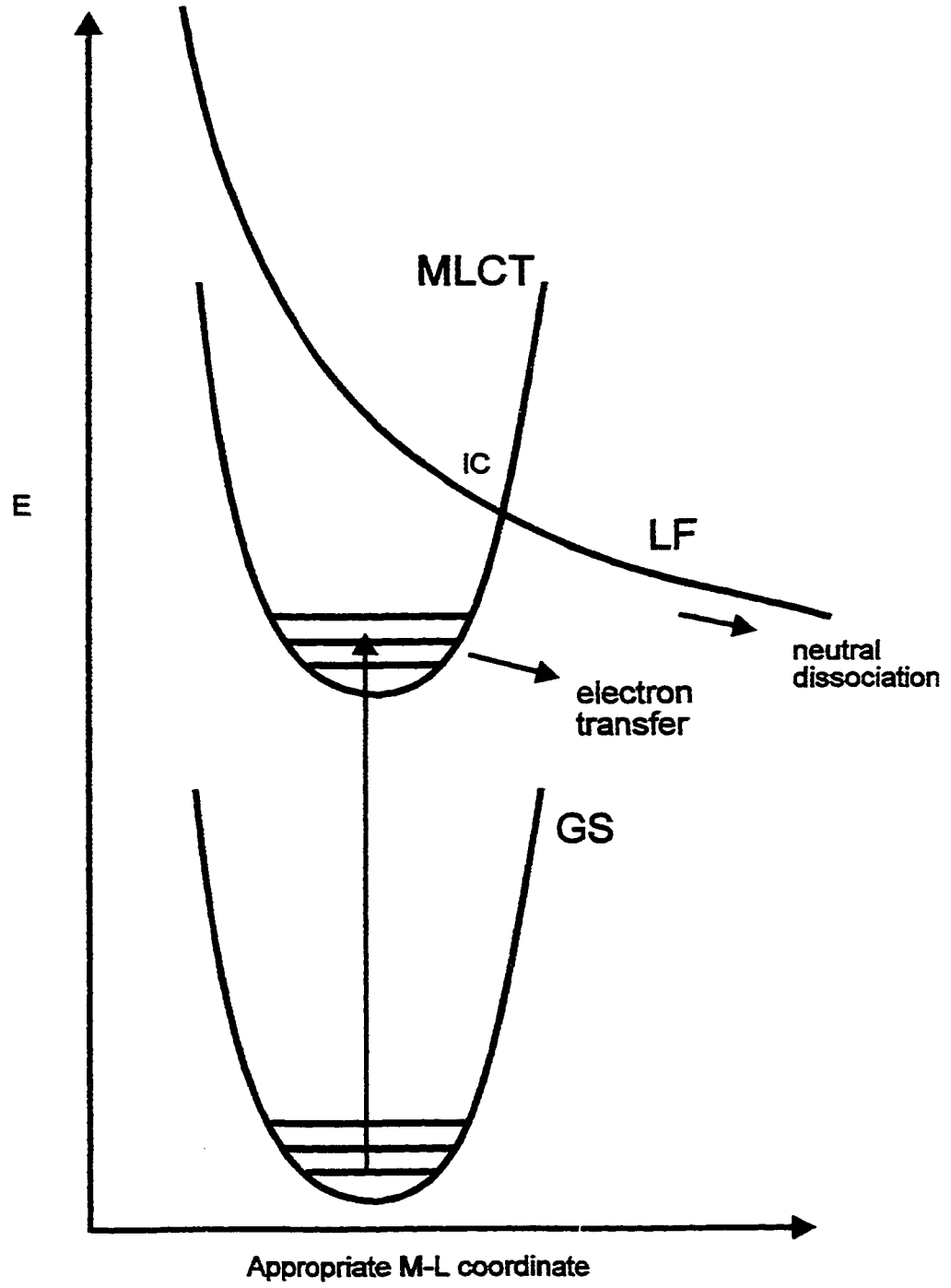

Figure 4.7 Excited state diagram of $Mo(CNPh)_6$. The MLCT state is responsible for electron transfer reactivity. A higher lying ligand field state is responsible for the dissociation of a neutral PhNC ligand.

the answer. It is known from resonance Raman data that the low energy MLCT state in $Cr(CNPh)_6$ is associated with molecular distortions.[57] Such distortions may decrease the LFSE further. If the LFSE drops below the spin pairing energy (SPE), the MLCT state may undergo a dramatic change in spin state at the metal centre. In the MLCT state, chromium is formally in the +1 oxidation state (d^5). A "spin flip" could populate antibonding LF states according to Figure 4.8.

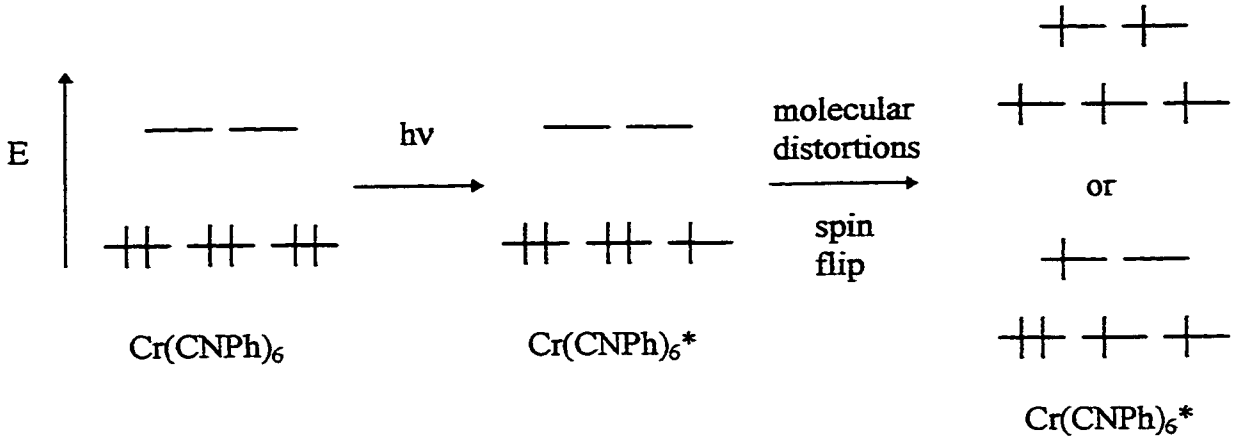

Figure 4.8 Configuration of metal centred d orbitals of $Cr(CNPh)_6$ on going from ground state to MLCT excited state, followed by distortions that make LFSE < SPE, resulting in a spin flip. For clarity, the effects of Jahn-Teller distortions are not included

Such a mechanism is purely speculative and examples of similar behaviour are rare and in one case similarly speculative. In the self exchange electron transfer reaction of $Co(NH_3)_6^{2/3+}$, the rate is significantly lower than in the ruthenium analogue.[91] It has been suggested that a spin state change is required for electron transfer in Co(II).[92] For example, electron transfer may be facilitated on going from the configuration $t_{2g}^5e_g^2$

(high spin d^7) to $t_{2g}^6 e_g^1$ (low spin). Since Co(II) is high spin d^7, a spin flip to low spin is required for electron transfer. The ruthenium(II) analogue is low spin d^7, and does not require a change in spin state for electron transfer to occur.

While electron transfer in $Cr(CNPh)_6$ is intimately related to a substitution pathway, the mechanism is different in the case of $Mo(CNPh)_6$. In $Mo(CNPh)_6$, the MLCT states are relatively long lived when compared to $Cr(CNPh)_6$ and electron transfer occurs from these states. The wavelength dependence of electron transfer has been interpreted above. The apparent 'hot' electron transfer is of fundamental and practical interest. Hot electron transfer is potentially important in solar energy conversion and photocatalysis, where it is important to maximize the conversion of photon energy into a chemical process (typically an electron transfer). These experiments on $Mo(CNPh)_6$ appear to have provided the first direct observation of a homogeneous photoinduced 'hot' electron transfer. An indirect example was provided when photoinduced 'hot' electron transfer was invoked to reconcile energy requirements with observed reactivity in $W(CO)_4$phen.[93] Examples of heterogeneous 'hot' electron transfer have been suggested[94,95] and are a current research area which can be informed by homogeneous examples.

The quantum yields for electron transfer found in this work are significantly higher than previously reported. It should be noted that the 436 nm ϕ_{et} in the tungsten complex

$W(CNPh)_6$ was reported as 0.28, the same as found here for $Mo(CNPh)_6$ at this wavelength. The difference in $Mo(CNPh)_6$ results may have its origin in the method of monitoring the progress of reaction. In this work, ϕ_{et} was determined by monitoring the decrease in $Mo(CNPh)_6$ absorption at 520 nm. Mann[78] monitored the very small absorption increase found in the 600 nm region (Figure 4.3). Small absorbance measurements are often associated with errors. It is also possible that quenching impurities were present in samples used in the previous work. These measurements are very sensitive to the purity of the chloroform that is used.

4.6 Future Work

To better understand $Mo(CNPh)_6$ photochemistry, picosecond or femtosecond time resolved spectroscopy would be useful. Such time resolution could pin down the exact time scale of photosubstitution. The nucleophile concentration dependence described in section 4.2.2 suggests that it occurs much faster than the 21 ns lifetime of the excited state. In this respect, it might be like the wavelength independent reaction of $Cr(CO)_6$ which provided 'classic' evidence[24] for reaction from a vibrationally relaxed triplet until femtosecond spectroscopy showed the reaction occurred in less that 300 fs.[11] It may also be possible to measure the rate of excited state electron transfer to the solvent. The fundamental interest in hot electron transfer processes would make such a study valuable.

CHAPTER FIVE: PHOTOSUBSTITUTION IN *cis*-$Ru(bpy)_2(py)_2^{2+}$

5.1 Introduction

Ruthenium (II) polypyridyl complexes make up a large class of compounds with low lying MLCT states. Generally, they have been studied for their photoinduced electron transfer reactions, acting as electron donors and acceptors. Photosubstitution in Ru(II) polypyridyl complexes is not a desirable reaction mode because it competes with electron transfer and also destroys the original complex.[96] Typically, photosubstitution in this class of compounds is studied to learn how to avoid it.

A compound used to model the photosubstitution of $Ru(bpy)_3^{2+}$ is *cis*-$Ru(bpy)_2(py)_2^{2+}$. The general photosubstitution reaction is[62]:

$$cis\text{-}Ru(bpy)_2(py)_2^{2+} + L \xrightarrow{h\nu} cis\text{-}Ru(bpy)_2(py)(L)^{2+}$$

where L is either a neutral nucleophile or a coordinating anion. Secondary photosubstitution of the remaining pyridine ligand can occur if L is a sufficiently strong field ligand.[97]

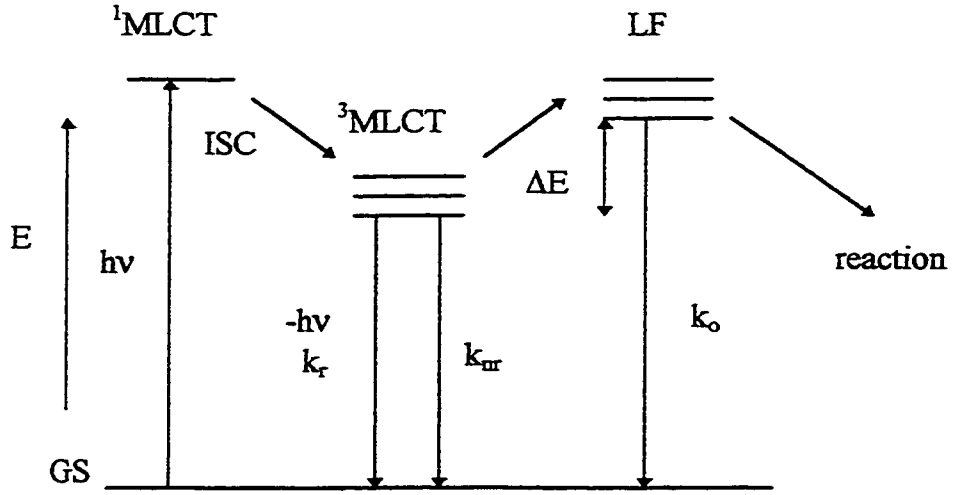

Figure 5.1 Excited state diagram and relevant photophysical quantities for $Ru(bpy)_3^{2+}$ and $Ru(bpy)_2(py)_2^{2+}$. Taken from reference 62.

The excited states of *cis*-$Ru(bpy)_2(py)_2^{2+}$ and $Ru(bpy)_3^{2+}$ have been described according to Figure 5.1.[62] Initial population of the ^{1}MLCT is followed by rapid, efficient ($\phi_{ISC} = 1$) intersystem crossing to ^{3}MLCT, which can lead to emission. In $Ru(bpy)_3^{2+}$, the ^{3}MLCT state is responsible for electron transfer reactions. A LF state at energy ΔE higher than ^{3}MLCT, thermally populated, is responsible for photosubstitution. Both ^{3}MLCT and LF states can decay through non-radiative processes. From the temperature dependence of emission intensity or lifetime, the quantities ΔE, $(k_r + k_{nr})$, and k_o from Figure 5.1 can be evaluated. These quantities are given in Table 5.1 for *cis*-$Ru(bpy)_2(py)_2^{2+}$ and

$Ru(bpy)_3^{2+}$. Note that ΔE is much smaller for *cis*-$Ru(bpy)_2(py)_2^{2+}$, in keeping with its lower ligand field strength.

Table 5.1 Comparison of photophysical data for $Ru(bpy)_2(py)_2^{2+}$ and $Ru(bpy)_3^{2+}$.

Compound	ΔE (cm^{-1})[a]	$(k_r + k_{nr})$[a]	k_o[a]	E_{em} (cm^{-1})[b]	E_{em} (cm^{-1}) (0-0)[b]
$Ru(bpy)_3^{2+}$	3859[c] 3951[d]	3.9×10^5	1.9×10^{14}	16580	16600
$Ru(bpy)_2(py)_2^{2+}$	2758[c] 1957[d]	4.23×10^5	2.34×10^{14}	16530[e]	16600[e]

[a] Determined from non-linear fits of the temperature dependence of emission (based on the expression describing lifetimes or intensity of emission: e.g. for lifetime data, $1/\tau = k_r + k_{nr} + k_o\exp(-\Delta E/RT)$). Taken from reference 62. [b] CH_2Cl_2 solution at 200 K. Taken from reference 98. [c] Determined from emission lifetimes. [d] Determined from emission intensities. [e] Questions have been raised about the presence of $Ru(bpy)_3^{2+}$ impurities in the samples of $Ru(bpy)_2(py)_2^{2+}$ used in this reference[62], leading to erroneous luminescence meaurements for that complex.

There are several features of *cis*-$Ru(bpy)_2(py)_2^{2+}$ that suggest that the photosubstitution reaction may occur on the ultrafast time scale:

1) *cis*-$Ru(bpy)_2(py)_2^{2+}$ does not luminesce at temperatures above 230 K, indicating possible absence of a bound excited state at these temperatures. The lack of observable emission means that the efficiency for population of the LF state, ϕ_{LF}, is near unity.[62]

2) The photosubstitution yield is not affected by O_2 quenching in CH_2Cl_2. From the O_2 concentration, the lifetime of the reactive LF state was estimated to be less than 100 ps.[99]

3) The photosubstitution quantum yield (ϕ_{sub}) is essentially independent of temperature.[99,100] The activation energy for ϕ_{sub}, determined from the temperature dependence, was estimated at 700 cm^{-1}. This is associated with a large error. Another group has reported that the activation energy is not detectable. Only a small barrier, if any, is associated with the reaction for temperatures above 250 K.

If the photodissociation of pyridine is an ultrafast process, the classical cage effect is expected to manifest itself in the wavelength dependence of ϕ_{sub}. The wavelength dependence of photosubstitution in *cis*-$Ru(bpy)_2(py)_2^{2+}$ was investigated in order to test this hypothesis.

5.2 Results

The photosubstitution of $Ru(bpy)_2(py)_2^{2+}$ was performed in acetone under nitrogen. With acetone (a weak field ligand) acting as the entering nucleophile, complications due to secondary photolysis are avoided. The hexafluorophosphate salt of $Ru(bpy)_2(py)_2^{2+}$ was used because PF_6^- is a non-coordinating anion. The spectral changes for the photosubstitution are shown in Figure 5.2.

Table 5.2 Wavelength Dependence of Photosubstitution Quantum Yields in $Ru(bpy)_2(py)_2^{2+}$

Wavelength (nm)	Quantum yield*
365	0.09
436	0.11
488	0.10

*All quantum yields are ± 0.01

The wavelength dependence of ϕ_{sub} is given in Table 5.2. Within experimental error, ϕ_{sub} is independent of irradiation wavelength. The absence of wavelength dependence suggests that the reactive LF excited state is thermally equilibrated with the surrounding solvent. That is, memory of excess excitation energy is lost by the time the dissociation

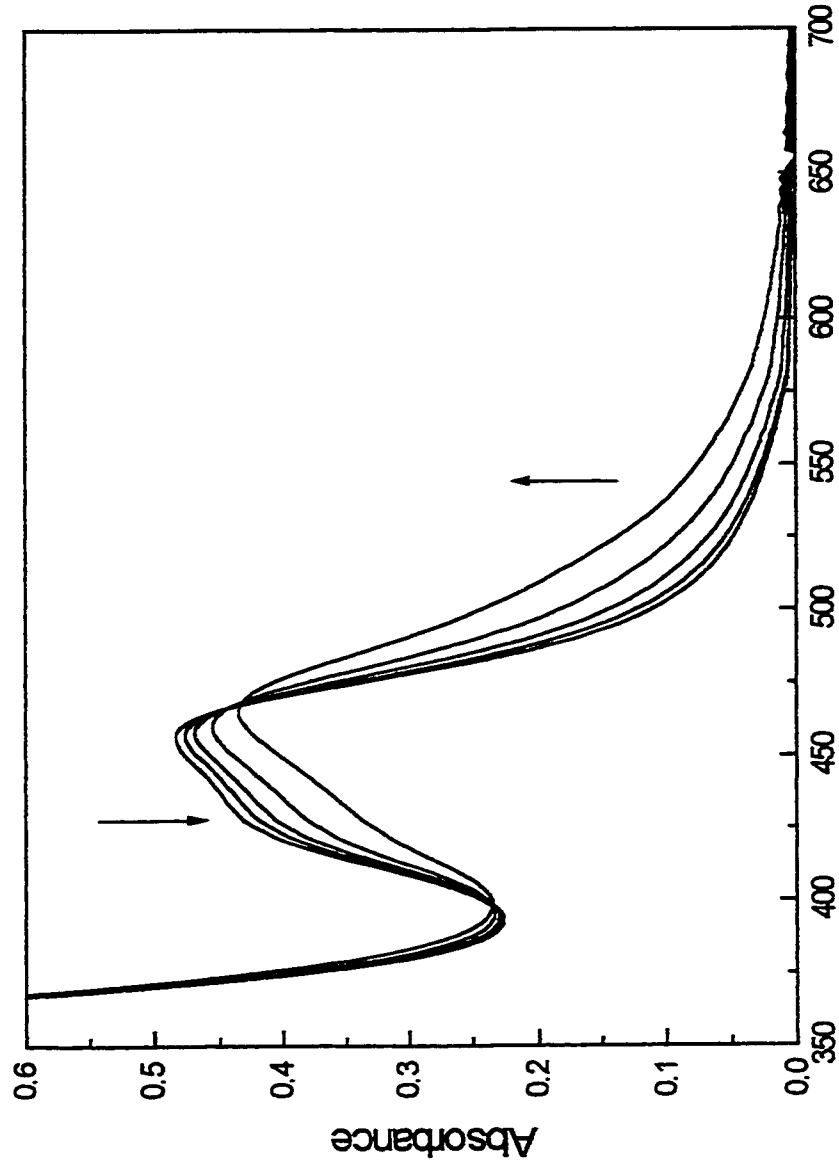

Figure 5.2 Absorbance changes for 365 nm photolysis of *cis*-$Ru(bpy)_2(py)_2^{2+}$ in acetone. Irradiation times are 0, 30, 120, 300, and 780 seconds. Arrows indicate the direction of absorbance changes. $[Ru(bpy)_2(py)_2^{2+}] = 5.9 \times 10^{-5}$ M.

occurs, and no wavelength dependence is observed. It also implies that the photochemical reaction always occurs from the same low lying LF excited state, regardless of the initial excitation energy.

5.3 Discussion

The primary photodissociation step in $Ru(bpy)_2(py)_2^{2+}$ is not likely to fall into the ultrafast (< 1 ps) time scale, given the wavelength dependence above. However, the temperature dependence of ϕ_{sub} and the lack of emission at room temperature indicate that population of the reactive state is extremely efficient and that the dissociation is almost barrierless - features expected in ultrafast reactions.

The maximum lifetime of the reactive state has been estimated at 100 ps. The lifetimes of solvent thermal cages are 0.1 -100 ps. It is possible that the dissociation occurs on a similar time scale to thermal equilibration with the solvent. This would mask the expected results of the classical cage effect (i.e. decrease in ϕ_{sub} with decreasing excitation energy) because excess excitation energy is distributed to the solvent prior to ligand dissociation.

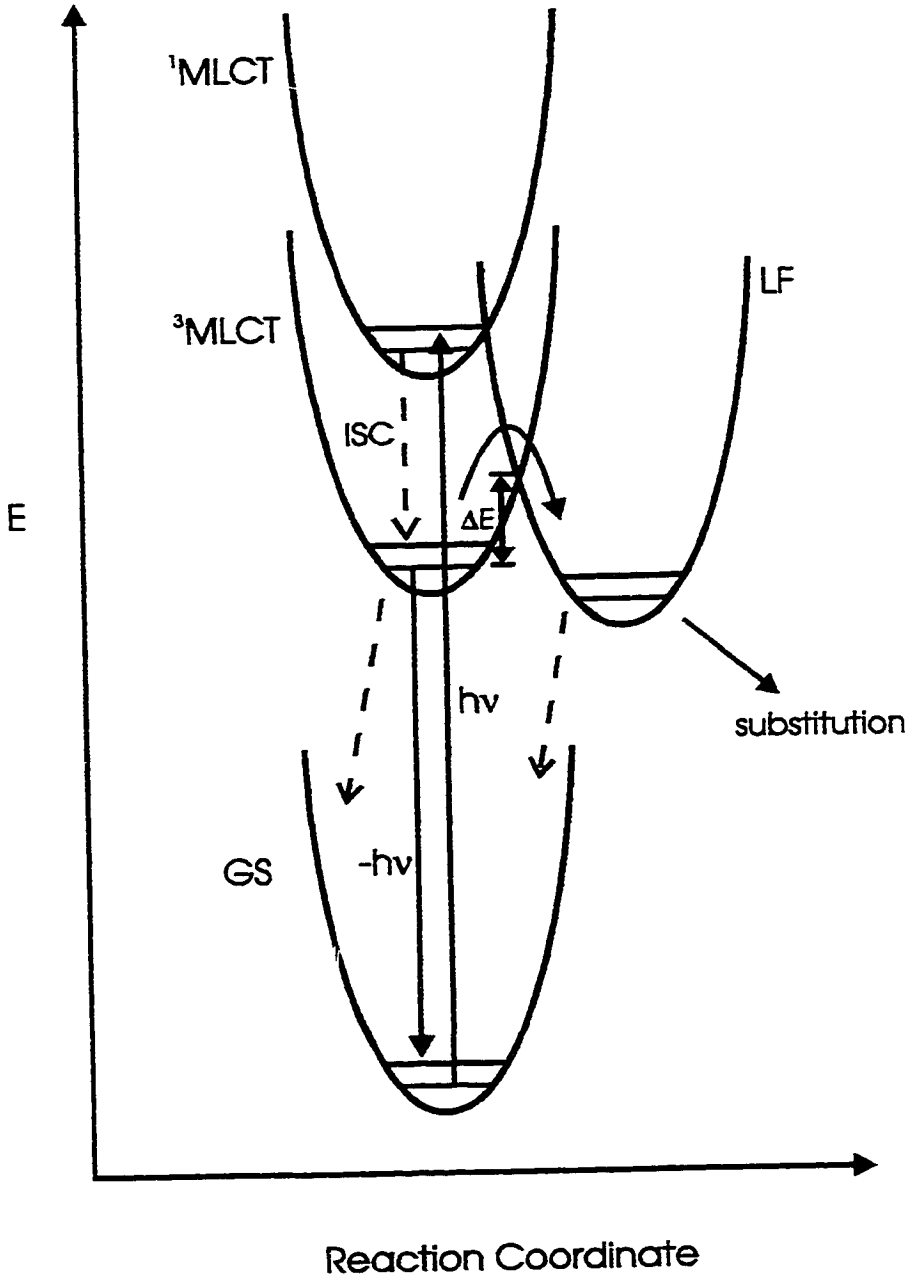

Figure 5.3 Excited state diagram for $Ru(bpy)_2(py)_2^{2+}$. Dashed lines indicate non-radiative decay. The dashed line labelled ISC refers to intersystem crossing from ^{1}MLCT $\rightarrow$ ^{3}MLCT. Recrossing from LF $\rightarrow$ ^{3}MLCT is omitted for clarity.

Figure 5.3 shows the same excited states as in Figure 5.1, except with representations of the potential surfaces. The energy ΔE between ^{3}MLCT and LF states is more accurately described as an activation energy, not the energy difference between the zeroth vibrational levels of these two states, as implied in Figure 5.1. Crossing and recrossing between thermally equilibrated ^{3}MLCT and LF states is unlikely at room temperature since $\Delta E >> kT$ ($kT = 207$ cm^{-1} at 298 K). Therefore, population of the LF state must occur prior to thermal equilibration. This is not surprising because the system has more than sufficient excess energy immediately after electronic excitation to move the system over the ΔE energy barrier. At 298 K, most of the thermal equilibration would occur after ^{3}MLCT $\rightarrow$ LF intersystem crossing. Thermal equilibration of the LF state may be faster than ligand dissociation because of a relatively shallow LF potential energy surface, unlike the cases of $Mn_2(CO)_{10}$ and $MnCl(CO)_5$ where the LF energy drops rapidly with increasing bond length.[83-85] There is also the possibility that other trap states may affect the times for thermal equilibration.

It is possible that excitation into the MLCT absorption envelope leads to population of states that are above the energy of the MLCT $\rightarrow$ LF crossing. From energetics, this explanation is plausible. The energy of the ^{3}MLCT state has been estimated at 16600 cm^{-1} above the ground state (Table 5.1) and the maximum energy barrier for ^{3}MLCT $\rightarrow$ LF crossing is 2758 cm^{-1}. These add to 19358 cm^{-1} above the ground state. The lowest

excitation energy used here is 20492 cm^{-1} (488 nm), 1134 cm^{-1} above the estimated energy barrier for $^3MLCT \rightarrow LF$ crossing.

It should be noted that the ΔE values for $Ru(bpy)_2(py)_2^{2+}$ in Table 5.1 could be subject to the same error suggested for the reported emission energy.[62] $Ru(bpy)_3^{2+}$ impurities may have skewed the temperature dependent emission lifetime and intensity measurements, leading to the >30% difference in ΔE's determined the two different ways. This is in contrast to the corresponding values for $Ru(bpy)_3^{2+}$, where the two determination methods yielded very similar results.

Table 5.3 Solvent Effects on Photosubstitution in $Ru(bpy)_2(py)_2^{2+}$ at 436 nm

Solvent	Quantum yield
CH_2Cl_2 [a]	0.20 [b]
1 M H_2SO_4	0.26 [b]
CH_3CN	0.036 [c]
H_2O	0.17 [c]
$(CH_3)CO$	0.11[d]

[a] In the presence of excess tetrabutylammonium chloride, taken from reference 99. [b] Taken from reference 101. [c] Taken from reference 99. [d] This work.

The $Ru(bpy)_2(py)_2^{2+}$ system appears to lie somewhere between the ultrafast photochemical regime and the more classical photochemistry of long lived thermally

equilibrated excited states. However, picosecond or femtosecond absorption spectroscopy are necessary to determine the exact time scale of the primary photochemical events. If the photodissociation of pyridine occurs on the time scale of thermal cage lifetimes, this may be a good model for the study of solvent effects, perhaps based on thermal conductivity. Indeed, significant variations in ϕ_{sub} with solvent have been observed (Table 5.3), although there appears to be no immediate correlation with thermal conductivity, dielectric relaxation time, or viscosity.

CONCLUDING REMARKS:

The wavelength dependent photochemistry of three d^6 metal complexes having low-lying MLCT excited states was investigated. In Chapter Three, it was shown that $Cr(CNPh)_6$ has wavelength dependent substitution and electron transfer photochemistry, and that the mechanisms of these processes are also wavelength dependent. Chapter Four dealt with $Mo(CNPh)_6$, which exhibits photochemistry that contrasts strongly with the intricate mechanisms of the chromium analogue. Chapter Five investigated the photosubstitution of *cis*-$Ru(bpy)_2py_2^{2+}$. In the phenylisocyanide complexes, wavelength dependence revealed much about mechanism and provided evidence for a new electron transfer mediated substitution pathway and the 'hot' electron transfer phenomenon. Wavelength dependence in the ruthenium system provides a problem for future study: Why should an ultrafast or semi-ultrafast reaction exhibit no wavelength dependence in spite of the classical cage effect? This behaviour is similar to $Cr(CO)_6$, where there is a wavelength independent substitution quantum yield and CO photodissociation is known to occur in less than 300 fs.

Wavelength dependence is an important tool in the study of photochemical mechanisms The examples above demonstrate the diversity of photochemical behaviour that can be unraveled.

BIBLIOGRAPHY:

1. Liu, Q.; Wang, J.; Zewail, A.H. *J. Phys. Chem.* 1995, **99**, 11321.

2. Garraway, B.; Stenholm, S.; Suominen, K-A. *Physics World* 1993, **4**, 43.

3. Pulgiano, N.; Gnanakoran, S.; Hochstrasser, R.M. *J. Photochem. Photobiol. A: Chem.* 1996, **102**, 21.

4. Rapinec, S.T.; Sension, R.J.; Szarka, A.Z.; Hochstrasser, R.M. *J. Phys. Chem.* 1991, **95**, 10380.

5. Schoenlien, R.W.; Peteanu, L.A.; Mathies, R.A.; Shank, C.V. *Science* 1991, **254**, 412.

6. Wang, Q.; Schoenlein, R.W.; Peteanu, L.A.; Mathies, R.A.; Shank, C.V. *Science* 1994, **266**, 422.

7. Zhu, L.; Sage, J.T.; Champion, P.M. *Science* 1994, **266**, 629.

8. Pedersen, S.; Herek, J.L.; Zewail, A.H. *Science* 1994, **266**, 1359.

9. Simon, J.D.; Xie, X. *J. Phys. Chem.* 1987, **91**, 5538.

10. Joly, A.G.; Nelson, K.A. *J. Phys. Chem.* 1989, **93**, 2876.

11. Joly, A.G.; Nelson, K.A. *Chem. Phys.* 1991, **152**, 69.

12. Adamson, A.W. *J. Chem. Ed.* 1983, **60**, 797.

13. Roundhill, D.M. Photochemistry and Photophysics of Metal Complexes, Plenum Press: New York, 1994.

14. Turro, N.J. Modern Molecular Photochemistry, Benjamin/Cummings: Menlo Park, 1994.

15. Heller, E.J. *J. Chem. Phys.* 1975, **62**, 1544.

16. Lee, S-Y.; Heller, E.J. *J. Chem. Phys.* 1979, **71**, 4777.

17. Heller, E.J. *Acc. Chem. Res.* 1981, **14**, 368.

18. Yoo, C.S.; Zink, J.L. *Inorg. Chem.* 1983, **22**, 2474.

19. Tutt, L.; Zink, J.L. *J. Am. Chem. Soc.* 1986, **108**, 5830.

20. Zink, J.L.; Shin, K-S. K. *Adv. Photochem.* 1991, **16**, 119.

21. Hollebone, B.R. *Theoret. Chim. Acta (Berl.)* 1980, **56**, 45.

22. Hollebone, B.R.; Langford, C.H.; Serpone, N. *Coord. Chem. Rev.* 1981, **39**, 181.

23. Moralejo, C.; Langford, C.H.; Sharma, D.K. *Inorg. Chem.* 1989, **28**, 2205.

24. Nasielski, J.; Colas, A. *Inorg. Chem.* 1978, **17**, 237.

25. Moralejo, C.; Langford, C.H. *J. Photochem. Photobiol. A: Chem.* 1991, **59**, 285.

26. Franck, J.; Rabinowitch, E. *Trans. Faraday Soc.* 1934, **30**, 120.

27. Rabinowitch, E.; Wood, W.C. *Trans. Faraday Soc.* 1936, **32**, 1381.

28. Rabinowitch, E.; Wood, W.C. *Trans. Faraday Soc.* 1936, **32**, 1547.

29. Zimmerman, J.; Noyes, R.M. *J. Chem. Phys.* 1950, **18**, 658.

30. Lampe, F.W.; Noyes, R.M. *J. Am. Chem. Soc.* 1954, **76**, 2140.

31. Booth, D.; Noyes, R.M. *J. Am. Chem. Soc.* 1960, **82**, 1868.

32. Meadows, L.F.; Noyes, R.M. *J. Am. Chem. Soc.* 1960, **82**, 1872.

33. Langford, C.H.; Vuik, C.P.J. *J. Am. Chem. Soc.* 1976, **98**, 5409.

34. Vichova, J.; Hartl, F.; Vlcek, A., Jr. *J. Am. Chem. Soc.* 1992, **114**, 10903.

35. Rossenaar, B.D.; Kleverlaan, C.J.; Stufkens, D.J.; Oskam, A. *J. Chem. Soc. Chem. Commun.* 1994, 63.

36. Stufkens, D.J.; van Outersterp, J.W.M.; Oskam, A.; Rossenaar, B.D.; Stor, G.J. *Coord. Chem. Rev.* 1994, **132**, 147.

37. Langford, C.H.; Shaw, L.E. *Coord. Chem. Rev.* 1997, **159**, 221.

38. Laermer, F.; Elsaesser, T.; Kaiser, W. *Chem. Phys. Lett.* 1989, **156**, 381.

39. Elsaesser, T.; Kaiser, W. *Annu. Rev. Phys. Chem.* 1991, **42**, 83.

40. Johnson, F.P.A.; George, M.W.; Morrison, S.L.; Turner, J.J. *J. Chem. Soc. Chem. Commun.* 1995, 391.

41. Wilkins, R.G. Kinetics and Mechanism of Reactions of Transition Metal Complexes, VCH: New York, 1991.

42. Hynes, J.T. *Annu. Rev. Phys. Chem.* 1985, **36**, 573.

43. Kramers, H.A. *Physica* 1940, **7**, 284.

44. Kosower, E.M.; Huppert, D. *Chem. Phys. Lett.* 1983, **96**, 433.

45. Kosower, E.M.; Huppert, D. *Annu. Rev. Phys. Chem.* 1986, **37**, 127.

46. Hubbard, J.; Onsager, L. *J. Chem. Phys.* 1977, **67**, 4850.

47. Murov, S.L.; Carmichael, I.; Hug, G.L. Handbook of Photochemistry, 2nd. ed., Marcel Dekker: New York, 1993.

48. Bertolini, D.; Cassettari, M.; Salvetti, G. *J. Chem. Phys.* 1982, **76**, 3285.

49. Bertolini, D.; Cassettari, M.; Salvetti, G. *J. Chem. Phys.* 1983, **78**, 365.

50. Bottcher, C.J.F.; Bordewijk, P. Theory of Electric Polarization, Elsevier: New York, 1978.

51. Hill, N.E.; Vaughn, W.E.; Price, A.H.; Davies, M. Dielectric Properties and Molecular Behaviour, van Nostrand Reinhold: New York, 1969.

52. Jiminez, R.; Fleming, G.R.; Kumar, P.V.; Maroncelli, M. *Nature* 1994, **369**, 471.

53. Rejto, P.A.; Bindewald, E.; Chandler, D. *Nature* 1995, **375**, 129.

54. Strommen, D.P.; Nakamoto, K. *J. Chem. Ed.* 1977, **54**, 474.

55. Hirakawa, A.Y.; Tsuboi, M. *Science* 1975, **188**, 359.

56. Vitale, M.; Lee, K.K.; Hemann, C.F.; Hille, R.; Gustafson, T.L.; Burston, B.E. *J. Am. Chem. Soc.* 1995, **117**, 2286.

57. Maskova, E.; Vlcek, A., Jr. *Inorg. Chim. Acta* 1996, **242**, 17.

58. Lindsay, E.; Vlcek, A., Jr.; Langford, C.H. *Inorg. Chem.* 1993, **32**, 2269.

59. Geoffroy, G.L.; Wrighton, M.S. Organometallic Photochemistry, Academic Press: New York, 1979.

60. Xie, X.; Simon, J.D. *J. Phys. Chem.* 1989, **93**, 4401.

61. Mann, K.R.; Gray, H.B.; Hammond, G.S. *J. Am. Chem. Soc.* 1977, **99**, 306.

62. Wacholtz, W.M.; Auerbach, R.A.; Schmehl, R.H.; Ollino, M.; Cherry, W.R. *Inorg. Chem.* 1985, **24**, 1758.

63. Weber, W.P.; Gokel, G.W.; Ugi, I.K. *Angew. Chem. Int. Ed.* 1972, **11**, 530.

64. Cowan, J.A.; Sanders, J.K.M. *J. Chem. Soc. Perkin Trans. I* 1985, 2435.

65. Nagata, T. *Bull. Chem. Soc. Jpn.* 1991, **64**, 3005.

66. Wiederrecht, G.P.; Niemczyk, M.P.; Svec, W.A.; Wasielewski, M.R. *J. Am. Chem. Soc.* 1996, **118**, 81.

67. Malatesta, L.; Sacco, A.; Ghielmi, S. *Gazz. Chim. Ital.* 1952, **82**, 516.

68. Bullock, J.P.; Mann, K.R. *Inorg. Chem.* 1989, **28**, 4006.

69. Brignole, A.B.; Cotton, F.A. *Inorg. Syn.* 1972, **13**, 87.

70. Mann, K.R.; Cimolino, M.; Geoffroy, G.L.; Hammond, G.S.; Orio, A.A.; Albertin, G.; Gray, H.B. *Inorg. Chim. Acta* 1976, **16**, 97.

71. Dwyer, F.P.; Goodwin, H.A.; Gyarfas, E.C. *Aust. J. Chem.* 1963, **16**, 544.

72. King, A. Inorganic Preparations, George Allen and Unwin: London, 1950.

73. Calvert, J.G.; Pitts, J.N. Photochemistry, John Wiley and Sons: New York, 1966.

74. Hatchard, C.G.; Parker, C.A. *Proc. R. Soc. London* 1956, **A235**, 518.

75. Wegner, E.E.; Adamson, A.W. *J. Am. Chem. Soc.* 1966, **88**, 394.

76. Heller, H.G.; Langan, J.R. *J. Chem. Soc. Perkin Trans. II* 1981, 341.

77. Liao, Y.; Bohne, C. *J. Phys. Chem.* 1996, **100**, 734.

78. Mann, K.R. *Ph.D. Thesis*, California Institute of Technology, 1977.

79. Johnston, R.F.; Cooper, J.C. *J. Mol. Struct. (Theochem)* 1991, **236**, 297.

80. Gray, H.B.; Beach, N.A. *J. Am. Chem. Soc.* 1963, **85**, 2922.

81. Bohling, D.A.; Evans, J.F.; Mann, K.R. *Inorg. Chem.* 1982, **21**, 3546.

82. Bard, A.J.; Faulkner, L.R. Electrochemical Methods: Fundamentals and Applications, John Wiley and Sons: New York, 1980.

83. Rosa, A.; Ricciardi, G.; Baerends, E.J.; Stufkens, D.J. *Inorg. Chem.* 1995, **34**, 3425.

84. Rosa, A.; Ricciardi, G.; Baerends, E.J.; Stufkens, D.J. *Inorg. Chem.* 1996, **35**, 2886.

85. Wilms, M.P.; Baerends, E.J.; Rosa, A.; Stufkens, D.J. *Inorg. Chem.* 1997, **36**, 1541.

86. Shriver, D.F.; Atkins, P.W.; Langford, C.H. Inorganic Chemistry, 2nd ed., W.H. Freeman: New York, 1990.

87. Morse, D.L.; Wrighton, M.S. *J. Am. Chem. Soc.* 1976, **98**, 3951.

88. Stufkens, D.J. *Comments Inorg. Chem.* 1992, **13**, 359.

89. Klendworth, D.D.; Welters, W.W.; Walton, R.A. *Organometallics* 1982, **1**, 336.

90. Mann, C.K.; Barnes, K.K. Electrochemical Reactions in Nonaqueous Systems, Marcel Dekker: New York, 1970.

91. Jordan, R.B. Reaction Mechanisms of Inorganic and Organometallic Systems, Oxford University Press: New York, 1991.

92. Binstead, R.A.; Beattie, J.K.; Dewey, T.G.; Turner, D.M. *J. Am. Chem. Soc.* 1980, **102**, 6442.

93. Lindsay, E.; Langford, C.H. *Inorg. Chem.* in press.

94. Kulmala, S.; Ala-Kleme, T.; Heikkila, L.; Vare, L. *J. Chem. Soc. Faraday Trans.* 1997, **93**, 3107.

95. Bard, A.J. et al. *J. Phys. Chem. (B)* 1998, **102**, 9806.

96. Durham, B.; Caspar, J.V.; Nagle, J.K.; Meyer, T.J. *J. Am. Chem. Soc.* 1982, **104**, 4803.

97. Durham, B.; Walsh, J.L.; Carter, C.L.; Meyer, T.J. *Inorg. Chem.* 1980, **19**, 860.

98. Caspar, J.V.; Meyer, T.J. *Inorg. Chem.* 1983, **22**, 2444.

99. Henderson, L.J.; Cherry, W.L. *Chem. Phys. Lett.* 1985, **114**, 553.

100. Pinnick, D.V.; Durham, B. *Inorg. Chem.* 1984, **23**, 3841.

101. Pinnick, D.V.; Durham, B. *Inorg. Chem.* 1984, **23**, 1440.

102. Kirk, A.D.; Kneeland, D.M. *Inorg. Chem.* 1989, **28**, 7274.

103. Jones, W.D.; Feher, F.J. *J. Am. Chem. Soc.* 1984, **106**, 1650.

104. Hoyano, J.K.; Graham, W.A.G. *J. Am. Chem. Soc.* 1982, **104**, 3723.

105. Janowicz, A.H.; Bergman, R.G. *J. Am. Chem. Soc.* 1983, **105**, 3929.

106. Wrighton, M.; Hammond, G.S.; Gray, H.B. *Mol. Photochem.* 1973, **5**, 179.

APPENDIX A: EXCITATION ENERGY DEPENDENCE OF COMPETITIVE PHOTOSOLVATION IN $W(CO)_5py$

Introduction:

While competition studies are commonly used in the study of thermal reaction mechanisms[41], they remain largely unexploited in the study of photochemical reactions despite some telling examples. 1) Kirk and Kneeland monitored the competition between photoaquation and photoanation by NCS^- in $[Co(CN)_5X]^{n-}$ ($X = CN^-, N_3^-, Cl^-, Br^-, OH^-, H_2O$) complexes, also monitoring the ratio of N- and S- bound photoanation products.[102] 2) In studies of photoinduced C-H bond activation in complexes such as $Cp^*Ir(CO)_2$, competition experiments have been used to reveal varying reactivities of hydrocarbons with the active metal complex fragment.[103-105] This section presents the results of a competition study probing the wavelength dependence of product selection in the photoinduced substitution reaction of $W(CO)_5py$.

The photochemistry of $W(CO)_5L$ (L = pyridine, piperidine) is simple and not complicated by multiple photochemical pathways.[106] The primary photoreaction is the dissociative photosubstitution:

$$W(CO)_5L \xrightarrow[S]{h\nu} W(CO)_5S + L$$

where L is the N-donor ligand and S is the solvent. Picosecond absorption spectroscopy has shown that the primary product $W(CO)_5S$ is formed completely with a time constant of less than 20 ps.[23] Despite the apparent simplicity of this reaction, studies of wavelength and solvent dependence have revealed complicated electronic and medium effects.[23,37] To gain further insight into these effects, photosolvation competition experiments were undertaken.

Experimental:

$W(CO)_5py$ and $W(CO)_5pip$ were prepared previously in this laboratory (see Moralejo et al. Inorg. Chem. 1989, 28, 2205 and Langford et al. Coord. Chem. Rev. 1997). HPLC grade acetonitrile was obtained from EM Science. Water was double deionized. Triethylamine (99%; BDH) and piperidine (99%; Aldrich) were used without further purification.

$W(CO)_5py$ was irradiated in a two-component solvent mixture consisting of equimolar piperidine (pip) and triethylamine (TEA). The reaction mixture was monitored by HPLC at various irradiation times. A sample chromatogram is given in Figure A.1. The decrease in $W(CO)_5py$ and the increase in $W(CO)_5pip$ product were quantified. The increase in the product $W(CO)_5TEA$ was not quantified but inferred by difference. Concentrations $[W(CO)_5pip]$ vs. $[W(CO)_5py]$ were plotted and the slopes determined over the first 10% conversion in each run. Secondary photoproducts were not detected by HPLC up to 10% conversion and remained below detection limits for conversions up to 70%. Plots of $[W(CO)_5pip]$ vs. $[W(CO)_5py]$ were linear up to 10% conversion (see Figures A.2, A.3), ruling out complications arising from secondary photolysis.

Runs were performed in triplicate at four different irradiation wavelengths: 313-, 365-, 436-, and 488-nm. Wavelengths were selected (± 20-nm) with interference filters. The light source was a PTI A-1010 200-W Xe/Hg arc lamp, with the appropriate interference filter. Irradiation times ranged from 15 seconds to 5 minute intervals, depending on the irradiation wavelength. Initial $W(CO)_5py$ concentrations were 1.5-3.0 x 10^{-3} M. Solutions of $W(CO)_5py$ in pip/TEA (1:1; mol:mol) were irradiated in a 1 cm quartz cell equipped with a small magnetic stir bar and septum.

50 μL aliquots of the reaction mixtures were removed after each irradiation interval and diluted by a factor of ten into 450 μL of acetonitrile. 20 μL of the diluted sample were analyzed on a Waters HPLC with a Nova-Pak C_{18} column (3.9 x 15 mm) and Waters 486 Tunable Absorbance Detector set at 310-nm. 60:40 acetonitrile-water was the eluent. Only the concentrations of $W(CO)_5py$ and $W(CO)_5pip$ were quantified.

Results and Discussion:

Results are listed in Table A.1. At high excitation energy (313-nm), the -pip and -TEA substituted products are formed in a ratio that is close to statistical. As the excitation energy is decreased, there is a marked preponderance of the -pip product. A plot of the ratio $d[W(CO)_5pip]/d[W(CO)_5py]$ versus excitation energy is shown in Figure A.4, revealing an apparent linear relationship between nucleophile selectivity and excitation energy.

Table A.1. Product ratios with varying excitation wavelength.			
Excitation Energy		$\frac{-d[W(CO)_5pip]^a}{d[W(CO)_5py]}$	$\frac{d[W(CO)_5pip]^b}{d[W(CO)_5TEA]}$
(nm)	(cm^{-1})		
313	31950	0.53 ± 0.01	1.1
365	27400	0.61 ± 0.01	1.6
436	22940	0.80 ± 0.01	4.0
488	20490	0.87 ± 0.01	6.7

(a) Average result from three trials, followed by the standard deviation.
(b) Derived values in this column were calculated from the experimentally determined ratios: -d[W(CO)5pip]/d[W(CO)5py].

The results are highly complementary to solvent effect data. A previous study investigated solvent effects at each of the excitation wavelengths used here.[37] Solvent effects were dependent on the excitation wavelength. At high excitation energy (313-nm) there is a simple, classical viscosity dependence of the quantum yield. At intermediate energies (365- and 436-nm) there is a complex viscosity and thermal conductivity related solvent dependence. At low energy (488-nm) there is only a weak solvent dependence that cannot be explained by a suitably small solvent parameter set. The solvent dependences originate from cage effects. The classical cage effect, where the solvent cage favours recombination of the geminate pair, correlates with solvent viscosity. The thermal cage effect involves the loss of excess vibrational energy from the photo-active species to the bulk solvent. This cage effect correlates with the thermal conductivity of the solvent. As excitation energy is decreased, the role of bound excited states (i.e. states having a well defined potential well) becomes more significant to the

relaxation dynamics due to the ability of bound states to trap the system. At high excitation energy, there is enough excess energy for the system to overcome the energy barriers associated with these bound states, and they play little role in determining the relaxation pathways. At lower excitation energies, bound states become more important. The role of such trap states in $W(CO)_5py$ and their relation to the solvent effects observed in this system has been discussed extensively.[37]

The solvent effect data and the competition results presented here illustrate the importance of excess excitation energy in determining the fate of a geminate pair. Excess excitation energy is the difference between the energy contained in the absorbed photon and the ground state bond dissociation energy. This excess excitation energy is distributed as kinetic and vibrational energy in $W(CO)_5$ and py. The loss of kinetic and vibrational energy to the solvent leads to solvent cage effects (i.e. the viscosity and thermal conductivity dependences noted above). The results of this study provide information about the excess vibrational energy of the $W(CO)_5$ fragment and how it affects the reactivity towards donor molecules in the solvent cage. A 'cool' $W(CO)_5$ (low excess excitation energy) is quite selective towards nucleophiles. A 'hot' $W(CO)_5$ (high excess excitation energy) shows little selectivity. This firmly underlines that products can be determined prior to vibrational relaxation, probably in a non Born-Oppenheimer domain.

It is interesting to note that significant differences in nucleophile selectivity can be measured in this system. A picosecond absorption study into the nature of the primary products, $W(CO)_5S$, present 50 ps after a 355-nm flash (high excitation energy),[25]

showed that long chain alcohols and alkenes form alkyl coordinated transients (i.e. σ-complexes) in large excess of the alcohol and alkene coordinated final products. The stable products are formed in approximately 600 ps. In n-butanol, 70% of the products at 50 ps were alkyl coordinated transients. For this competition study, it might then be expected that most of the primary products are σ-complexes and that no significant competition for nucleophile donor atoms would occur. If the competition somehow involves σ-complexes and not naked $W(CO)_5$, a wavelength independent ratio of products would be expected. This is not the case.

This is the first time that a competition study has been used to probe the wavelength dependence of a photochemical reaction. Competitive photosolvation may prove to be a versatile method in mechanistic photochemistry due to the flexibility in the choice of donor solvents that can be used. While this study relied on steric differences between secondary and tertiary amines, it should be possible to exploit electronic differences between solvents with different donor atoms (e.g. phosphines vs. amines).

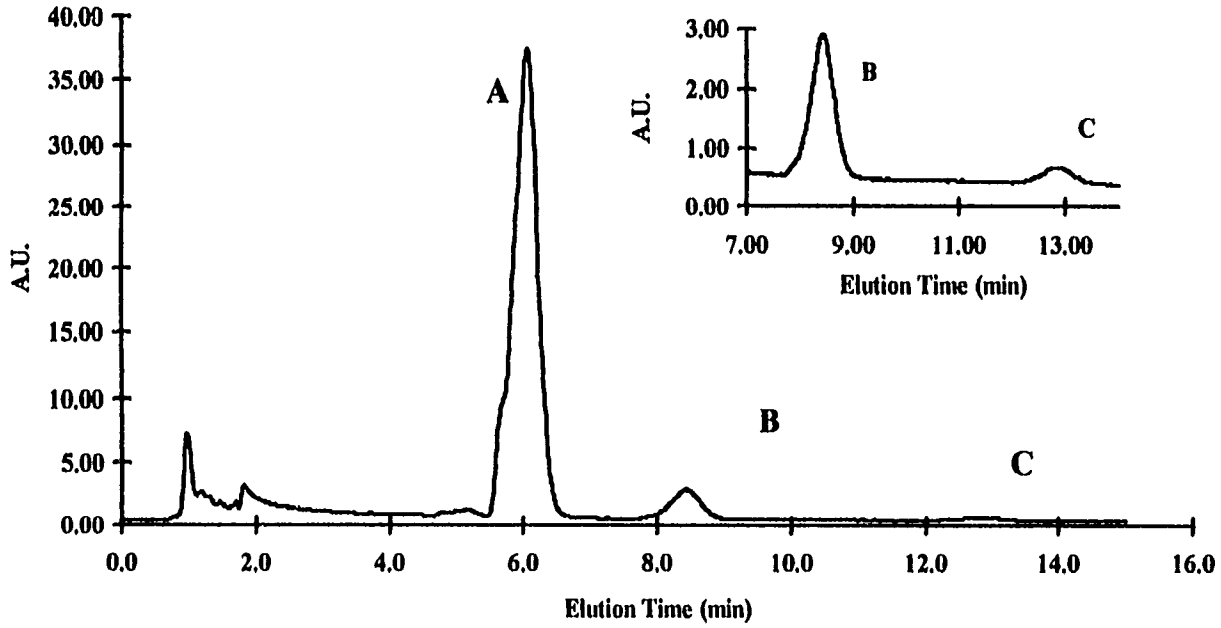

Figure A.1. Chromatogram of a 365-nm photolysis mixture. Peaks are: A) $W(CO)_5py$; B) $W(CO)_5pip$; C) $W(CO)_5TEA$. The inset shows the product peaks. LC analysis was performed on a C_{18} column, with a tunable absorbance detector set at 310-nm. 60:40 acetonitrile/water was the eluent.

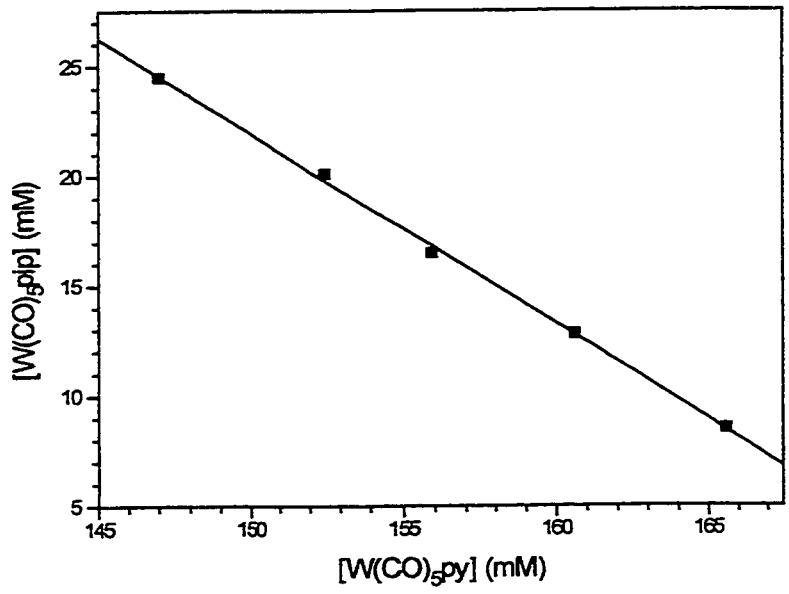

Figure A.2. Example of a plot of [W(CO)5pip] vs. [W(CO)5py], 488-nm excitation. Slope = 0.866 from a linear regression routine, $r^2 = 0.9986$.

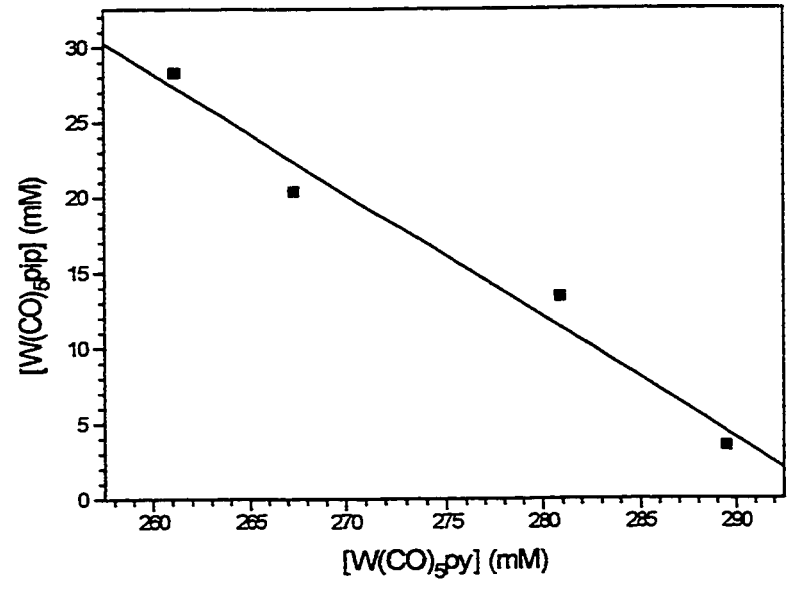

Figure A.3. Example of a plot of $[W(CO)_5pip]$ vs. $[W(CO)_5py]$, 436-nm excitation. Slope = 0.806 from a linear regression routine, $r^2 = 0.9710$.

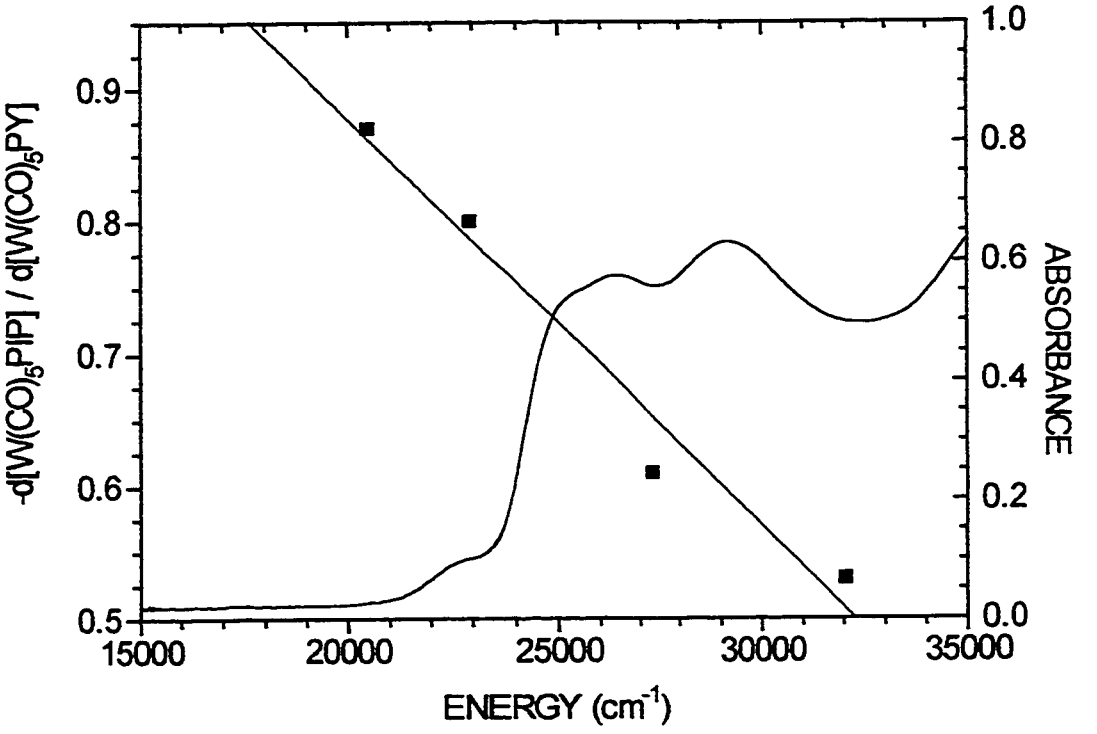

Figure A.4. Plot of the slopes -d[$W(CO)_5$pip]/d[$W(CO)_5$py] vs. excitation energy. The absorption spectrum of $W(CO)_5$py in piperidine/TEA (1:1; mol:mol) is superimposed (concentration = 5.7×10^{-4} M, measured in a 2 mm quartz cell). The straight line through the data points is the result of a linear regression routine, $r^2 = 0.9725$.

APPENDIX B: EXTINCTION COEFFICIENTS USED IN QUANTUM YIELD DETERMINATIONS

All extinction coefficients are at worst ± 5%.

Table B.1 Extinction coefficients of $Cr(CNPh)_6$ in various solvents.

Solvent	Wavelength (nm)	ε (M^{-1} cm^{-1})
Benzene	313	33000
	356	40740
	365	44740
	404 (max)	69350
	436	55100
	488	36600
	514	17000
	560	1100
Toluene	313	25140
	365	31200
	404 (max)	47000
	436	37550
	488	25300

Table B.1. continued

	532	4880
	600	≈100
Pyridine	356	45500
	366	51500
	400 (max)	71000
	436	55000
	488	36250
	514	17100
	600	≈100
DMSO	313	12780
	366	19300
	390 (max)	22800
	436	15900
	532	1600
	540	1040

Table B.2 Extinction coefficients of photosubstitution products of $Cr(CNPh)_6$		
Product	Wavelength (nm)	ε (M^{-1} cm^{-1})
$Cr(CNPh)_5py$ (in pyridine)	600	8500
$Cr(CNPh)_5py$ (in benzene)	600	10600
$Cr(CNPh)_5py$ (in toluene)	600	5830
$Cr(CNPh)_5PPh_3$ (in benzene)	514	14170
$Cr(CNPh)_5DMSO$	540	2170

Table B.3 Extinction coefficients of Ru(II) complexes in acetone		
Compound	Wavelength (nm)	ε (M^{-1} cm^{-1})
$Ru(bpy)_2py_2^{2+}$	366	7190
	436	8080
	488	3270
	500	1910
$Ru(bpy)_2(py)(acetone)^{2+}$	500	4960

Table B.4 Extinction coefficients of $Mo(CNPh)_6$ in various solvents		
Solvent	Wavelength (nm)	ε (M^{-1} cm^{-1})
Chloroform	313	75400
	366	101000
	436	65070
	488	41000
	520	9370
Pyridine	313	41550
	366	59400
	436	39100
	488	25500
	550	650
Benzene	313	40550
	366	55530
	388 (max)	69200
	436	40940
	488	27300
	514	8200
	532	2610

Table B.5. Extinction coefficients of $Mo(CNPh)_6$ photoproducts		
Product	Wavelength (nm)	ε (M^{-1} cm^{-1})
$Mo(CNPh)_5py$ (in pyridine)	550	7170
$Mo(CNPh)_5py$ (in benzene)	560	4790
$Mo(CNPh)_5PPh_3$ (in benzene)	490	16000
$Mo(CNPh)_6Cl^+$	520	4350

APPENDIX C: PICOSECOND SPECTRA OF $Cr(CNPH)_6$ IN VARIOUS SOLVENTS

This appendix contains additional picosecond absorption spectra of $Cr(CNPh)_6$ that did not appear in Chapter 3. These were measured to check for possible solvent effects on the picosecond time scale. The spectra are entirely congruent with those taken in benzene.

Some of the figures include arrows to indicate a direction of change in the spectra. These changes are sometimes within instrumental error and the arrows are only included for completion. For the case of $Cr(CNPh)_6$ in neat pyridine (Figure C.22), a moderate level of decomposition was observed from UV-vis spectra taken before and after the flash photolysis experiments and the changes seen may be due to the decomposition products. Such decomposition was not observed in any other system.

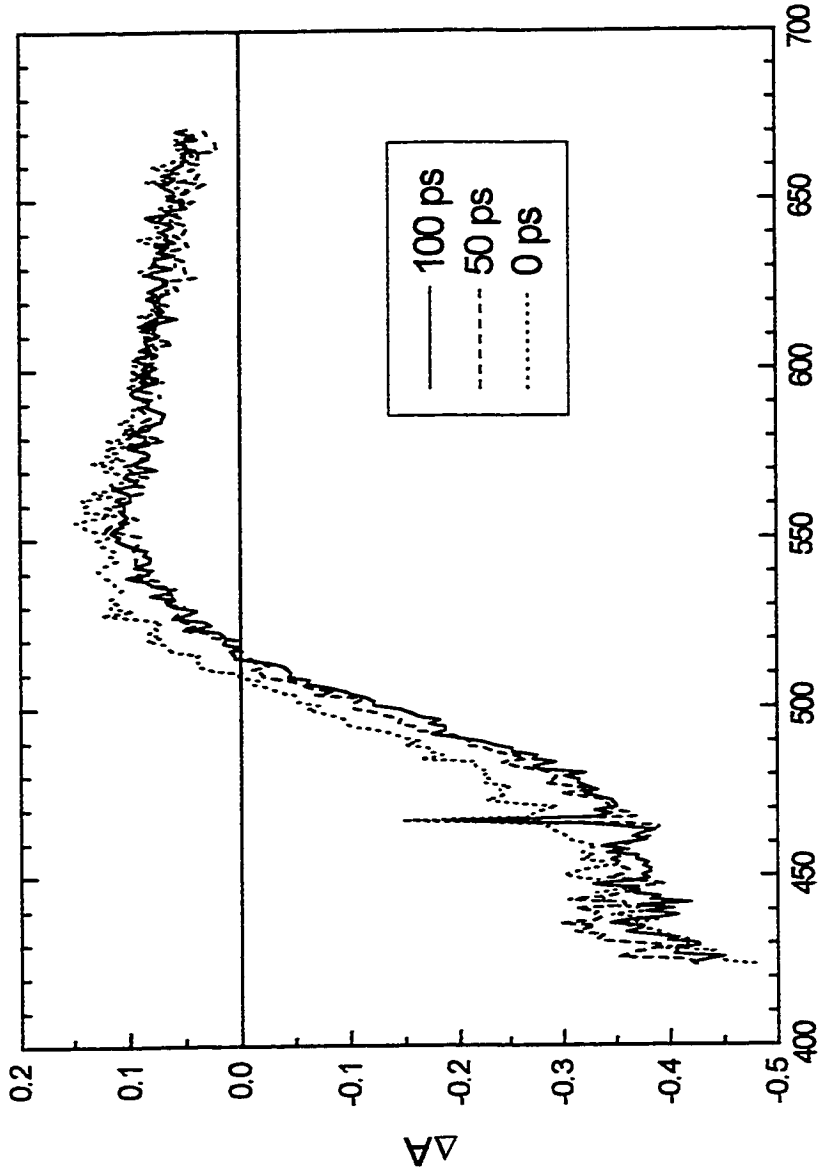

Figure C.1 Picosecond absorption spectra of $Cr(CNPh)_6$ in DMSO. 355 nm pump. Time delays 0, 50, and 100 ps.

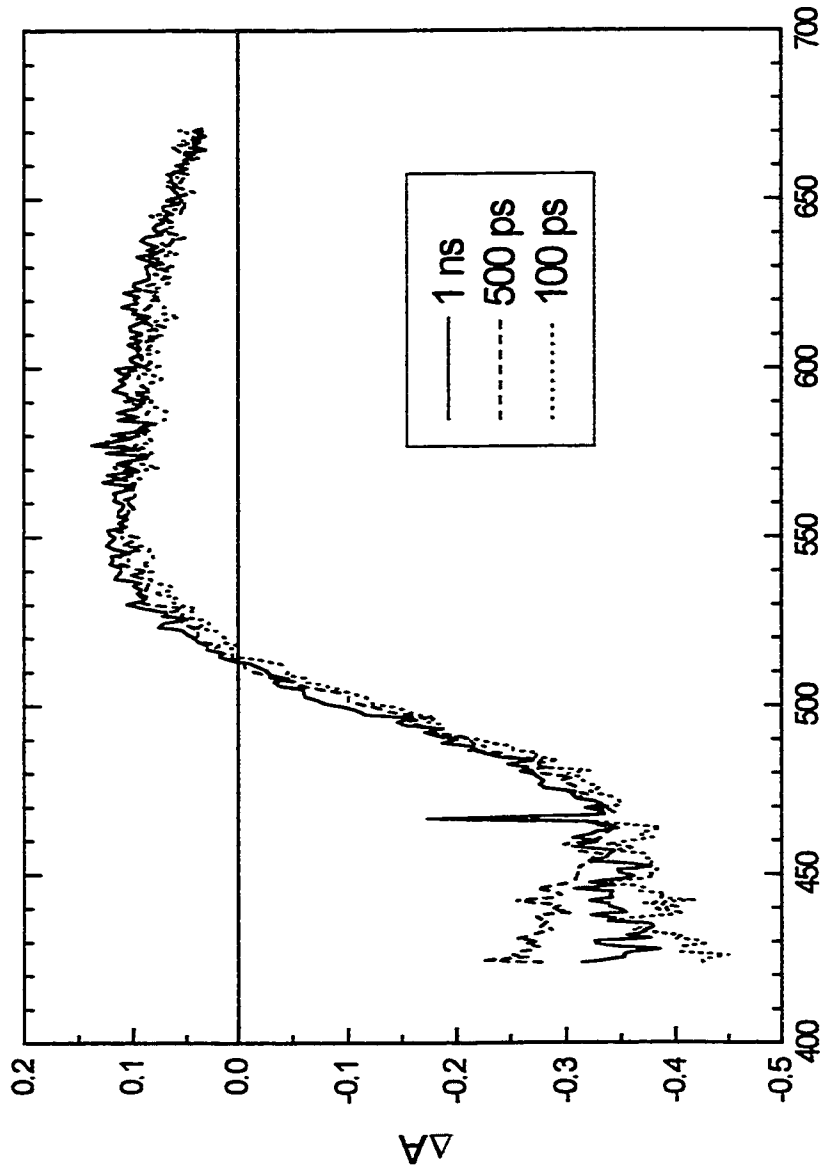

Figure C.2 Picosecond absorption spectra of $Cr(CNPh)_6$ in DMSO. 355 nm pump. Time delays 100 ps, 500 ps, and 1 ns.

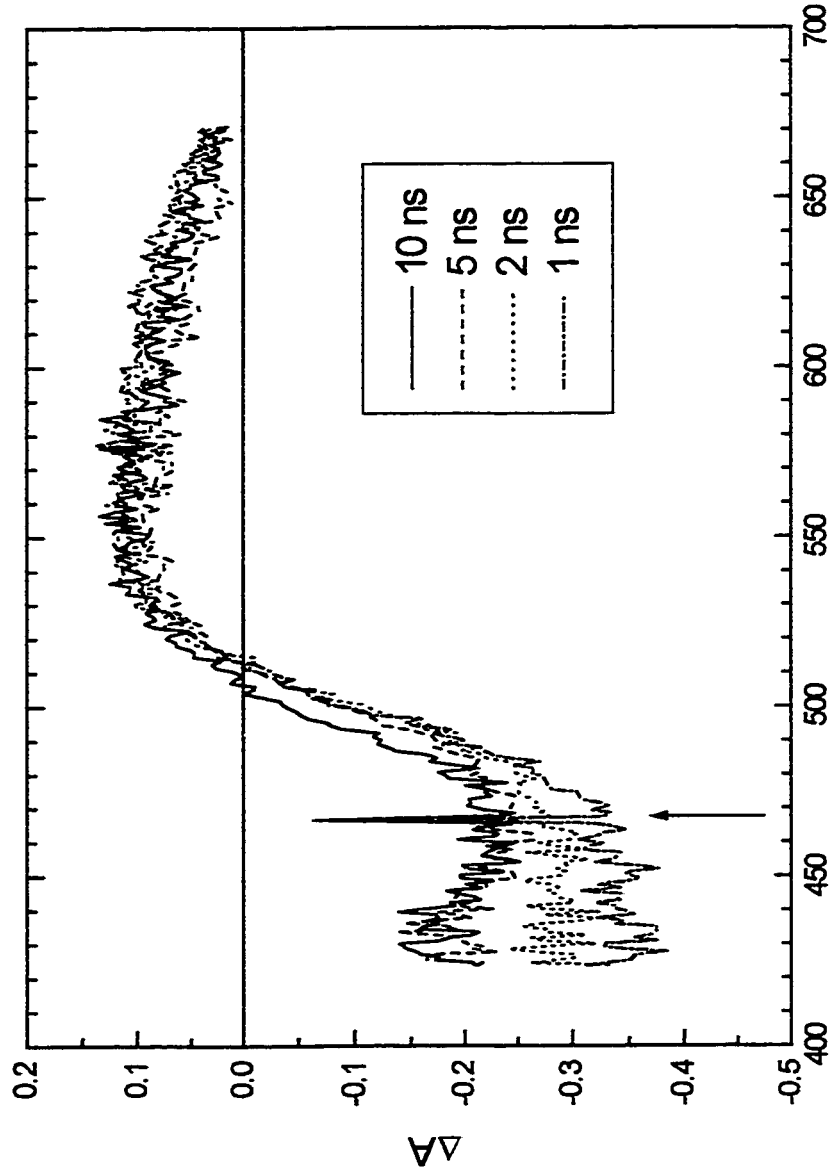

Figure C.3 Picosecond absorption spectra of $Cr(CNPh)_6$ in DMSO. 355 nm pump. Time delays 1, 2, 5, and 10 ns.

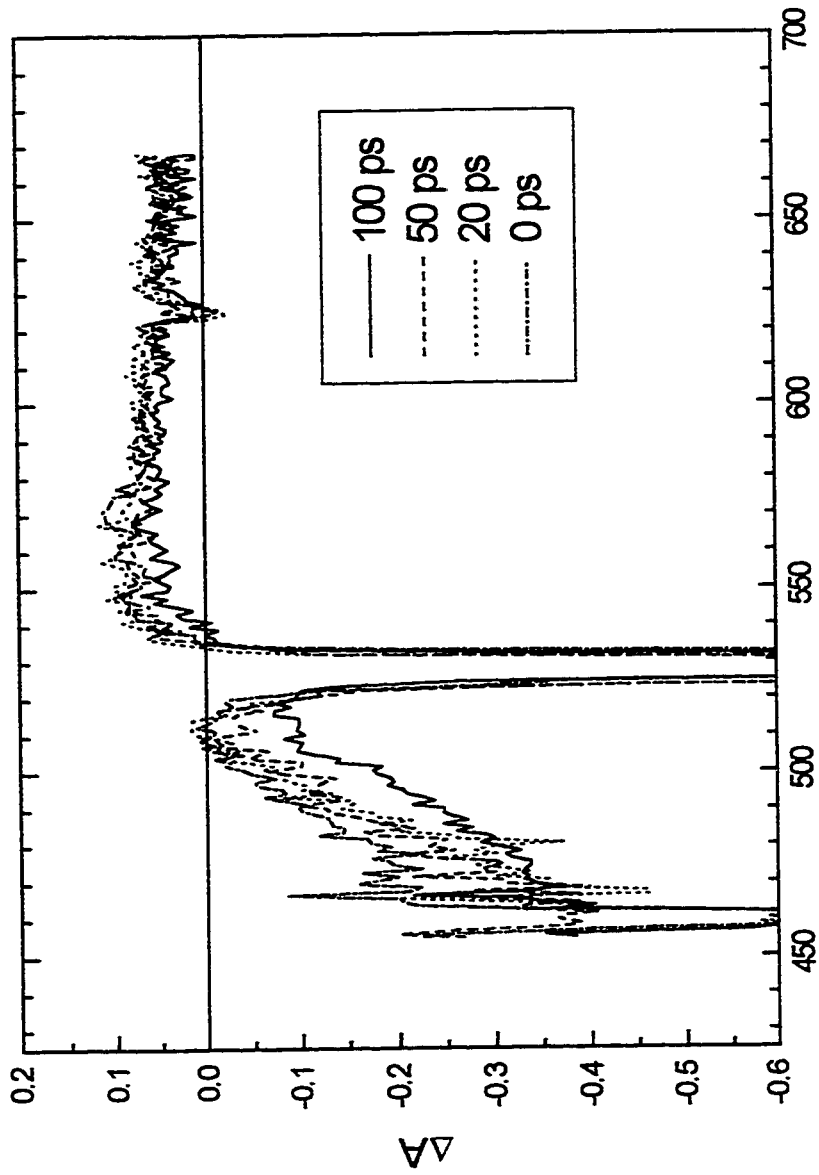

Figure C.4 Picosecond absorption spectra of $Cr(CNPh)_6$ in DMSO. 532 nm pump. Time delays 0, 20, 50, and 100 ps.

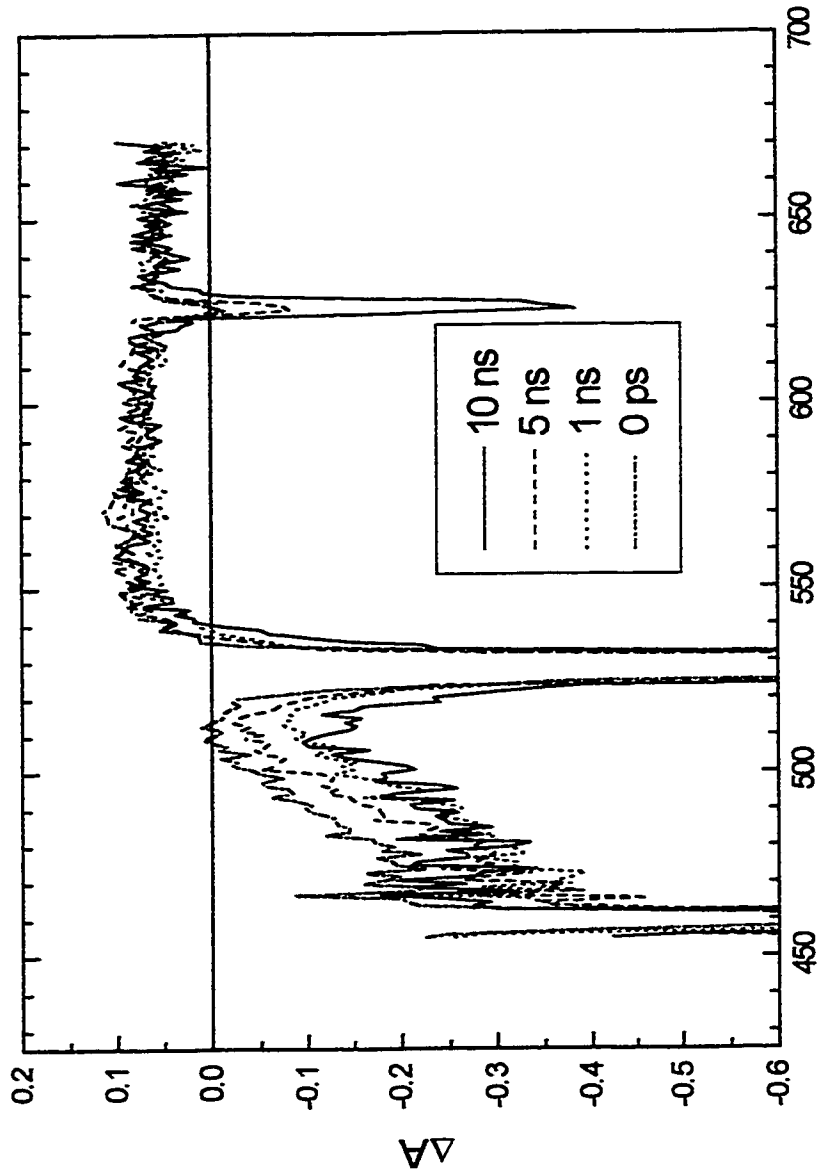

Figure C.5 Picosecond absorption spectra of $Cr(CNPh)_6$ in DMSO. 532 nm pump. Time delays 0 ps, 1 ns, 5 ns, and 10 ns.

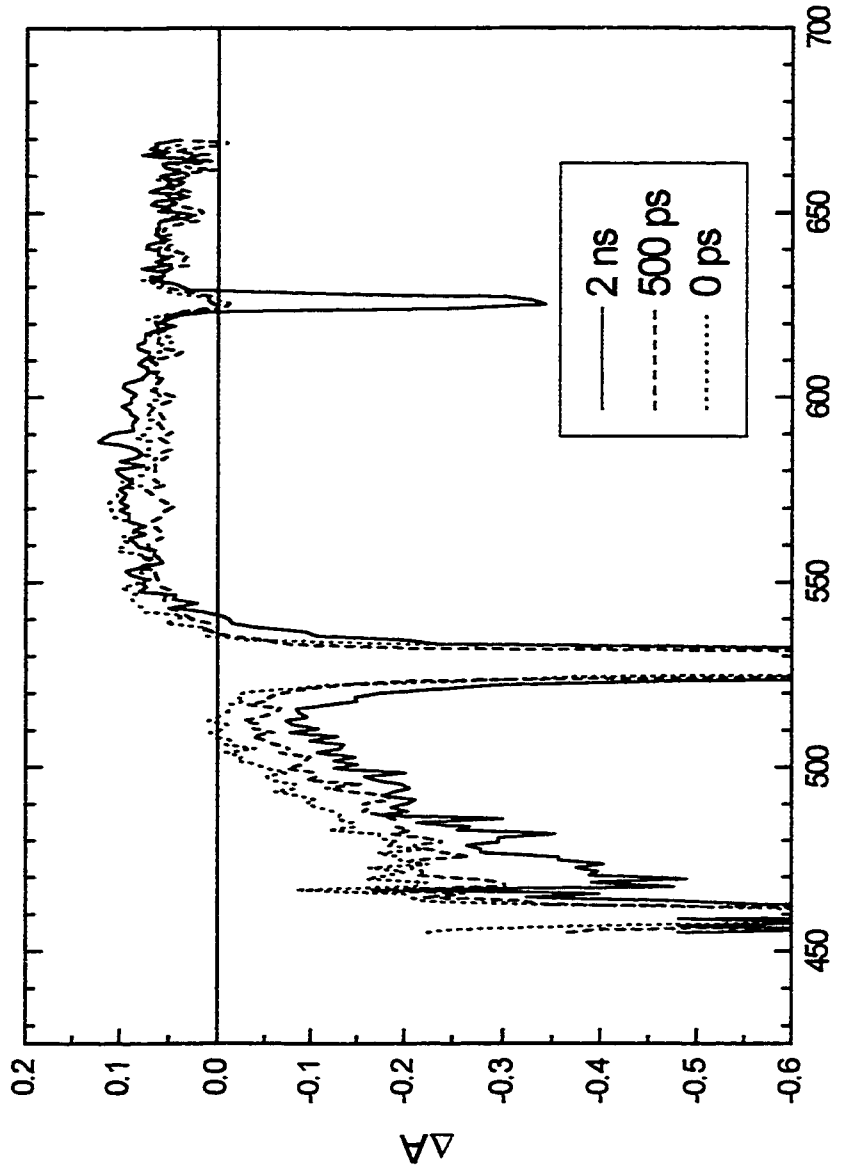

Figure C.6 Picosecond absorption spectra of $Cr(CNPh)_6$ in DMSO. 532 nm pump. Time delays 0 ps, 500 ps, and 2 ns.

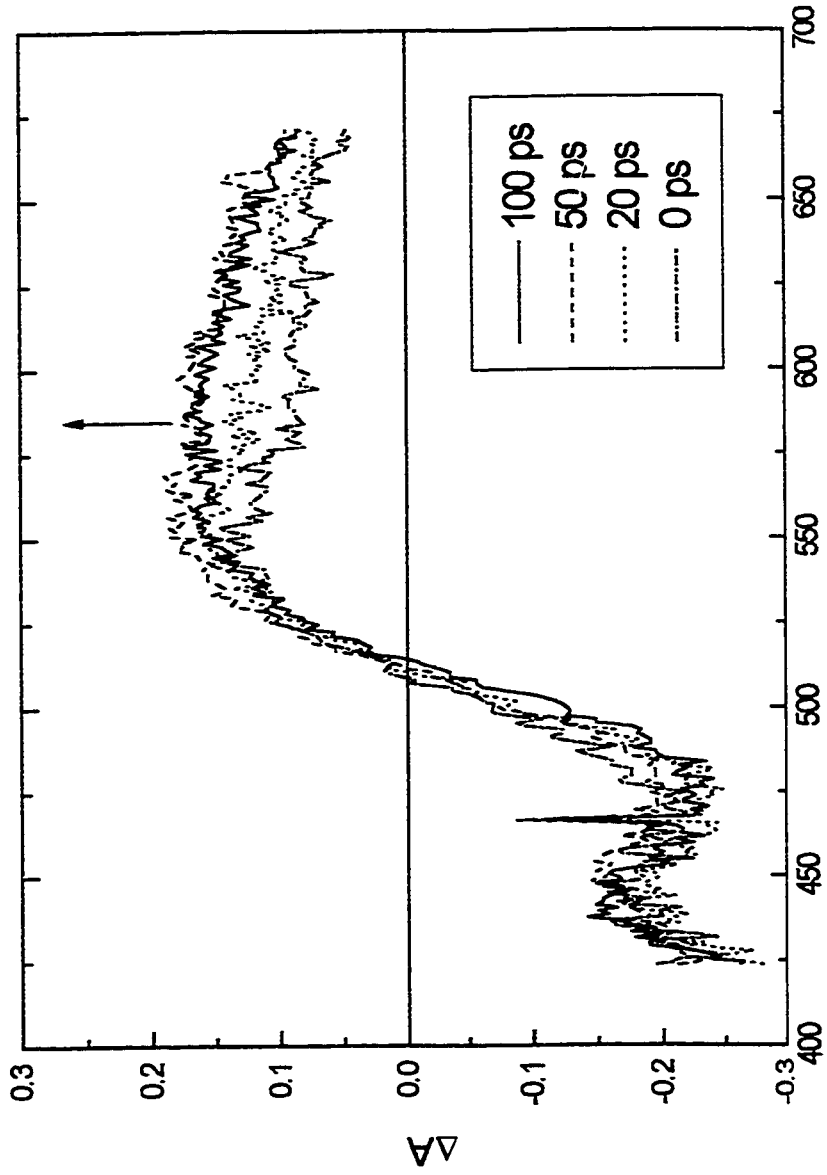

Figure C.7 Picosecond absorption spectra of $Cr(CNPh)_6$ in toluene. 355 nm pump. Time delays 0, 20, 50, and 100 ps.

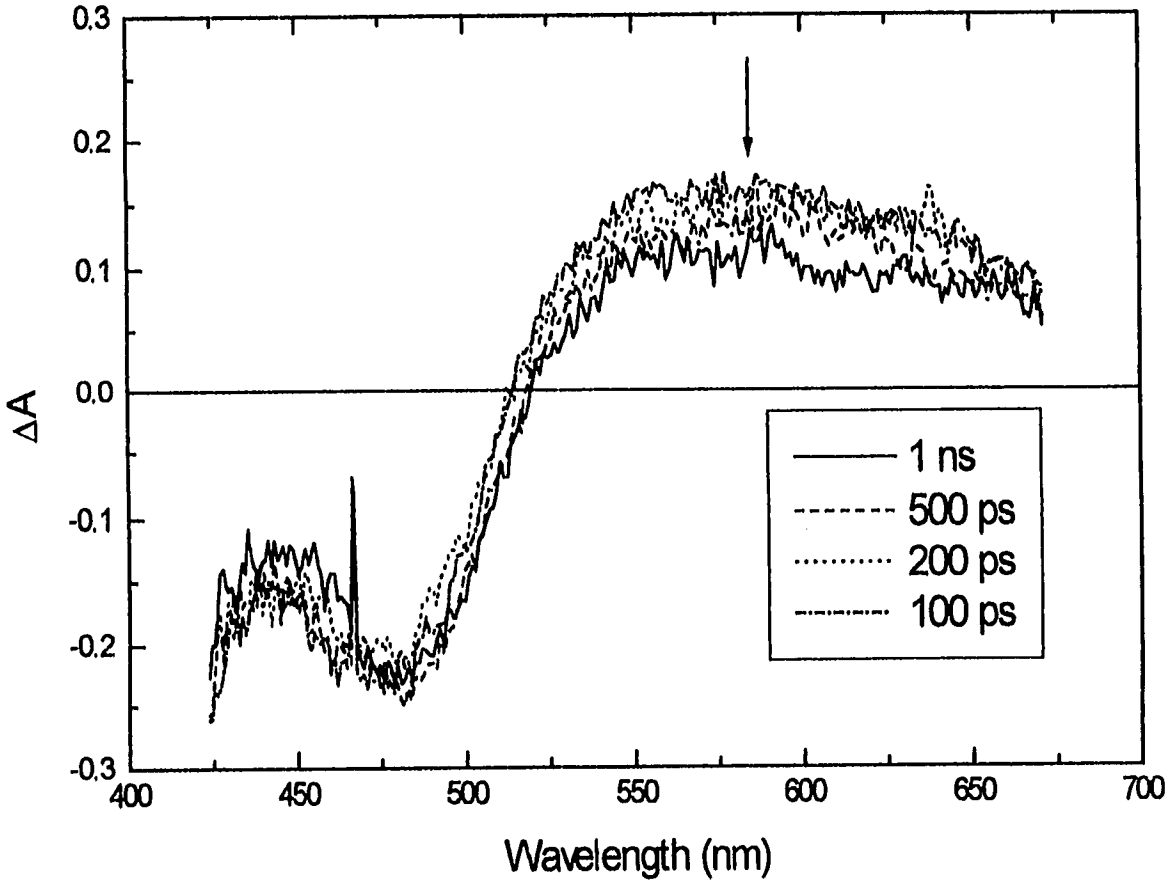

Figure C.8 Picosecond absorption spectra of $Cr(CNPh)_6$ in toluene. 355 nm pump. Time delays 100 ps, 200 ps, 500 ps, and 1 ns.

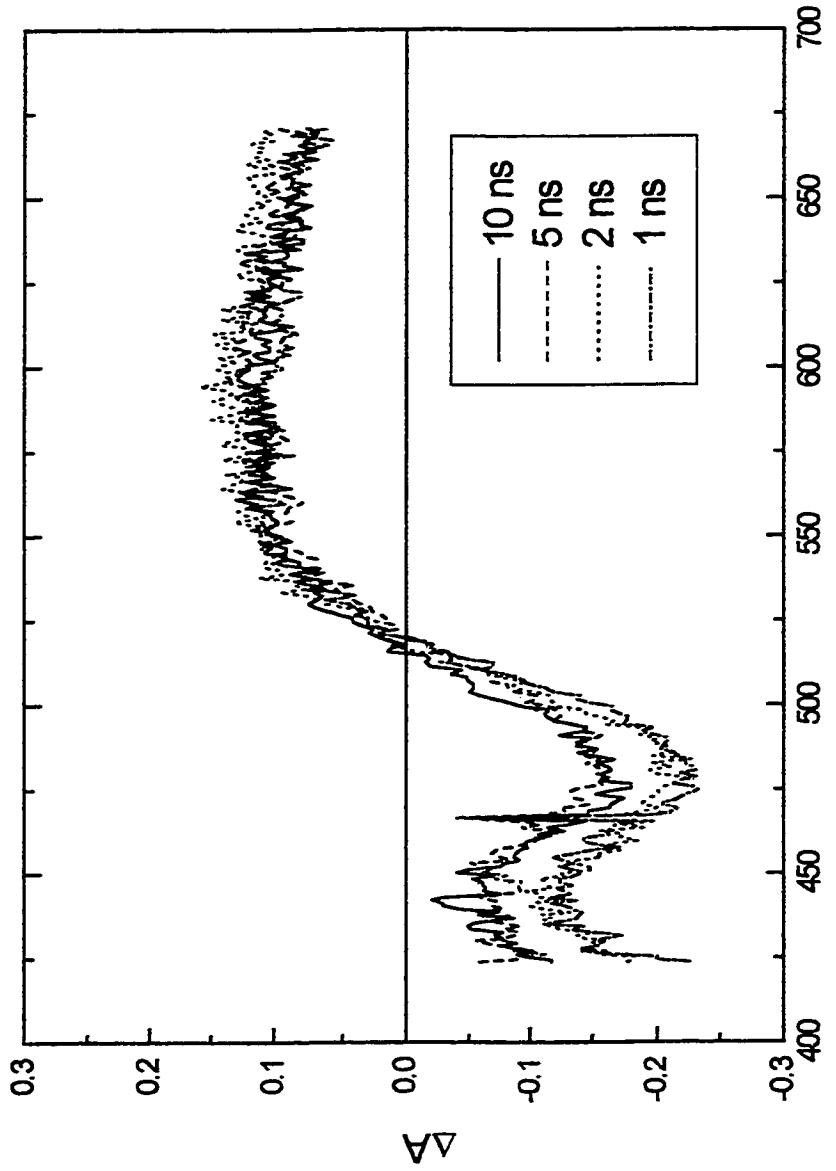

Figure C.9 Picosecond absorption spectra of $Cr(CNPh)_6$ in toluene. 355 nm pump. Time delays 1, 2, 5, and 10 ns.

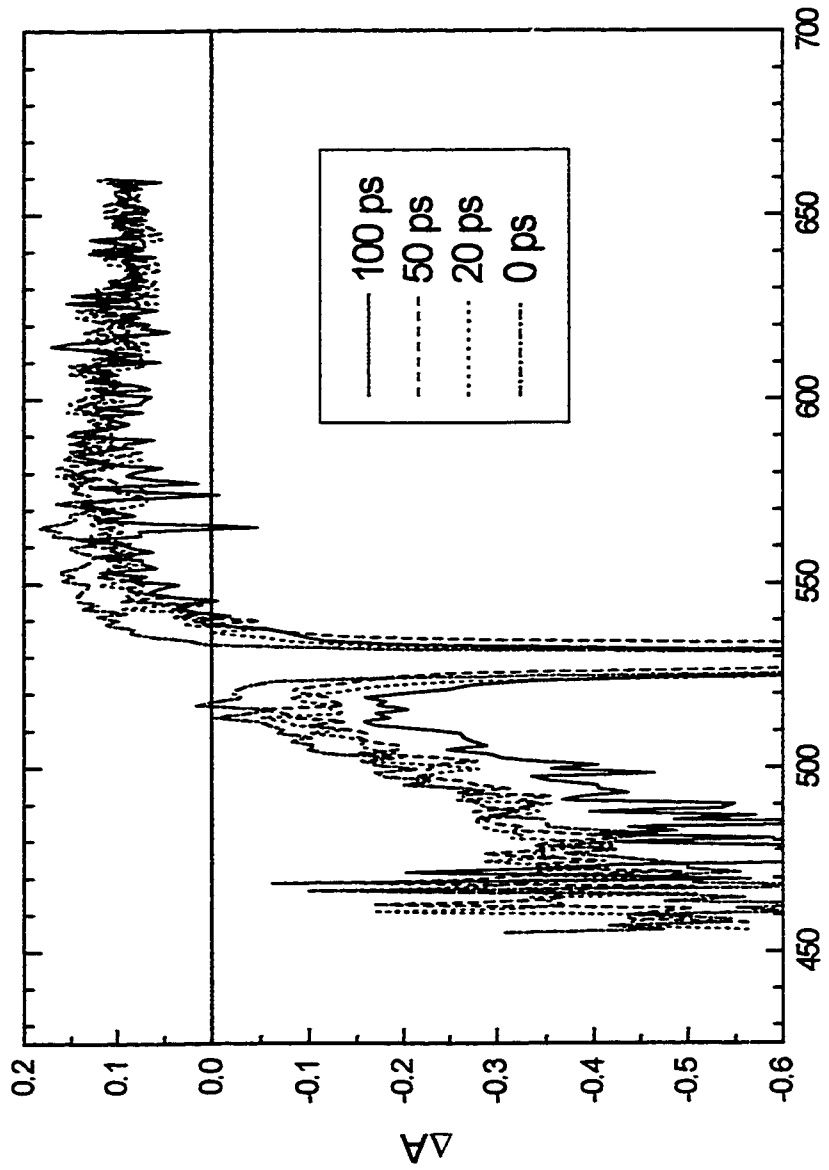

Figure C.10 Picosecond absorption spectra of $Cr(CNPh)_6$ in toluene. 532 nm pump. Time delays 0, 20, 50, and 100 ps.

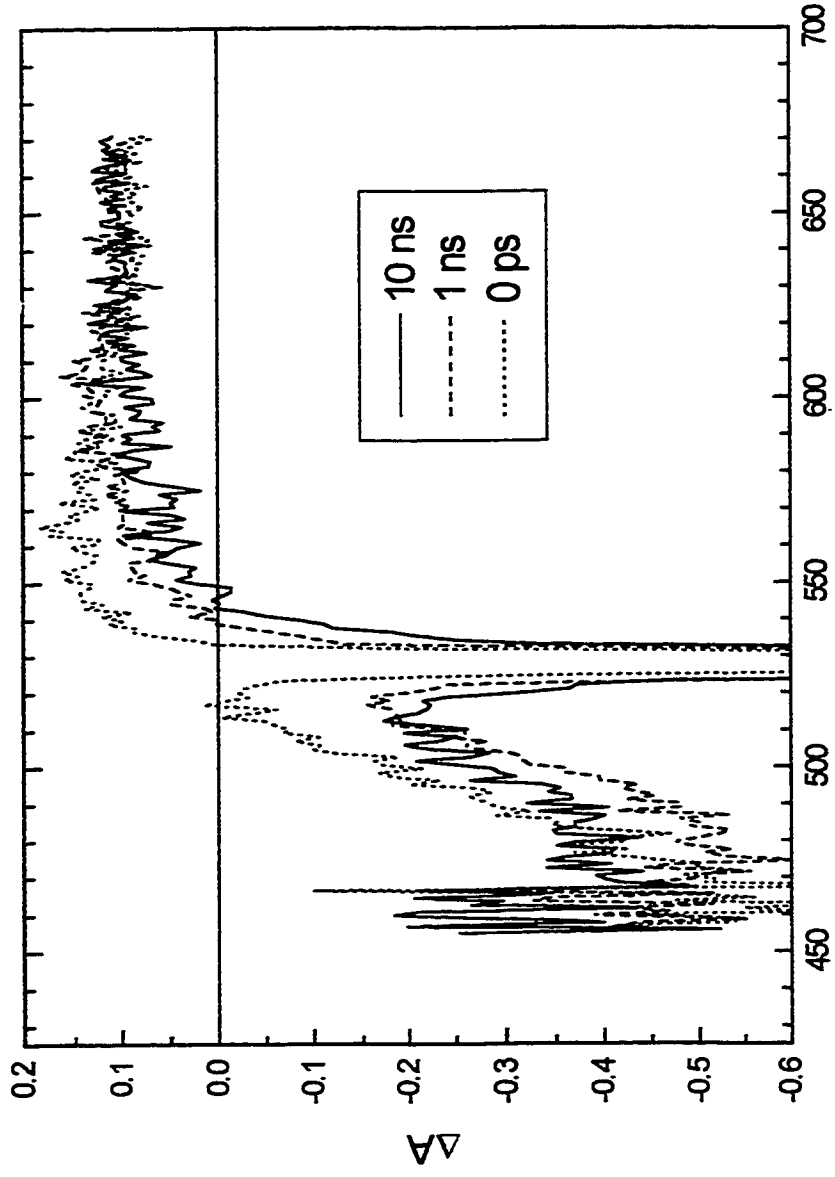

Figure C.11 Picosecond absorption spectra of $Cr(CNPh)_6$ in toluene. 532 nm pump. Time delays 0 ps, 1 ns, and 10 ns.

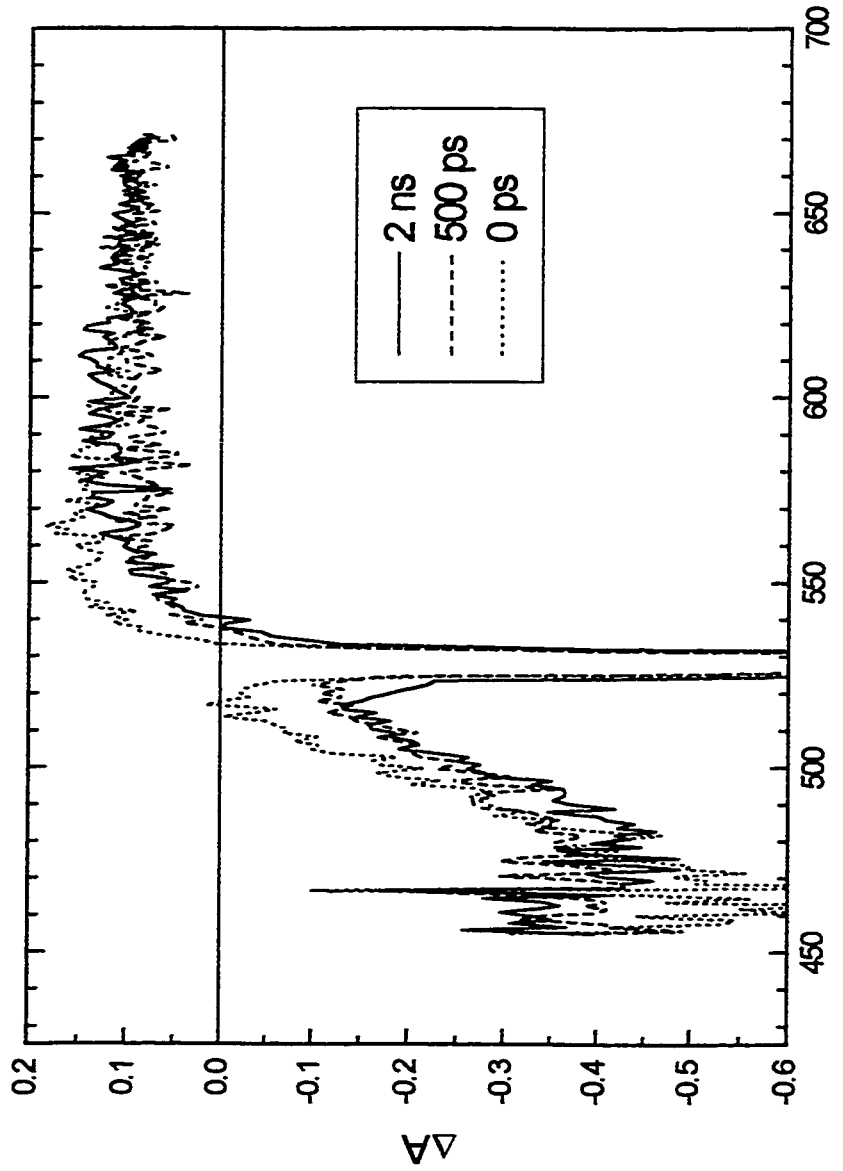

Figure C.12 Picosecond absorption spectra of $Cr(CNPh)_6$ in toluene. 532 nm pump. Time delays 0 ps, 500 ps, and 2 ns.

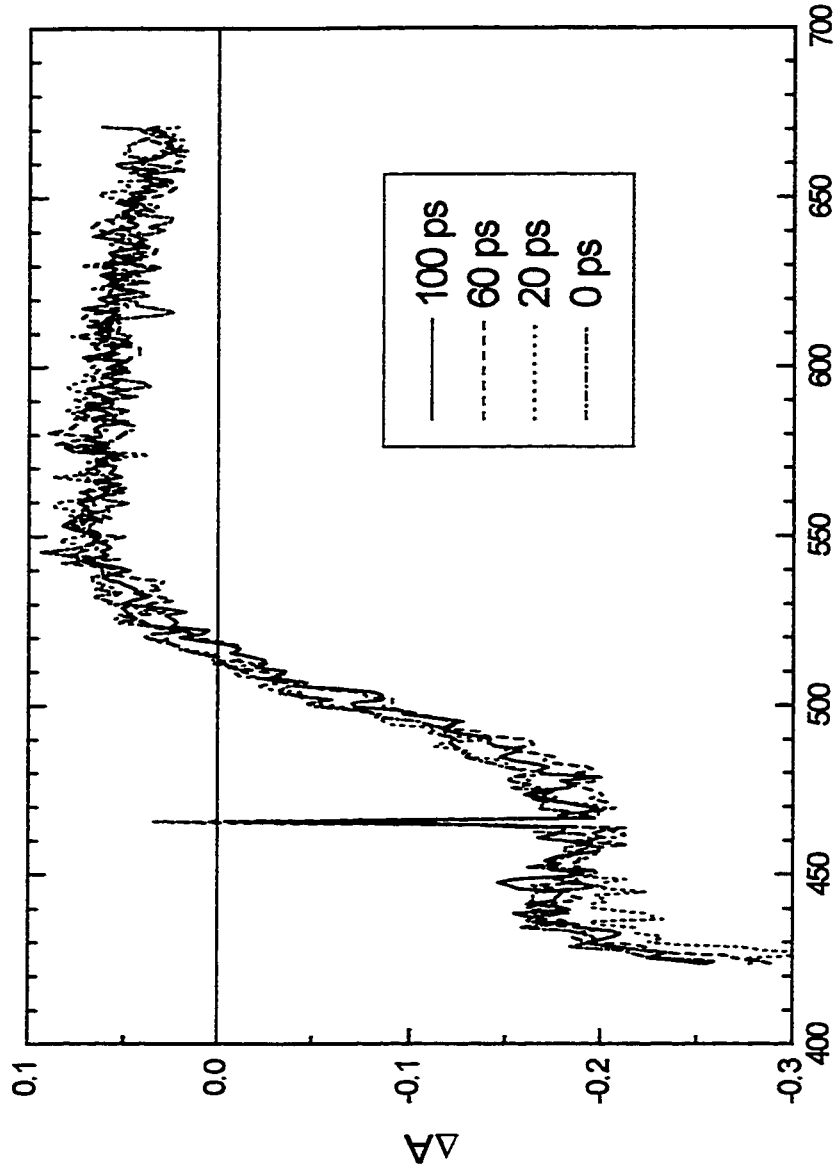

Figure C.13 Picosecond absorption spectra of $Cr(CNPh)_6$ in THF. 355 nm pump. Time delays 0, 20, 60 and 100 ps.

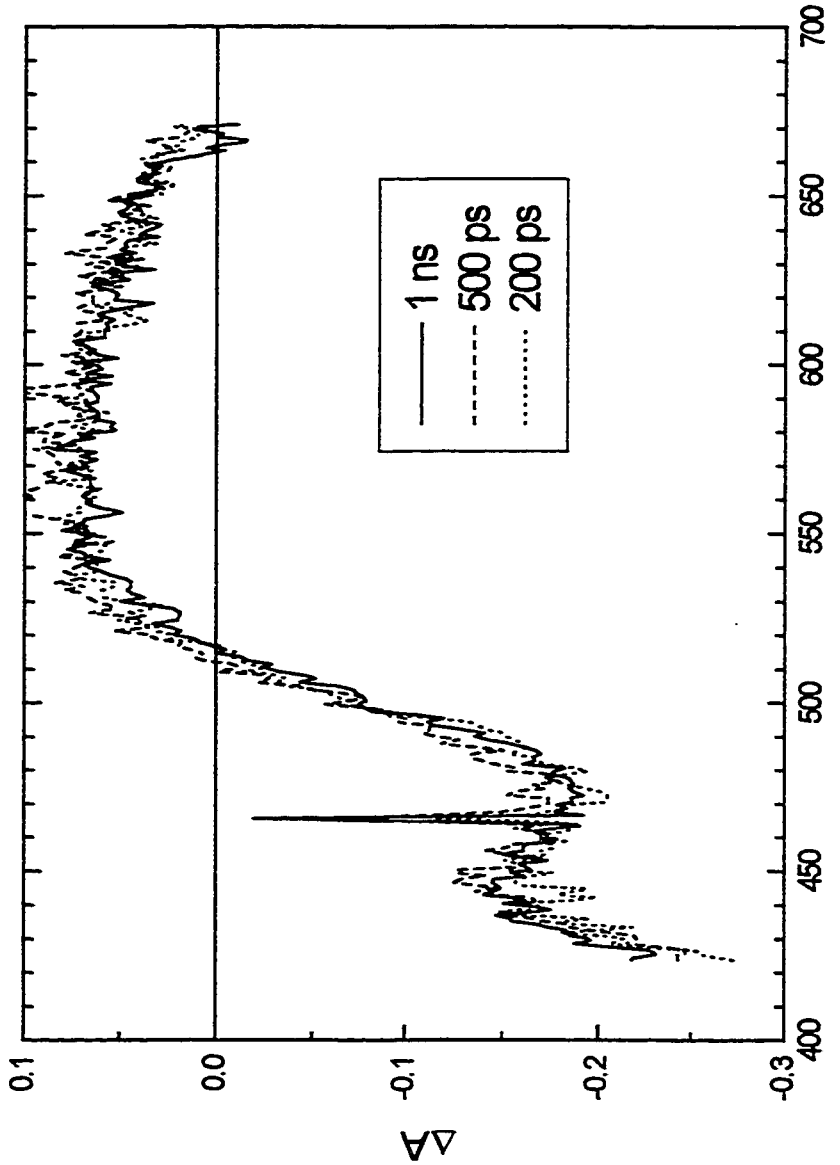

Figure C.14 Picosecond absorption spectra of $Cr(CNPh)_6$ in THF. 355 nm pump. Time delays 200 ps, 500 ps, and 1 ns.

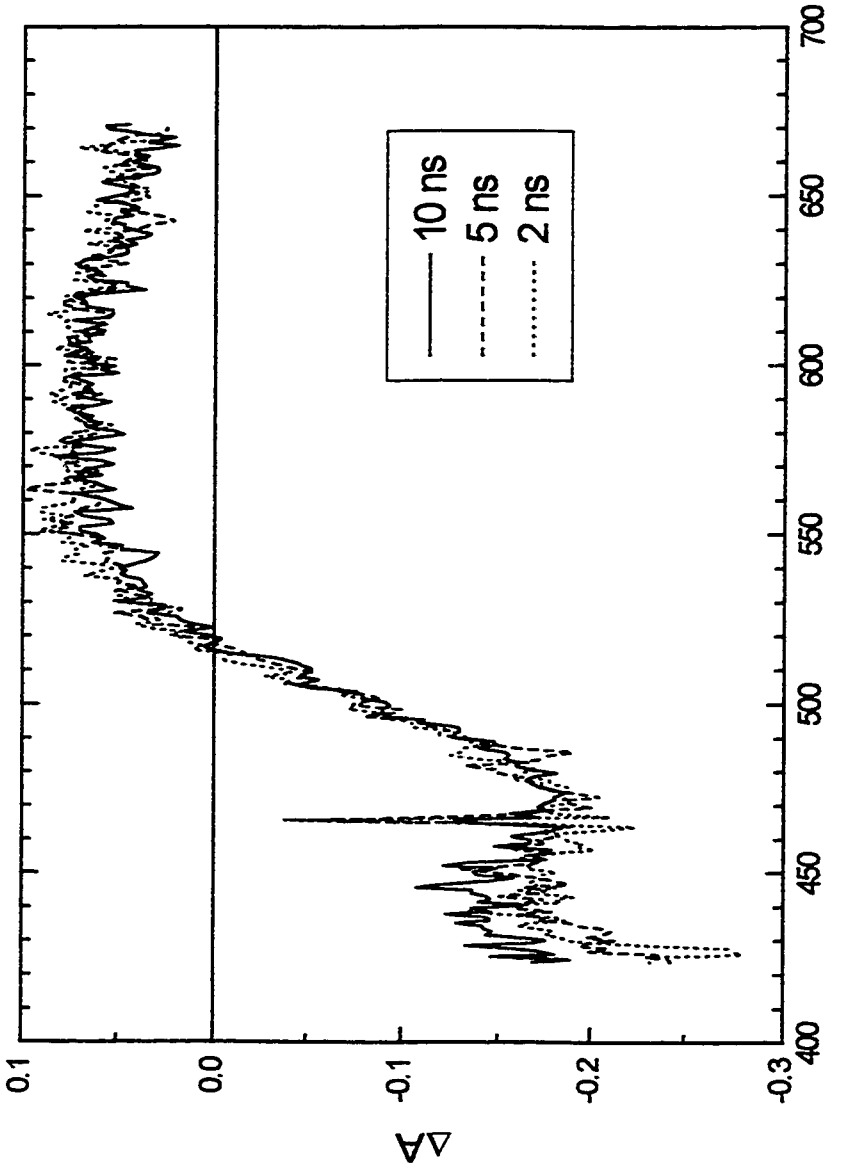

Figure C.15 Picosecond absorption spectra of $Cr(CNPh)_6$ in THF. 355 nm pump. Time delays 2, 5, and 10 ns.

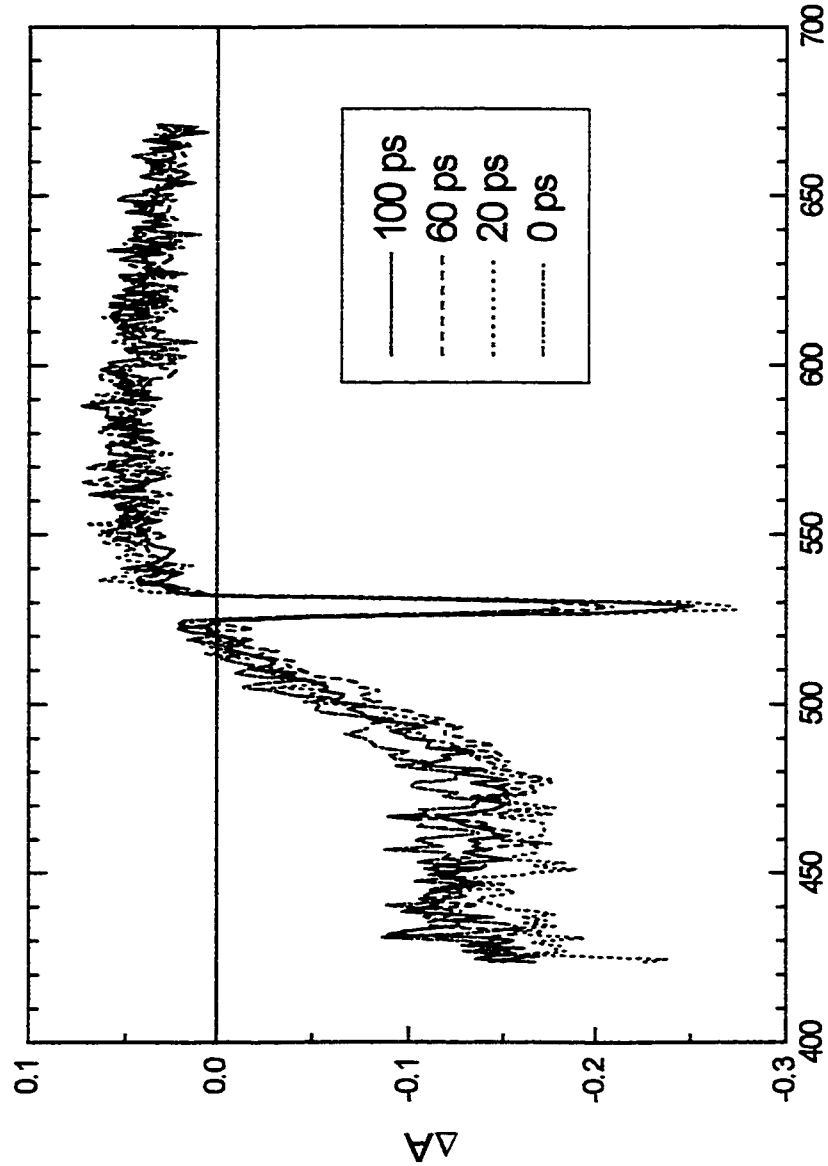

Figure C.16 Picosecond absorption spectra of $Cr(CNPh)_6$ in THF. 532 nm pump. Time delays 0, 20, 60, and 100 ps.

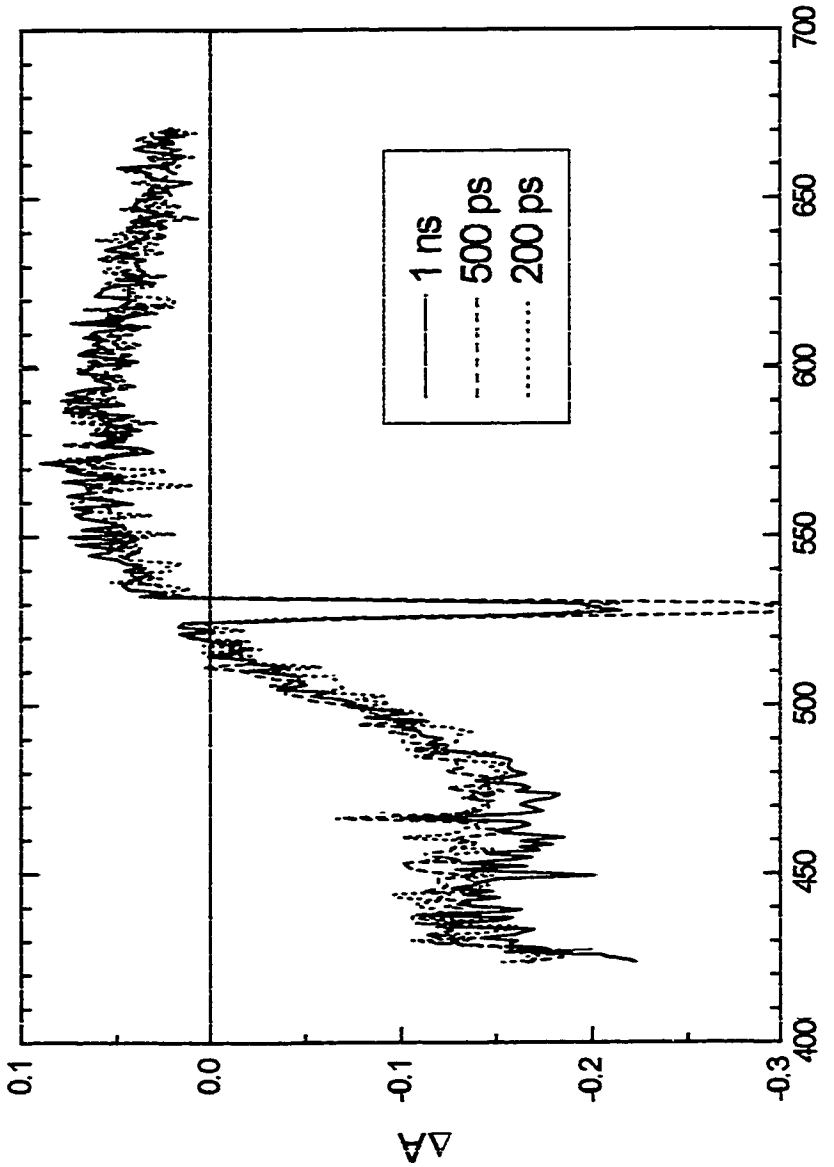

Figure C.17 Picosecond absorption spectra of $Cr(CNPh)_6$ in THF. 532 nm pump. Time delays 200 ps, 500 ps, and 1 ns.

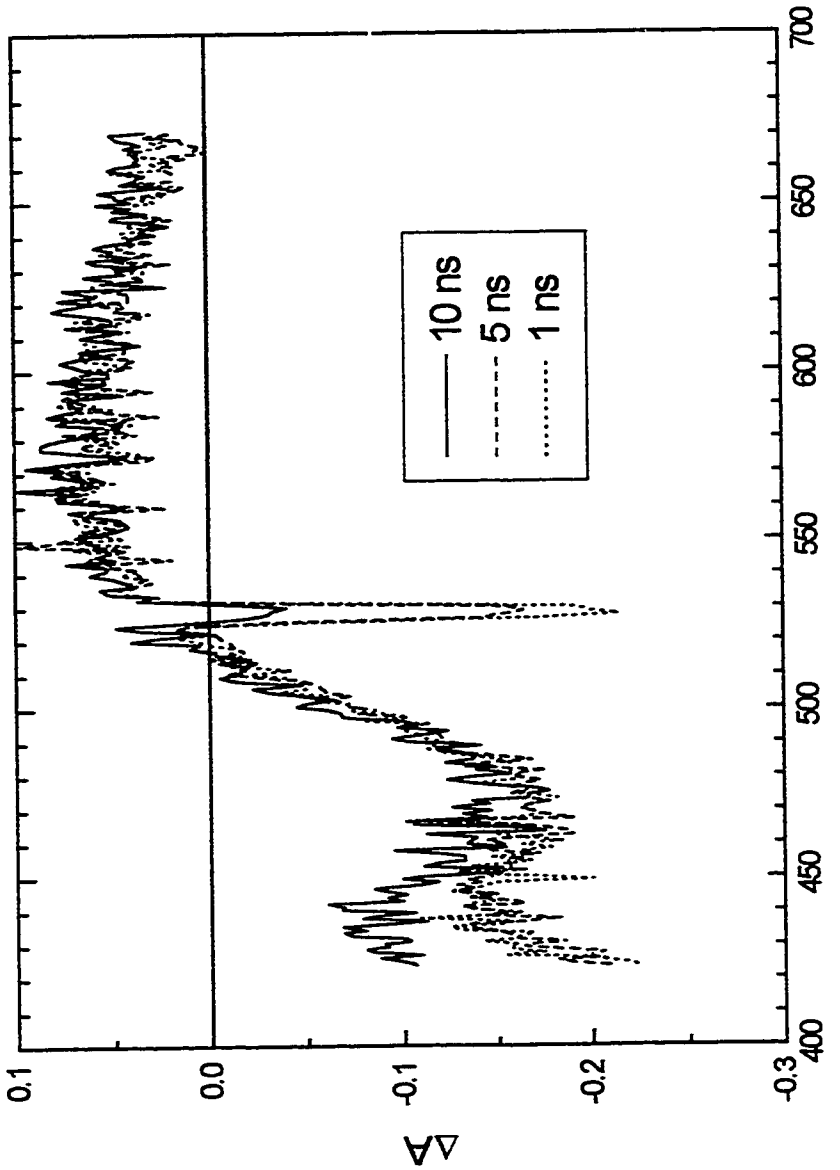

Figure C.18 Picosecond absorption spectra of $Cr(CNPh)_6$ in THF. 532 nm pump. Time delays 1, 5, and 10 ns.

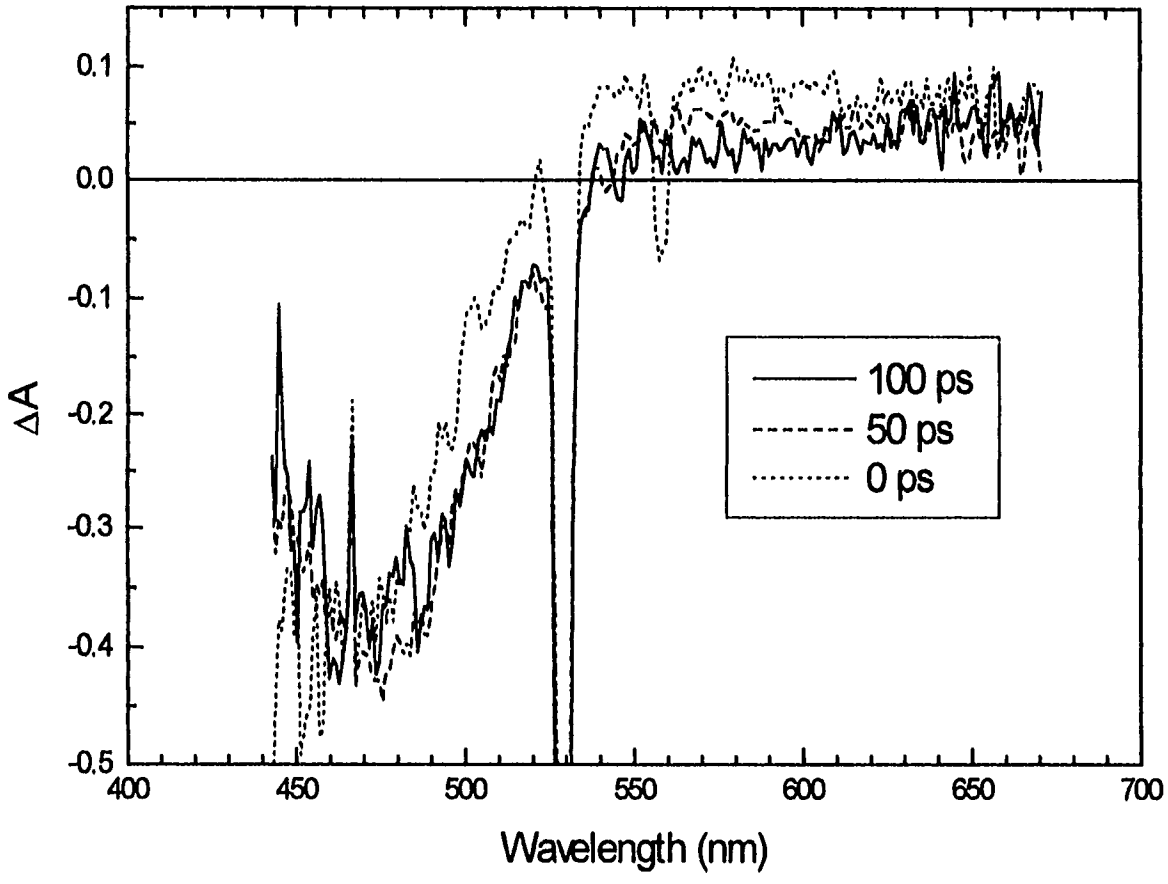

Figure C.19 Picosecond absorption spectra of $Cr(CNPh)_6$ in toluene (0.5 M py). 532 nm pump. Time delays 0, 50, and 100 ps.

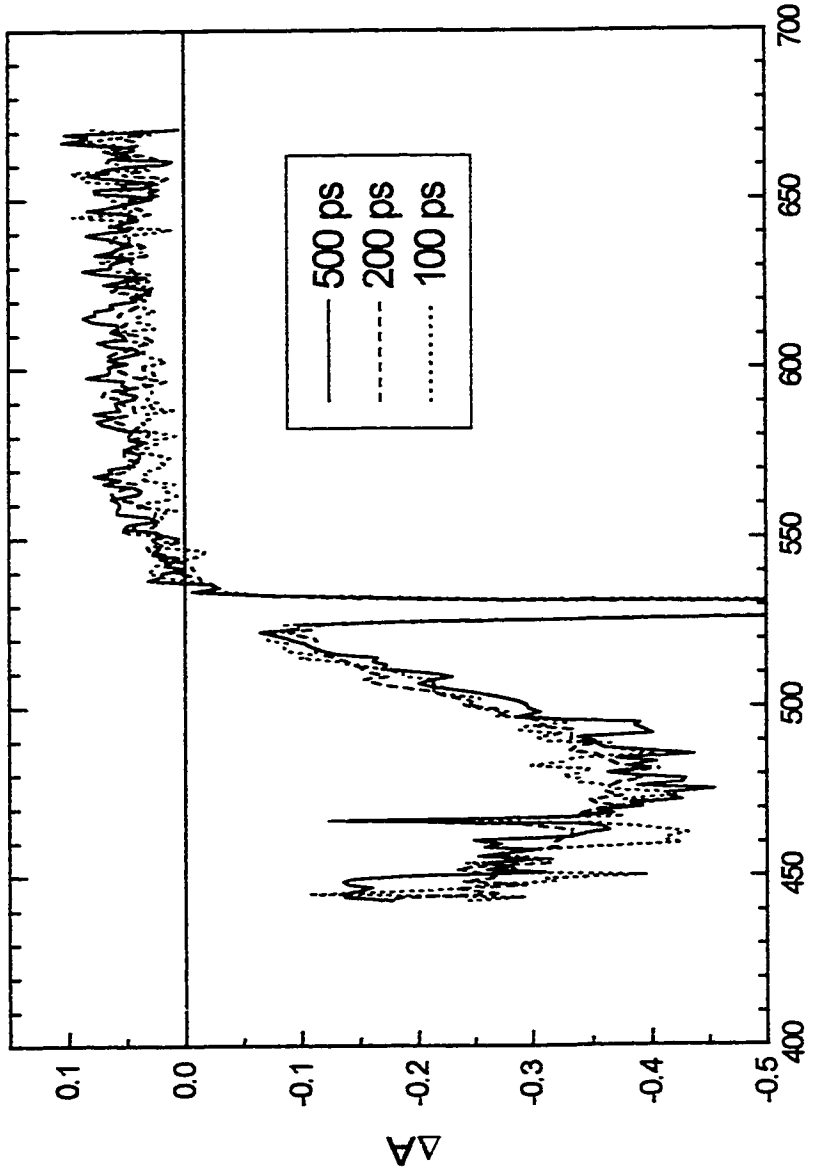

Figure C.20 Picosecond absorption spectra of $Cr(CNPh)_6$ in toluene (0.5 M py). 532 nm pump. Time delays 100, 200, and 500 ps.

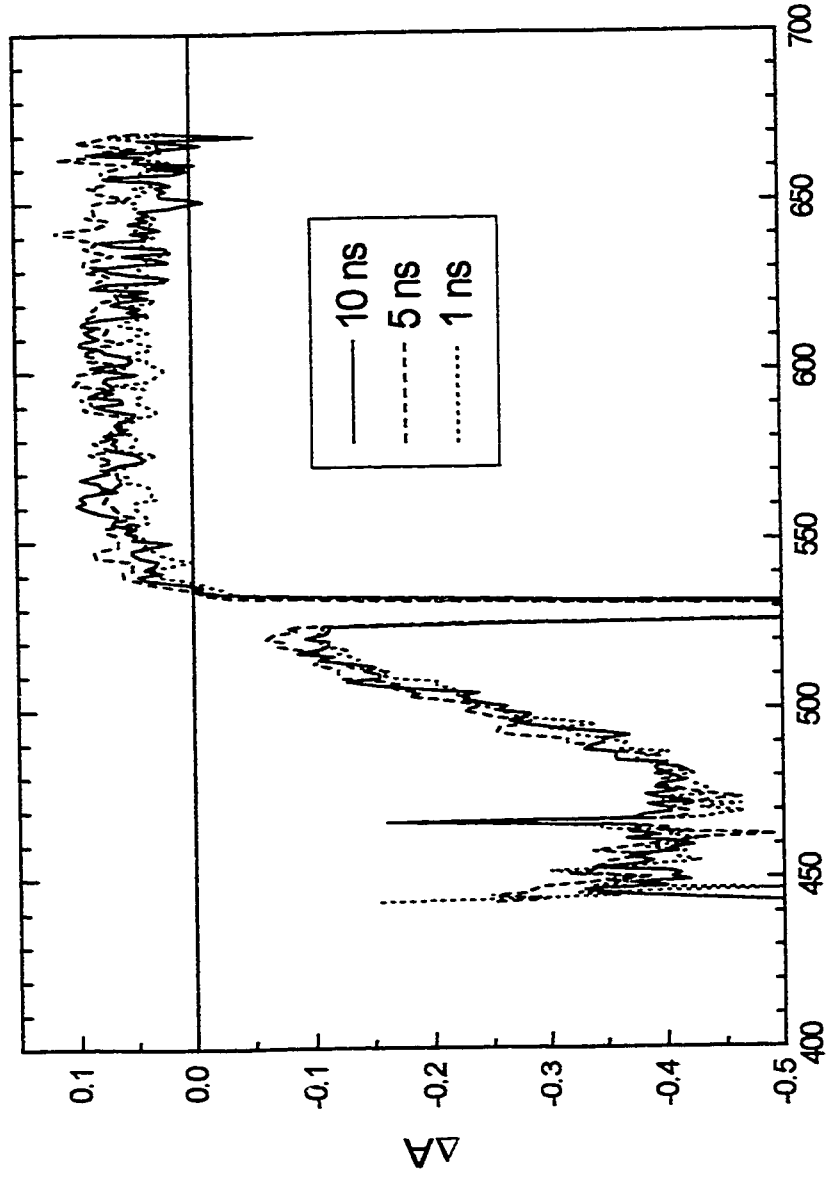

Figure C.21 Picosecond absorption spectra of $Cr(CNPh)_6$ in toluene (0.5 M py). 532 nm pump. Time delays 1, 5, and 10 ns.

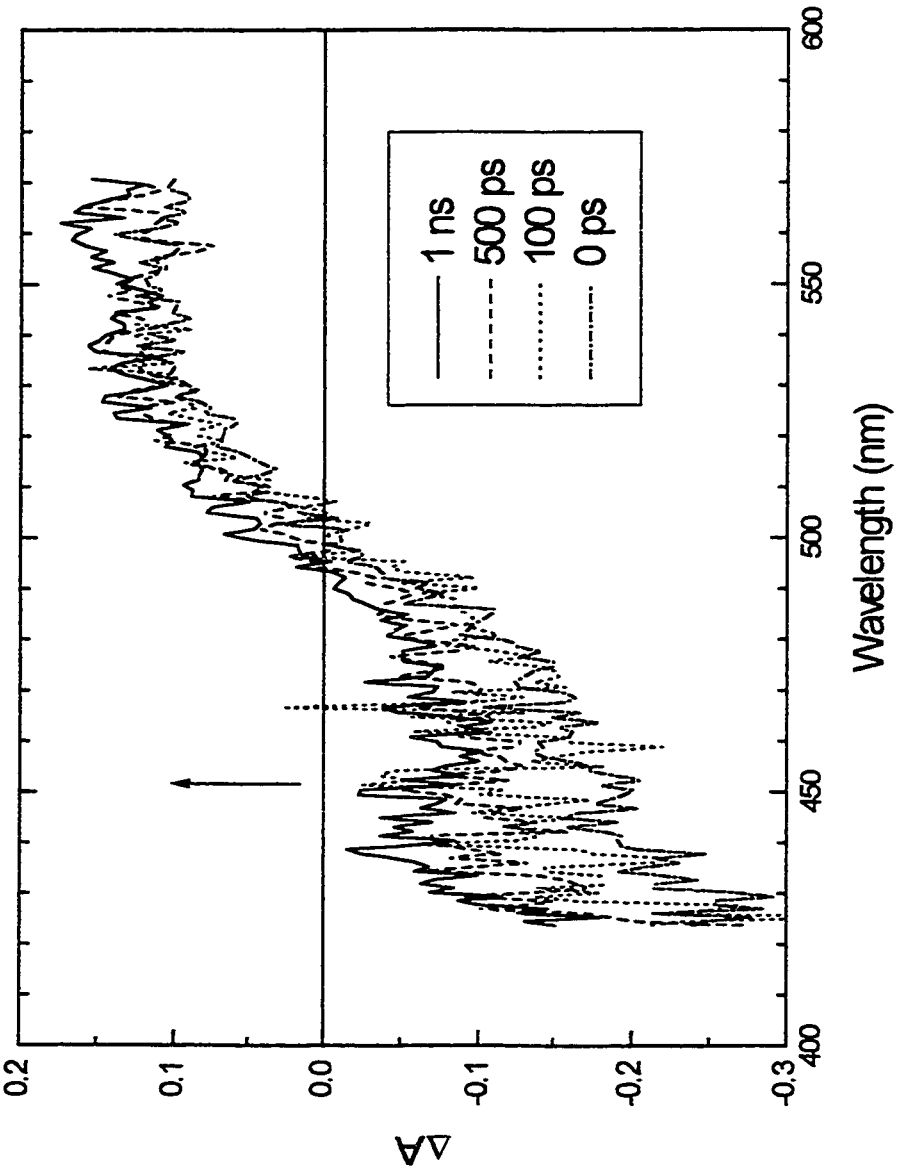

Figure C.22 Picosecond absorption spectra of $Cr(CNPh)_6$ in neat pyridine, 355 nm pump. Time delays 0 ps, 100 ps, 500 ps, and 1 ns.